

Theory and Practice in Replica-Exchange Molecular  
Dynamics Simulation

by

Benjamin Perry Cooke Isard

Department of Mathematics  
Duke University

Date: \_\_\_\_\_  
Approved:

\_\_\_\_\_  
Scott Schmidler, Supervisor

\_\_\_\_\_  
William Allard

\_\_\_\_\_  
Jonathan Mattingly

\_\_\_\_\_  
Terry Oas

Dissertation submitted in partial fulfillment of the  
requirements for the degree of Doctor of Philosophy  
in the Department of Mathematics  
in the Graduate School of  
Duke University

2008

## ABSTRACT

(Mathematics)

### Theory and Practice in Replica-Exchange Molecular Dynamics Simulation

by

Benjamin Perry Cooke Isard

Department of Mathematics  
Duke University

Date:

Approved:

---

Scott Schmidler, Supervisor

---

William Allard

---

Jonathan Mattingly

---

Terry Oas

An abstract of a dissertation submitted in partial fulfillment of the  
requirements for the degree of Doctor of Philosophy  
in the Department of Mathematics  
in the Graduate School of  
Duke University

2008

Copyright © 2008 by Benjamin Perry Cooke Isard  
All rights reserved

# Abstract

We study the comparison of computational simulations of biomolecules to experimental data. We study the convergence of these simulations to equilibrium and determine measures of variance of the data using statistical methods. We run replica-exchange molecular dynamics (REMD) simulations of eight helical peptides and compare the simulation helicity to the experimentally measured helicity of the peptides. We use one-way sensitivity analysis to determine which parameter changes have a large effect on helicity measurements and use Bayesian updating for a parameter of the AMBER potential. We then consider the theoretical convergence behavior of the REMD algorithm itself by evaluating the properties of the isothermal numerical integrators used in the underlying MD. The underlying constant-temperature integrators explored in this thesis represent a majority of the deterministic isothermal methods used with REMD simulations and we show that these methods either fail to be measure-invariant or are not ergodic. For each of the non-ergodic integrators we show that REMD fails to be ergodic when run with the integrator. We give computational results from examples to demonstrate the practical implications of non-ergodicity and describe hybrid Monte Carlo, a method that leads to ergodicity. Finally, we consider the use of stochastic Langevin dynamics to simulate isothermal MD. We show geometric ergodicity of the Langevin diffusion over a simplified system with the eventual goal of determining geometric ergodicity for Langevin dynamics over the full AMBER potential.

# Contents

<b>Abstract</b>	<b>iv</b>
<b>List of Tables</b>	<b>viii</b>
<b>List of Figures</b>	<b>ix</b>
<b>Acknowledgements</b>	<b>xiii</b>
<b>1 Introduction</b>	<b>1</b>
1.1 Peptides . . . . .	3
1.2 Purpose . . . . .	4
<b>2 Background</b>	<b>9</b>
2.1 Molecular Dynamics . . . . .	9
2.1.1 Hamiltonian Systems . . . . .	10
2.1.2 Numerical Integration . . . . .	11
2.1.3 Forcefields . . . . .	13
2.2 Boltzmann Distribution . . . . .	15
2.3 Replica-Exchange Molecular Dynamics . . . . .	16
2.4 Ergodicity . . . . .	17
<b>3 Comparing Replica-Exchange Simulations of Helical Peptides with Experimental Data</b>	<b>19</b>
3.1 Replica Exchange Molecular Dynamics . . . . .	19
3.2 Statistical Analysis and Evaluation . . . . .	23
3.2.1 Interval predictions . . . . .	26
3.2.2 Integrated Autocorrelation Estimate . . . . .	27

3.2.3	Batch Estimate . . . . .	28
3.2.4	Monitoring convergence . . . . .	29
3.3	Results . . . . .	32
<b>4</b>	<b>Determination of Simulation Parameters</b>	<b>39</b>
4.1	Parameter Adaptation . . . . .	40
4.1.1	Sensitivity Analysis . . . . .	41
4.1.2	Effect of $\epsilon_{in}$ and $S_{nb}$ Parameters . . . . .	42
4.1.3	Bayesian estimation of simulation parameters . . . . .	45
4.1.4	Cross Validation . . . . .	55
4.2	Conclusions . . . . .	57
<b>5</b>	<b>Preserving the Boltzmann Ensemble in Replica-Exchange Molecular Dynamics</b>	<b>58</b>
5.1	Ergodicity and Invariance in Molecular Simulation . . . . .	59
5.2	Hamiltonian Dynamics and Symplectic Integrators . . . . .	62
5.2.1	Symplectic integrators . . . . .	63
5.3	Isothermal Molecular Dynamics . . . . .	64
5.3.1	Velocity rescaling and the Berendsen heat-bath . . . . .	65
5.3.2	Extended Lagrangian methods . . . . .	66
5.3.3	Nosé-Hoover Integrators . . . . .	69
5.3.4	Nosé Poincaré Integrators . . . . .	72
5.3.5	Failure of ergodicity in REMD using isothermal dynamics . . .	74
5.3.6	Nosé-Poincaré Chains . . . . .	80
5.4	Stochastic dynamics . . . . .	81
5.4.1	Metropolis correction and Hybrid Monte Carlo . . . . .	81

5.4.2	Langevin Dynamics . . . . .	84
5.5	Examples . . . . .	85
5.5.1	Harmonic oscillators and Gaussian mixtures . . . . .	86
5.5.2	Alanine dipeptide . . . . .	91
5.5.3	High dimensional systems and irregular energy landscapes . .	95
5.6	Discussion . . . . .	100
<b>6</b>	<b>Geometric Ergodicity</b>	<b>102</b>
6.1	Simplified System . . . . .	104
6.2	Control Function . . . . .	106
6.3	Drift Condition . . . . .	108
<b>7</b>	<b>Conclusion</b>	<b>111</b>
7.1	Future Work . . . . .	112
<b>Bibliography</b>		<b>112</b>
<b>Biography</b>		<b>120</b>

# List of Tables

3.1	Helical peptides studied by simulation in this chapter, along with original experimental characterization and conditions. Peptides are either unblocked or have an N-terminal acetyl group (Ace) and/or a C-terminal amide group (Nhe). ID provides the peptide identifier used in other figures in this chapter. . . . .	20
3.2	forcefield and simulation parameters used in the helical peptide replica-exchange simulations, and as default values for the parameter sensitivity analysis. Parameters values are those used previously for simulating a helical peptideNymeyer and Garcia [2003]. . . . .	22
3.3	Time length of equilibration and production phases for REMD simulations of each peptide; peptide identifiers are given in Table 3.1. Equilibration and production times were determined according to the statistical convergence criteria described in Section 3.2.4. Due to the use of replica-exchange, equilibration is significantly faster than physical timescales (see Figure 3.3). . . . .	36
4.1	One-way sensitivity analysis of helicity as a function of simulation parameters. Shown are mean helicity and variance obtained for two peptides DGAEAAKAAAGR and SAEDAMRTAGGA at a range of values for each parameter studied. . . . .	43
4.2	Mean-squared error (MSE) for each value of $\epsilon_{in}$ , along with estimated out-of-sample prediction accuracy given by MSE obtained from cross-validation. . . . .	56

# List of Figures

1.1	This figure shows an example amino acid, Alanine. Alanine has backbone atoms found in every amino acid, N, C <sub><math>\alpha</math></sub> , C, and O, and a sidechain C <sub><math>\beta</math></sub> with three hydrogen atoms. . . . .	3
1.2	This figure shows the backbone angles $\phi$ and $\psi$ in a chain of two consecutive amino acids. The view on the left shows how the $\psi$ angle from the first amino acid can be measured by an end-on viewing of the bond. . . . .	4
1.3	This figure gives a context map of the chapters of this thesis. . . . .	7
2.1	This figure is a visual representation of the five terms contributing to the energy function in Equation 2.12: bond length (A), bond angle (B), dihedral angle (C), van der Waals (D), and electrostatics (E). . .	14
3.1	Quantile plots of standardized residuals $(\hat{h}_{ij} - \hat{h}_i)/\sigma_{\hat{h}_{ij}}$ for the $8 \times 4 = 32$ individual REMD simulations. The lack of significant deviation from the diagonal suggests the assumptions of normally distributed noise is reasonable. . . . .	29
3.2	Three configuration snapshots from the four parallel REMD simulations of peptide SAEDAMRTAGGA. Shown are (a) the four starting configurations, (b) four configurations observed at time of convergence to equilibrium, and (c) four configurations from the experiment phase of the simulation. . . . .	33
3.3	Convergence of REMD simulations of the eight peptides from Table 3.1, as measured by the Gelman-Rubin shrink factor for helical content. Plots represent convergence between 4 parallel simulations started from diverse initial configurations using parameters given in Table 3.2. Shown for comparison is a convergence plot for 4 standard MD simulations of peptide AE simulated without replica-exchange. .	34

3.4 Peptide helicity as estimated from simulation using the method of Shalongo and Stellwagen [1997] versus experimentally measured helicity for the eight peptides in Table 3.1. The diagonal line $y = x$ is shown as a reference. Simulation results are shown as 95% confidence intervals using standard errors estimates described in text, and are shown both for individual REMD runs and for the pooled estimates. . . . .	36
3.5 Peptide helicity as estimated from simulation versus experimentally measured helicity for the eight peptides in Table 3.1. The diagonal line $y = x$ is shown as a reference. Simulation results are shown as 95% confidence intervals using standard errors estimates described in text, and are shown both for individual REMD runs and for the pooled estimates. . . . .	37
4.1 The N-N (blue) and H-C (red) 1-4 interactions along the peptide backbone, which are most affected by changes in the $S_{nb}$ scaling constant in the AMBER potential. The effect of equilibrium distances for these atom pairs has a significant effect on the $(\phi,\psi)$ angles of their respective amino acids, and hence on peptide helicity. . . . .	44
4.2 Effects of the non-bonded scaling parameter $S_{nb}$ on the equilibrium distances of successive backbone nitrogen atoms (N-N), hydrogen-carbon atom pairs (H-C), and $\alpha$ -carbons ( $C_\alpha$ - $C_\alpha$ ). Line represents the ensemble-mean helicity for the $i^{th}$ amino acid as a function of the $N_i$ - $N_{i+1}$ distance (plots a,b), $H_i$ - $C_i$ distance (c,d), or $C_\alpha$ - $C_\alpha$ distance (e,f) for the two peptides DGAEAAKAAAGR (a,c,e) and SAEDAMRTAGGA (b,d,f). Individually labeled points give the average N-N or H-C distance for simulations with $S_{nb} = \{0.5, 1, 1.2, 1.5, 2, 3, 5\}$ . Helicity changes in response to varying $S_{nb}$ can be explained by sensitivity to N-N and H-C distances; other 1-4 atom pairs have little effect on helicity as demonstrated here for $C_\alpha$ - $C_\alpha$ . . . . .	46
4.3 Quantile plots of standardized residuals $(\hat{h}_i - h_i^{exp})/\sigma_{\hat{h}_i}$ for the eight combined simulation peptide helicities versus experiment. The lack of significant deviation from the diagonal suggests the assumptions of normally distributed noise is reasonable. . . . .	48

4.4	Posterior distributions for the dielectric constant $\epsilon_{in}$ evaluated at discrete values, obtained using Bayesian parameter updating described in Section 4.1.3 under uniform prior. (a) Posterior over $\epsilon_{in} \in \{1, 2, 3, 4, 5\}$ . (b) An additional simulation was run at $\epsilon_{in} = 4.1$ to help identify the mode of the posterior distribution. . . . .	50
4.5	Simulated helicity versus experimental helicity for the peptides in Table 3.1 evaluated at a range of values of the internal dielectric parameter $\epsilon_{in}$ . . . . .	51
4.6	Helicity versus $\epsilon_{in}$ for each peptide in Table 3.1 at values of $\epsilon_{in} \in \{1, 2, 3, 4, 4.1, 5\}$ . The experimentally measured helicity for each peptide is plotted as a horizontal line. . . . .	52
4.7	Marginal posterior distributions of boundaries of the helical angle region (a) $\phi_{\min}$ and $\phi_{\max}$ , and (b) $\psi_{\min}$ and $\psi_{\max}$ . . . . .	54
5.1	Comparison of four dynamics simulation algorithms for the target distributions $\pi_1$ (left column) and $\pi_2$ (right column) defined in text. Algorithms are (top to bottom): microcanonical dynamics using leap-frog integrator; canonical dynamics using Berendsen heat bath; canonical dynamics using Nosé-Poincaré integrator; and canonical Langevin dynamics. . . . .	90
5.2	Replica-exchange dynamics using each of the four dynamics algorithms, for simulating $\pi_1$ (left) and $\pi_2$ (right). Each REMD involves 10 replicas of the corresponding dynamics. . . . .	92
5.3	The four dynamics algorithms of Figure 5.1, augmented with the hybrid Monte Carlo correction described in text. . . . .	93
5.4	Replica-exchange simulations using the four respective dynamics algorithms, each with the hybrid Monte Carlo correction. The microcanonical and Langevin algorithms thus become parallel tempering HMC and parallel tempering Langevin dynamics respectively, both of which are measure-invariant and ergodic. . . . .	94
5.5	Molecular structure of alanine dipeptide. . . . .	95



# Acknowledgements

I would like to thank my advisor, Professor Scott Schmidler, for his encouragement throughout my Duke graduate career. His patience and steadfast support were instrumental in guiding me through the work done in this thesis. Thanks to Professor Jonathan Mattingly and Dr. Scott McKinley for their continued help. Thanks to Professors William Allard for his encouragement to work on an interdisciplinary project and to Professor Terry Oas for serving on my committee.

I would like to thank James Michael, Dr. Ryan Anderson, Lauren Shareshian, Dr. David Anderson, Dr. Tim Lucas, and Dr. Derek Rasheed for their friendship during my graduate career at Duke.

I thank the departmental staff of both the Mathematics Department and the Institute for Statistics and Decision Sciences, including Andrew Schretter, Lance Brown, Carolyn Sessoms, Sunny Oakley, Georgia Barnes, Anna Duke, and Shannon Holder. The time they have dedicated to computer support and administrative support have allowed my research to be conducted and helped smoothly transition me through the phases of graduate school.

I would like to thank my parents and my sister for their encouragement, love, and advice. Thank you for believing in me and giving me the foundation to set forth on this journey.

Finally, I would like to thank my wife Linda for standing next to me and giving me the love and support I have needed. Your faith in me has allowed me to believe in myself.

# Chapter 1

## Introduction

Molecular modeling is becoming more popular as the field of biomolecular science transitions from discovering new genes to discovering the genes' functions. Proteins are the engineers of our cells, and understanding their functions requires a clear knowledge of their shapes and folds. Modeling protein folding and, ultimately, simulating protein interaction is motivated by the fact that other tools such as crystallography are costly in both time and money and limited in their ability to track protein behavior [Duan and Kollman, 1998]. The ability to computationally simulate the behavior of proteins folding or interacting would greatly speed the study of protein behavior.

Scientists have been interested in the behavior of molecules since before Boltzmann founded the branch of physics known as statistical mechanics. Computer modeling, which got its start when molecular dynamics (MD) was developed in the 1950s [Alder and Wainwright, 1957] within the field of theoretical physics, has become an important and widely used tool in the study of biomolecular systems [Schlick, 2002, Leach, 1996, Frenkel and Smit, 1996]. With the growing availability of high-

speed desktop computers and cluster computing, simulations that once required access to specialized supercomputers are now feasible for many individual laboratories. However, simulations of biomolecules still have some ways to go relative to simulations in other fields. In fields such as physics and chemistry, as well as in macroscopic areas of engineering and astronomy, simulations are regularly used *in lieu of* physical experiment, due to their ability to accurately and consistently predict physical quantities. By contrast, macromolecular simulations are currently used primarily for exploratory and visualization purposes, rather than quantitative prediction. However, as computational resources grow and algorithms improve, we can strive to develop truly accurate macromolecular computer experiments.

Because of the availability of computer processors and the quick turnaround speed of converting new algorithms into computer code, many new methods are being used to simulate molecular interaction. One of the newer methods is replica-exchange molecular dynamics (REMD), which has come to the forefront within the last ten years [Sugita and Okamoto, 1999]. REMD uses multiple parallel simulations of the same molecule or system of molecules each at a different temperature on some chosen scale of temperatures. Each parallel simulations is run at its chosen temperature, and at intervals, the temperatures of two of the parallel simulations may be swapped with positive probability. The ability to run REMD on parallel processors has made it a popular tool for molecular modelers; however, accurate measures of simulation data for large proteins remain beyond current computational resources.

We next introduce peptides, which in Chapters 3 and 4 is used in REMD simulations to study helical peptide folding. Helical peptide folding has been a widely

studied model system for protein folding both experimentally [Scholtz and Baldwin, 1992] and computationally [Daggett et al., 1991, Brooks and Case, 1993, Garcia and Sanbonmatsu, 2002, Daura et al., 1998, Hansmann and Okamoto, 1999, Gnanakaran et al., 2003, Jas and Kuczera, 2004, Sorin and Pande, 2005b].

## 1.1 Peptides

*Peptides* are constructed of strings of amino acids, each of which has a basic structure of backbone atoms and a side-chain. The backbone atoms of each amino acid combine to form the backbone of the peptide. An example amino acid is shown in Figure 1.1.

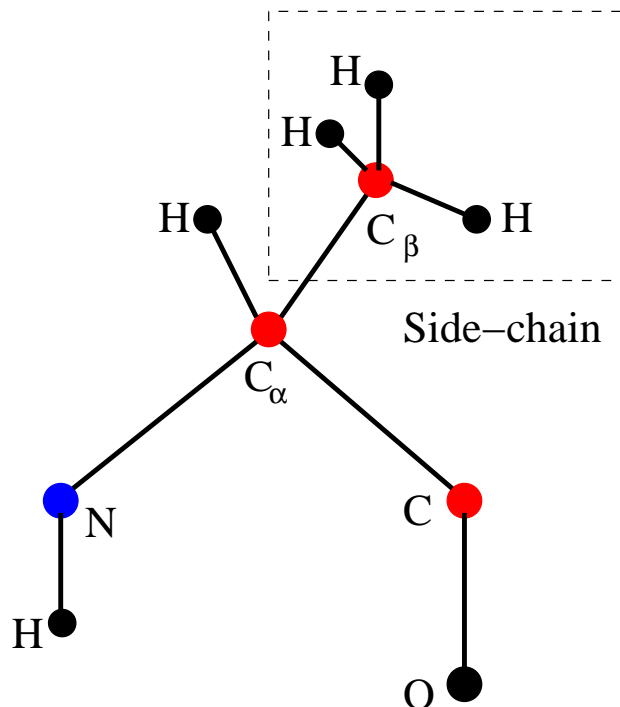


**Figure 1.1:** This figure shows an example amino acid, Alanine. Alanine has backbone atoms found in every amino acid, N,  $C_\alpha$ , C, and O, and a sidechain  $C_\beta$  with three hydrogen atoms.

Peptides are formed from short strings of six to thirty of the twenty types of amino acids [Branden and Tooze, 1999]. *Helical peptides* are peptides that form helical con-

figurations in equilibrium. The helicity of a peptide configuration can be measured by the dihedral angles of its amino acids,  $\phi$  and  $\psi$ . These backbone angles measure the twist around a single bond and can be measured between four atoms bonded consecutively. The range of angle measures is chosen to be  $(-180^\circ, 180^\circ)$  and can be used to measure the helicity of a peptide. Figure 1.2 helps visualize the  $\psi$  dihedral angle. A more in depth discussion of how to use these  $\phi$  and  $\psi$  angles to compute the helicity of a peptide configuration is given in Chapter 3.

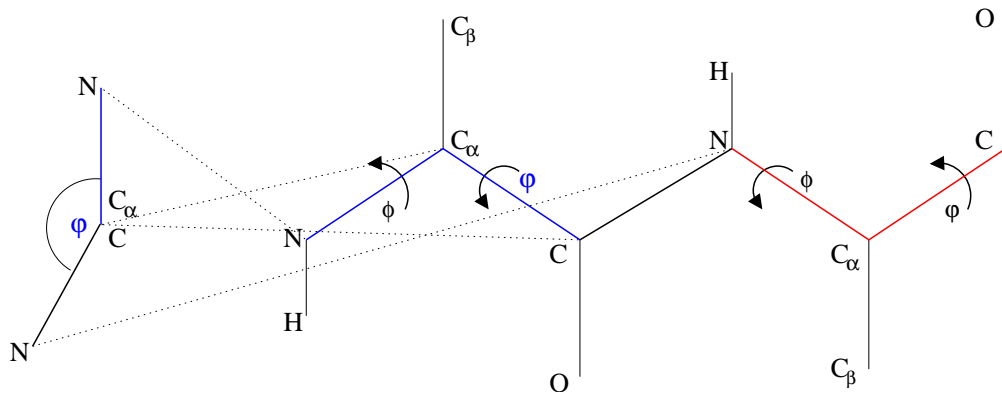


**Figure 1.2:** This figure shows the backbone angles  $\phi$  and  $\psi$  in a chain of two consecutive amino acids. The view on the left shows how the  $\psi$  angle from the first amino acid can be measured by an end-on viewing of the bond.

## 1.2 Purpose

The main purpose of this thesis is to examine how computer simulations of molecules can be used to *accurately* replicate molecular behavior. Computer simulation of molecules can only approximate the true behavior of molecules *en vivo*, but in this thesis we present methods to account for and improve approximations made using a particular type of molecular modeling, molecular dynamics (MD).

The path of work reported on in this thesis started with an interest in determining

more accurate ways to fold proteins. This led to studying peptide folding as a more computationally realistic pursuit, and comparing the results of experimental helicity data of known peptides to computer simulations. After using methods shown in the literature to be successful folding peptides [Garcia and Sanbonmatsu, 2002, Nymeyer and Garcia, 2003], we were unsatisfied with the level of variation of our results due to small parameter changes, especially because differing parameter values were widely used. This motivation led to the work in Chapters 3 and 4.

After continued dissatisfaction with the variety of temperature scaling methods and a desire to evaluate novel methods, we became more interested in the properties of the numerical integrators used with the simulations. We programmed some of the numerical integrators on small test examples and reached a more thorough mathematical understanding of the properties of the differing integrators, as described in Chapter 5.

To understand what is in the heart of each of these chapters, one must understand two fundamental ideas: the Boltzmann distribution, and ergodicity. Given a particular peptide or set of peptides in a solution, the Boltzmann distribution defines the probability of any particular configuration of the peptide(s). In experiments, the peptides spend most of their time in configurations with high probability, but theoretically any configuration or set of configurations with positive probability can be reached. The definition of the Boltzmann distribution is given in Chapter 2, but the key idea is that in the experimental world, the positions or configurations that proteins take on are sampled from this Boltzmann distribution.

To represent an accurate picture of the set of protein positions and configurations

that should occur, a computer simulation must sample configurations according to this Boltzmann distribution, which brings us to ergodicity. For a simulation to sample from the correct Boltzmann distribution, it must be able to reach all possible configurations. If one is trying to simulate molecules but some configurations cannot be reached, then inaccurate behavior may be observed.

Chapter 2 defines the necessary background material needed for the remainder of the thesis. We start by defining Hamiltonian systems, which are used in modeling molecular systems. We define the potential energy functions used by MD to replicate the forces felt by the atoms in each molecule. Then we cover the basic numerical integrators used in MD simulations including the leap-frog method. We define replica-exchange molecular dynamics (REMD) and finish with mathematical definitions of measure invariance and ergodicity.

Figure 1.3 gives a context map of the body of this thesis. Chapter 3 compares REMD simulations of eight helical peptides with experimental data by using statistical tests to measure convergence and accuracy of the simulations. We run multiple REMD simulations for each peptide starting from different initial configurations and determine convergence by observing when the distinct simulations have generated similar distributions of configurations. We also use statistical methods to determine the accuracy of simulation quantities of interest, in particular the experimental observables such as peptide helicity.

In Chapter 4 we examine the effects of perturbing forcefield parameters on the helical peptide simulation results obtained in the previous chapter. Applying simple statistical ideas, we are able to calculate the likelihood of the “true” value of each

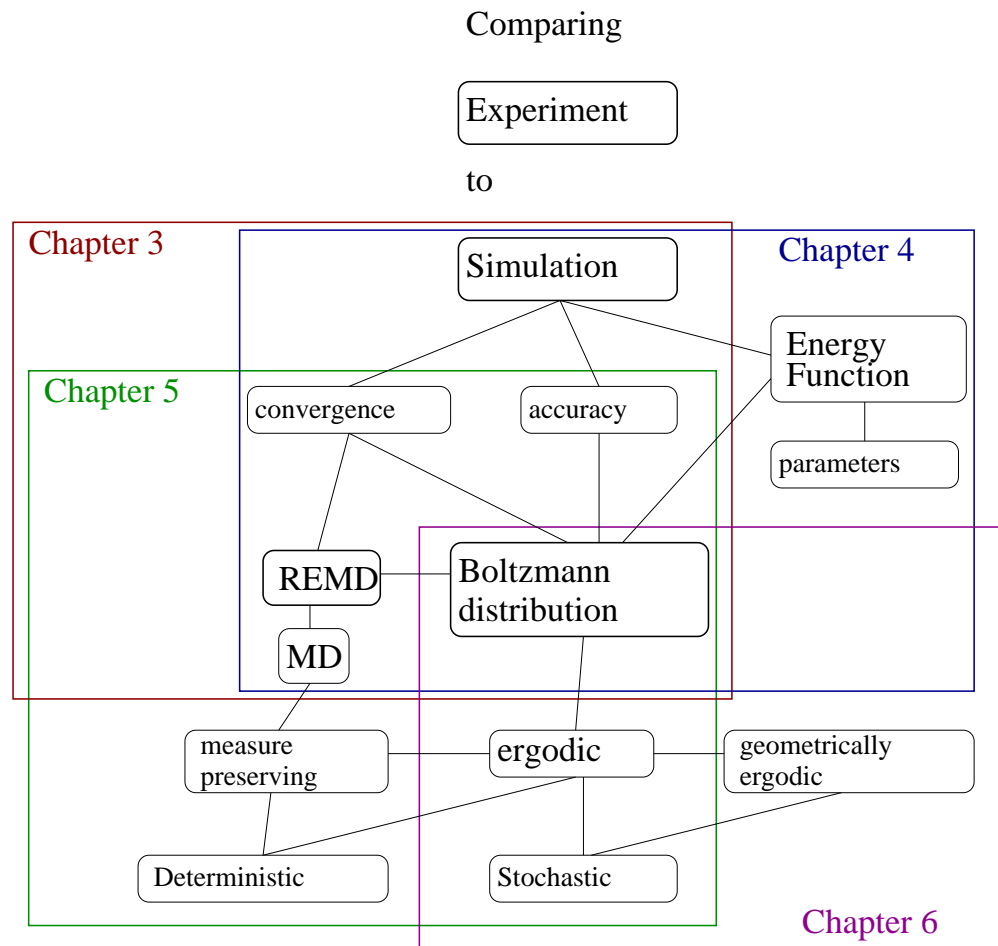


**Figure 1.3:** This figure gives a context map of the chapters of this thesis.

parameter by comparing the simulated helicity with the experimentally measured helicity. Chapters 3 and 4 were published together as an article in the Biophysics Journal [Cooke and Schmidler, 2008a].

Chapter 5 contains a detailed theoretical examination of the replica-exchange simulation methodology being used in the literature. We examine the ergodicity of REMD, using both deterministic and stochastic numerical integrators for the molecular dynamics portion of REMD. We demonstrate the shortcomings of non-ergodic methods by applying some of the integrators in question to test problems. Chapter 5 was published as an article in the Journal of Chemical Physics [Cooke and Schmidler, 2008a].

In Chapter 6, we consider the rate of convergence of Langevin diffusion, a simplified version of stochastic integrator often used with REMD. We establish the *geometric* ergodicity of Langevin diffusion under a simplified model and discuss the difficulties which arise for the actual AMBER energy function used in practice. Finally in Chapter 7 we conclude with a discussion of the implications of the thesis and directions for future work.

# Chapter 2

## Background

The study of molecules using computation is built upon a foundation of mathematics, without which the numerical results produced by simulations are meaningless. To grasp the results presented in this thesis, an understanding of the fundamental tools and systems underlying MD and REMD is needed.

### 2.1 Molecular Dynamics

Molecular dynamics simulation of a molecular system acting under potential energy  $U(\mathbf{q})$  involves numerical solution of the differential system arising from Newtonian dynamics:

$$\begin{aligned}\dot{\mathbf{q}}_i &= \frac{\mathbf{p}_i}{m_i} \\ \dot{\mathbf{p}}_i &= -\frac{\partial U(\mathbf{q}_i)}{\partial \mathbf{q}_i}.\end{aligned}\tag{2.1}$$

This system of ordinary differential equations yields trajectories in the phase space  $\mathcal{X} = \{\mathbf{x} : \mathbf{x} = (\mathbf{q}, \mathbf{p}) \in \mathbb{R}^{2d}\}$  of positions  $\mathbf{q}$  and associated momenta  $\mathbf{p}$ , and is a Hamiltonian system.

### 2.1.1 Hamiltonian Systems

A *Hamiltonian system* is a system of the form

$$\frac{d\mathbf{q}_i}{dt} = \frac{\partial \mathcal{H}}{\partial \mathbf{p}_i} \quad (2.2)$$

$$\frac{d\mathbf{p}_i}{dt} = -\frac{\partial \mathcal{H}}{\partial \mathbf{q}_i} \quad (2.3)$$

where  $\mathbf{q}$  and  $\mathbf{p}$  are position and velocity, respectively. Newton's equations of motion form a Hamiltonian system, with Hamiltonian defined by the sum of the potential energy and the kinetic energy,

$$\mathcal{H}(\mathbf{q}, \mathbf{p}) = U(\mathbf{q}) + K(\mathbf{p}) = U(\mathbf{q}) + \sum_i \frac{\mathbf{p}_i^2}{2m_i}. \quad (2.4)$$

To see that Newton's equations of motion form a Hamiltonian system, we first note that

$$\mathbf{p}_i = m_i \mathbf{v}_i \quad \text{and} \quad \frac{d\mathbf{p}_i}{dt} = m_i \frac{d\mathbf{v}_i}{dt}.$$

Then by taking the derivative of  $\mathcal{H}$  with respect to  $\mathbf{q}_i$ , and noticing that the  $i$ th derivative of  $U$  is the  $i$ th coordinate of the force vector, or  $-\frac{\partial U}{\partial \mathbf{q}_i} = \mathbf{F}_i(\mathbf{q})$ , we see that

$$-\frac{\partial \mathcal{H}}{\partial \mathbf{q}_i} = -\frac{\partial U}{\partial \mathbf{q}_i} = \mathbf{F}_i(\mathbf{q}) = m_i \mathbf{a}_i = m_i \frac{d\mathbf{v}_i}{dt} = \frac{d\mathbf{p}_i}{dt}. \quad (2.5)$$

Similarly, by taking the  $\mathbf{p}_i$  derivative of  $\mathcal{H}$ , we see that

$$\frac{\partial \mathcal{H}}{\partial \mathbf{p}_i} = \frac{\partial K}{\partial \mathbf{p}} = \frac{\mathbf{p}_i}{m} = \frac{m_i \mathbf{v}_i}{m_i} = \mathbf{v}_i = \frac{d\mathbf{q}_i}{dt}. \quad (2.6)$$

Our Hamiltonian system for Newton's equations of motion can then be written as a system of ordinary differential equations:

$$\begin{aligned}\dot{\mathbf{q}}_i &= \frac{\partial \mathcal{H}}{\partial \mathbf{p}_i} = \frac{\mathbf{p}_i}{m_i}, \\ \dot{\mathbf{p}}_i &= -\frac{\partial \mathcal{H}}{\partial \mathbf{q}_i} = \mathbf{F}_i(\mathbf{q}).\end{aligned}\tag{2.7}$$

To run MD simulations, numerical integrators are used to generate solutions of the system defined in Equation 2.1.

### 2.1.2 Numerical Integration

For a system of ordinary differential equations, a *numerical integrator* generates an approximate solution trajectory of the system given a time-step and initial positions and velocities. Numerical integration techniques that are used with MD include the Verlet algorithm [Verlet, 1967], the leap-frog method [Hockney, 1970], and the velocity-Verlet algorithm [Swope et al., 1982]. The *Verlet method* is given by the two updating steps:

$$\begin{aligned}\mathbf{q}_i(t + \Delta t) &= 2\mathbf{q}_i(t) - \mathbf{q}_i(t - \Delta t) + \frac{1}{m_i} \frac{\partial U}{\partial \mathbf{q}_i}(t) \Delta t^2 \\ \mathbf{p}_i(t) &= m_i \frac{(\mathbf{q}_i(t + \Delta t) - \mathbf{q}_i(t - \Delta t))}{2\Delta t}.\end{aligned}\tag{2.8}$$

To produce the *leap-frog method*, so called because the momenta are calculated on half time-steps, we first write down two second-order differences.

$$\begin{aligned}\mathbf{p}_i(t - \Delta t/2) &= m_i \frac{(\mathbf{q}_i(t) - \mathbf{q}_i(t - \Delta t))}{\Delta t} \\ \mathbf{p}_i(t + \Delta t/2) &= m_i \frac{(\mathbf{q}_i(t + \Delta t) - \mathbf{q}_i(t))}{\Delta t}.\end{aligned}$$

Taking the second expression for the position and subtracting  $\mathbf{p}_i(t - \Delta t/2)$  from  $\mathbf{p}_i(t + \Delta t/2)$ , and substituting in for  $\mathbf{q}_i(t + \Delta t)$  from the Verlet algorithm gives:

$$\begin{aligned}\mathbf{q}_i(t + \Delta t) &= \mathbf{q}_i(t) + \frac{\mathbf{p}_i(t + \Delta t/2)}{m_i} \Delta t \\ \mathbf{p}_i(t + \Delta t/2) &= \mathbf{p}_i(t - \Delta t/2) + \frac{\partial U}{\partial \mathbf{q}_i}(t) \Delta t.\end{aligned}\quad (2.9)$$

The *velocity-Verlet method* can be written as:

$$\begin{aligned}\mathbf{q}_i(t + \Delta t) &= \mathbf{q}_i(t) + \frac{\mathbf{p}_i(t)}{m_i} \Delta t + \frac{1}{2m} \frac{\partial U}{\partial \mathbf{q}_i}(t) \Delta t^2 \\ \mathbf{p}_i(t + \Delta t) &= \mathbf{p}_i(t) + \frac{\Delta t}{2} \left( \frac{\partial U}{\partial \mathbf{q}_i}(t) + \frac{\partial U}{\partial \mathbf{q}_i}(t + \Delta t) \right).\end{aligned}\quad (2.10)$$

All three methods produce *deterministic* dynamical systems: there is no stochastic element. By definition, these algorithms conserve the total energy because they are solving a Hamiltonian system. The total energy is defined as the sum of the potential energy and the kinetic energy:

$$E(\mathbf{q}, \mathbf{p}) = U(\mathbf{q}) + K(\mathbf{p}).\quad (2.11)$$

Therefore, when used for MD simulation, each method produces trajectories in a *microcanonical ensemble*, or set of all molecular configurations with constant energy. However due to the numerical error produced both by choosing a positive step-size and by computing with finite precision hardware, the configurations in the trajectories do not all have *exactly* the same energy; but these methods are chosen because they keep the energy from drifting over time. We discuss the energy conservation of these and other methods in Chapter 5.

### 2.1.3 Forcefields

Many different formulae have been proposed for measuring the potential energy  $U(\mathbf{q})$ .

One commonly used measure is the AMBER energy potential [Pearlman et al., 1995], given by the covalently-bonded and non-bonded terms:

$$U(\mathbf{q}) = \sum_{\text{bonds}} K_i(r_i - r_{0,i})^2 + \sum_{\text{angles}} L_i(\theta_i - \theta_{0,i})^2 + \sum_{\text{dihedrals}} \frac{V_i}{2}[1 + \cos(n_i\phi_i - \gamma_{0,i})] \\ + \sum_{\text{non-bonded}} \left[ \frac{A_{ij}}{r_{ij}^{12}} - \frac{B_{ij}}{r_{ij}^6} + \frac{q_i q_j}{\epsilon r_{ij}} \right]. \quad (2.12)$$

This potential function is a sum of five sources of potential energy: bond length stretching (vibration), bond angle opening, dihedral angle rotation, van der Waals interactions, and electrostatic interactions. These terms are shown visually in Figure 2.1. The first term (A) is the squared difference between each bond length and an isolated equilibrium length of that bond. The second term (B) is the squared difference between each bond angle and its typical equilibrium value. The third term (C) accounts for the preference of particular dihedral angles by sets of four atoms bonded in a row. The van der Waals term (D) gives a beneficial energy to atoms that are barely touching but penalizes atoms with overlapping volumes. The final term (E) measures the contribution of electrostatic charge interactions. Two other forcefields commonly used for MD, CHARMM [Brooks et al., 1983] and GROMACS [Lindahl et al., 2001] have similar forms with different parameter values. The values of the parameters that enter these functions are approximated using empirical or theoretical studies and depend on the choice of energy function and the empirical or theoretical method [Leach, 1996]. Other parameters that are not a part of the energy function but of the simulation, such as the time-step of the integrator

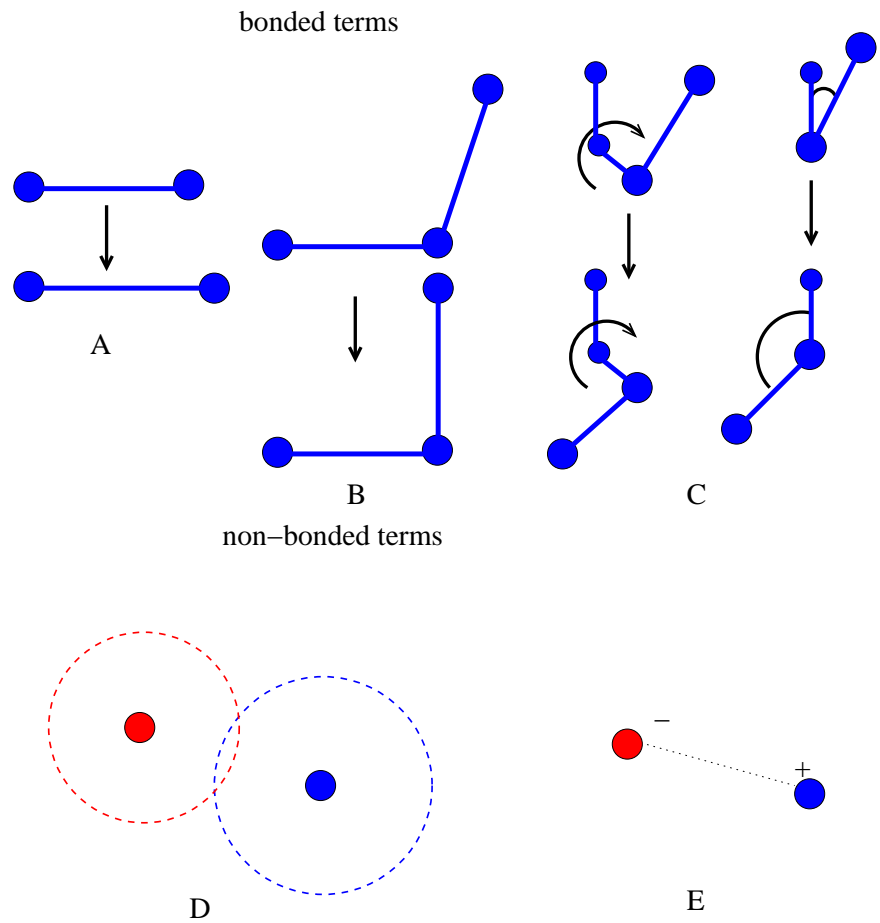


**Figure 2.1:** This figure is a visual representation of the five terms contributing to the energy function in Equation 2.12: bond length (A), bond angle (B), dihedral angle (C), van der Waals (D), and electrostatics (E).

or parameters introduced by the use of an explicit or implicit solvent, create error. Some of the parameters have a profound effect on the outcome of MD simulations as shown in Chapter 4. We use Bayesian methods to estimate some of these simulation parameters by comparison with experimental data in Chapter 4.

## 2.2 Boltzmann Distribution

The Boltzmann distribution of a configuration of positions and velocities  $\mathbf{x} = (\mathbf{q}, \mathbf{p})$  is defined by the energy function  $E(\mathbf{x}) = U(\mathbf{q}) + K(\mathbf{p})$ , where  $U$  is the potential energy and  $K$  is the kinetic energy. For a given temperature  $T$ , the Boltzmann distribution  $\pi_T(\mathbf{q}, \mathbf{p})$  is defined as:

$$\pi_T(\mathbf{x}) = \frac{e^{-E(\mathbf{x})/(k_B T)}}{\int_{(\mathbf{q}, \mathbf{p})} e^{-E(\mathbf{x})/(k_B T)}}, \quad (2.13)$$

where  $k_B$  is Boltzmann's constant. For molecular dynamics simulations, the potential energy function that defines this distribution is given above by Equation 2.12. This equation, including its parameters, is a theoretical approximation to the true potential energy, and thus the Boltzmann distribution it defines is only an approximation of the actual physical Boltzmann distribution defined by the real potential energy. Improving such approximate energy functions would improve the accuracy of molecular dynamics simulations; we give a method for improving the accuracy of the energy function parameters in Chapter 4. It is also critical that this theoretical Boltzmann distribution is correctly sampled by the simulation. If the distribution defined by the energy function is not accurately sampled, then the error of the underlying energy function is compounded by the error introduced by the simulation.

In Chapter 5 we determine which methods in common use are accurately sampling from the theoretical Boltzmann distributions.

## 2.3 Replica-Exchange Molecular Dynamics

The replica-exchange molecular dynamics (REMD) algorithm of Sugita and Okamoto [1999] has become a widely-used tool for molecular simulation [Seibert et al., 2005, Periole and Mark, 2007, Zhang et al., 2005, Nguyen et al., 2005, Beck et al., 2007, Roitberg et al., 2007]. *Replica-exchange* molecular dynamics arises by applying the parallel tempering method [Geyer, 1991] to molecular dynamics (MD) simulation. The REMD algorithm runs multiple isothermal MD simulations in parallel at a sequence of increasing temperatures  $(T_0, T_1, \dots, T_n)$  and intermittently attempts to swap simulations between temperatures: every  $L$  steps, two chains  $j$  and  $k$  are randomly chosen (or  $j$  random and  $k = j + 1$ ), and the proposed swap accepted with probability given by the Metropolis ratio below.

$$\min \left\{ 1, \frac{\pi_{T_k}(\mathbf{q}_j, \mathbf{p}_j)\pi_{T_j}(\mathbf{q}_k, \mathbf{p}_k)}{\pi_{T_j}(\mathbf{q}_j, \mathbf{p}_j)\pi_{T_k}(\mathbf{q}_k, \mathbf{p}_k)} \right\}, \quad (2.14)$$

The distribution  $\pi_{T_i}(\mathbf{q}_j, \mathbf{p}_j)$  is the Boltzmann distribution for replica  $j$  at temperature  $T_i$  given in Equation 2.13. The resulting REMD algorithm is a stochastic dynamical system on  $\mathcal{X} = \mathbb{R}^{2dn}$ . The added stochastic element enables the crossing of large energy barriers and has caused the REMD algorithm to see a surge in popularity for simulations of complex molecules such as peptides and proteins. Also fueling this surge is the ability to parallelize REMD and the evidence that parallel tempering simulations equilibrate dramatically faster. Recent theoretical results

for parallel tempering Monte Carlo show that a range of sampling problems which take exponential time to converge with traditional sampling techniques such as the Metropolis algorithm, converge dramatically faster (polynomial time) when parallel tempering is applied [Madras and Zheng, 2003, Woodard et al., 2008], although such speed-ups do not occur for every system [Bhatnagar and Randall, 2004, Woodard et al., 2007].

## 2.4 Ergodicity

Molecular simulation using both MD and REMD are sometimes compared to experimental data, [Garcia and Sanbonmatsu, 2002, Sorin and Pande, 2005a, Nymeyer and Garcia, 2003, Hansmann and Okamoto, 1999, Jas and Kuczera, 2004], and the results of simulation have also been used to infer underlying biological phenomena [Garcia and Sanbonmatsu, 2002]. To make a claim that simulation results are accurate or are a valid approximation to wet lab experiments, the behavior of these simulations must be understood. In particular, simulations must be run to an equilibrium distribution, and this distribution must be correct. In Chapter 3 we show how to use statistical tools to determine when simulations have reached this equilibrium. Here we define two concepts, measure invariance and ergodicity, which we use in Chapter 5 to show which REMD simulations reach the correct theoretical equilibrium.

Each numerical integrator can be defined as a transformation/mapping  $T$  on a measure space  $(X, \mu)$ .

**Definition 1.** *A transformation  $T$  is  $\mu$ -invariant if  $T^{-1}(E)$  is measurable for every measurable subset  $E \subset X$ , and  $\mu(T^{-1}E) = \mu(E)$  for every (measurable) subset*

$E \subset X$ , or equivalently, if for any  $f \in L^1(\mu)$ ,

$$\int_X f(x) d\mu = \int_X f(T(x)) d\mu.$$

**Definition 2.** For  $(X, \mathcal{A}, \mu)$  a probability space, and  $T$  a  $\mu$ -invariant transformation on  $X$ ,  $T$  is ergodic if  $E \in \mathcal{A}$  satisfies  $T^{-1}E = E$  if and only if  $\mu(E) = 0$  or 1 (equivalently,  $E = \emptyset$  or  $E = X$ ). Equivalently, for  $\mu(A) > 0$  then  $\bigcup_{n=1}^{\infty} T^{-n}A = X$ , and for  $\mu(A) > 0$  and  $\mu(B) > 0$ , then  $\mu(T^{-n}A \cap B) > 0$  for some  $n \geq 1$  (see Choe [2005]).

Intuition behind these definitions is that if a numerical integrator is  $\mu$ -invariant, as the simulation generates new points it is maintaining the distribution  $\mu$ . If a numerical integrator is ergodic then it can, and eventually does, reach any state in the system from any other state. We further explore these conditions for REMD in Chapter 5.

# Chapter 3

## Comparing Replica-Exchange Simulations of Helical Peptides with Experimental Data

This chapter compares the experimental helicity of eight naturally occurring and designed helical peptides with REMD simulations of the same eight peptides. The peptides have been studied experimentally with circular dichroism (CD) and shown to have measurable helicity (mean  $\theta_{222}$  ellipticity) in solution. Table 3.1 shows the peptides studied along with their original experimental characterization; these peptides were selected from a database of helical peptides model prediction [Schmidler et al., 2007] to obtain a range of helicities among native peptides at physiological pH.

### 3.1 Replica Exchange Molecular Dynamics

For the REMD simulations in this chapter, each replica was run under the AMBER94 forcefield using the AMBER 7 suite of programs. [Pearlman et al., 1995] The specific AMBER94 potential [Pearlman et al., 1995] consists of covalently-bonded and non-

ID	N-	Peptide Sequence	C-	Exp Hel	Tmp (°K)	pH	Reference
DG	-	DGAEEAKAAAGR	Nhe	0.196	273	7	Forood et al. [1993]
SA	Ace	SAEDAMRTAGGA	-	0.168	273	7	Goodman and Kim [1989]
RD	-	RDGWKRLIDIL	-	0.050	277	7	Munoz and Serrano [1997]
ES	-	ESLLERITRKL	-	0.217	277	7	Munoz and Serrano [1997]
LK	Ace	LKEDIDAFLAGGA	Nhe	0.150	298	7	Spector et al. [1999]
PS	Ace	PSVRKYAREKGV	Nhe	0.097	298	7	Spector et al. [1999]
RE	Ace	REKGVDIRLVQG	Nhe	0.134	298	7	Spector et al. [1999]
AE	Ace	AETAGAKFLRAHA	Nhe	0.126	276	7	Strehlow and Baldwin [1989]

**Table 3.1:** Helical peptides studied by simulation in this chapter, along with original experimental characterization and conditions. Peptides are either unblocked or have an N-terminal acetyl group (Ace) and/or a C-terminal amide group (Nhe). ID provides the peptide identifier used in other figures in this chapter.

bonded terms:

$$\begin{aligned}
U(\mathbf{x}) = & \sum_{\text{bonds}} K_r (r - r_{eq})^2 + \sum_{\text{angles}} K_\theta (\theta - \theta_{eq})^2 + \sum_{\text{dihedrals}} \frac{V_n}{2} [1 + \cos(n\phi - \gamma)] \\
& + \sum_{\substack{i < j \\ i,j \notin \Omega_{1-4}}} \left[ \frac{A_{ij}}{r_{ij}^{12}} - \frac{B_{ij}}{r_{ij}^6} + \frac{q_i q_j}{\epsilon r_{ij}} \right] + \sum_{\substack{i < j \\ i,j \in \Omega_{1-4}}} \left[ \frac{1}{S_{nb}} \left( \frac{A_{ij}}{r_{ij}^{12}} - \frac{B_{ij}}{r_{ij}^6} \right) + \frac{1}{S_{ee} \epsilon r_{ij}} \frac{q_i q_j}{\epsilon r_{ij}} \right]
\end{aligned} \tag{3.1}$$

where  $\Omega_{1-4}$  is the set of atom pairs  $(i,j)$  which are separated by three bonds. For example, the parameter  $S_{ee}$  weights the electrostatic interactions in  $\Omega_{1-4}$ ,  $S_{nb}$  weights the corresponding van der Waals interactions, and the dielectric constant  $\epsilon$  affects all longer range electrostatic terms.

In addition, the implicit-solvent model given by the generalized Born approximation [Still et al., 1990, Tsui and Case, 2001] has associated parameters:

$$\Delta G_{solv} = \sum_{a \in \mathcal{A}} \beta_a \alpha_a(\mathbf{x}) + \Delta G_{pol}. \tag{3.2}$$

where  $\mathcal{A}$  is the set of atom types,  $\alpha_a$  is the total solvent-accessible surface area of atoms of type  $a$  in configuration  $\mathbf{x}$ ,  $\beta_a$  are solvation parameters, and the electrostatic

polarization component of the free energy of solvation is given by:

$$\Delta G_{pol} = -\frac{1}{2} \sum_{i,j} \left( \frac{1}{\epsilon_{mol}} - \frac{1}{\epsilon_{water}} \right) \frac{q_i q_j}{f_{GB}(r_{ij})}, \quad (3.3)$$

which involves parameters such as the intra-molecular dielectric constant  $\epsilon_{mol}$  and the solvent dielectric  $\epsilon_{water}$ . (In AMBER, these parameters are specified as  $\epsilon_{in}$ ,  $\epsilon_{ext}$ , and  $\epsilon_{dielc}$ , with  $\epsilon_{water} = \epsilon_{ext}\epsilon_{dielc}$ ,  $\epsilon_{mol} = \epsilon_{in}\epsilon_{dielc}$ , and  $\epsilon = \epsilon_{in}\epsilon_{dielc}$ .) Although in principle these parameters represent physical quantities whose values can be known, in practice they are approximations with values determined individually in empirical or theoretical studies.

The time-step was chosen to be 2fs and SHAKE [Ryckaert et al., 1977] was used (tolerance  $5 \times 10^{-5} \text{\AA}$ ) to constrain hydrogen atoms, and a weakly-coupled heat bath with coupling constant of

$$\lambda = 1 + \frac{\Delta t}{2\tau_T} \left( \frac{T_N}{T} - 1 \right)$$

was used to maintain constant temperature [Berendsen et al., 1984], where  $T_N$  is the fixed reference temperature and  $\tau_T = 1.0$  controls the strength of the coupling. The specific forcefield, solvent, and heat bath parameters used are given in Table 3.2, and are an attempt to replicate as closely as possible a protocol which has previously been successful in simulating helical peptide folding Garcia and Sanbonmatsu [2002], Nymeyer and Garcia [2003]. A key question in the wider use of simulation techniques is whether such parameter sets which are successful in one instance are *generalizable* to other systems; in Section 3.3 we explore this issue by evaluating the use of these parameters to predict experimentally measured helicities for the eight

distinct peptides given in Table 3.1. A more detailed exploration of the effect of varying these parameter choices is described in Chapter 4.

Simul. param.	$\epsilon_{ext}$	$\epsilon_{in}$	Salt conc.	Non-bonded cut-off	$S_{ee}$	$S_{nb}$	$\epsilon_{dielc}$
Default value	78.5	4.0	0.0M	8.0Å	1.2	1.0	1.0

**Table 3.2:** forcefield and simulation parameters used in the helical peptide replica-exchange simulations, and as default values for the parameter sensitivity analysis. Parameters values are those used previously for simulating a helical peptide Nymeyer and Garcia [2003].

Our REMD protocol for this chapter utilizes 30 distinct MD simulations run in parallel at temperatures ranging from the target temperature  $T_0$  ( $273^{\circ}\text{K}$ ,  $276^{\circ}\text{K}$ ,  $277^{\circ}\text{K}$ , or  $298^{\circ}\text{K}$ ) to  $T_{29} = 624^{\circ}\text{K}$  for each peptide simulation. Temperatures are spaced exponentially with  $T_i = \lfloor T_0 \exp[ki] \rfloor$ , where  $k = \ln(624/T_0)/29$  and  $i = 0, \dots, 29$ . During the REMD simulation, each replica is run at the assigned temperature for cycles of 1000 MD steps (2ps), after which the translational and rotational motion of the center of mass is removed and 300 temperature-swapping moves attempted, as an attempt to copy a previous protocol Nymeyer and Garcia [2003] without too heavy a computational cost.

Let  $\mathbf{x}_T = (\mathbf{q}, \mathbf{p})_T$  denote the coordinates (positions and momenta) of the replicate at temperature  $T$ . Each attempted temperature-swap is accepted according to the Metropolis criteria (eq. 2.14), where the energy function  $E(\mathbf{x})$  that defines the Boltzmann distribution (eq. 2.13 over configurations is  $E(\mathbf{x}) = U(\mathbf{q}) + \Delta G_{solv} + \frac{1}{2} \sum_i \|\mathbf{p}_i\|^2/m_i$  with  $U$  the potential function given by (3.1) and  $\Delta G_{solv}$ , the implicit solvent free energy term, given by (3.2). When a swap is accepted the two replicas exchange temperatures, otherwise they remain at their respective temperatures. Associated velocities are rescaled to reflect the temperature swap before the next cycle

of MD steps. This process of 1000 MD steps followed by 300 attempted temperature swaps is repeated until the convergence criteria described in Section 3.2.4 is reached.

The above REMD protocol is used to conform as closely as possible to existing uses of REMD in protein simulation in the literature. The Metropolis criteria is used to guarantee invariance of the Boltzmann ensemble; however, in Chapter 5 we show that corrections are needed to guarantee the proper invariant measure.

## 3.2 Statistical Analysis and Evaluation

Molecular dynamics simulations differ from the use of classical mechanics in macroscopic engineering applications in that the goal is not to produce an accurate physical trajectory of the molecule over time. In fact such trajectories are highly sensitive to starting conditions, parameterizations of the energy model, and other simulation details (see e.g. Braxenthaler et al. [1997]). Instead, it is the long-run time-averaged behavior of the simulation which we can expect to produce observable macroscopic (thermodynamic) physical quantities if the simulation model is adequate. To evaluate simulations against experimental data then, we must be able to accurately compute the long-run time-averaged behavior implied by our theoretical model, specified by the molecular forcefield or potential. To do so, we rely first on an ergodic theorem. The validity of this assumption is further explored in Chapter 5.

The *ergodic theorem* says that if the dynamics of our simulation are ergodic (able to reach any region of the configuration space from any other region), then the time-averaged behavior of the simulation will converge to the configuration space integral representing the ensemble-averaged behavior for any (integrable) quantity

of interest. Writing the quantity of interest as a function  $h(\mathbf{x})$  of configurations  $\mathbf{x}$  in configuration space  $\mathcal{X}$ , we have:

$$\lim_{t \rightarrow \infty} \frac{1}{t} \int_0^t h(\mathbf{x}(s)) \, ds = Z^{-1} \int h(\mathbf{x}) e^{-\frac{1}{k_B T} E(\mathbf{x})} d\mathbf{x} \stackrel{\text{def}}{=} \langle h \rangle_T \quad (3.4)$$

for the canonical (constant N,V,T) ensemble, where  $\langle h \rangle$  denotes the expectation or ensemble average of  $h(\mathbf{x})$  under the stationary Boltzmann distribution. Here  $h(\mathbf{x})$  is any quantity we wish to compute from a given configuration, and may be used to compute means (e.g. internal energy or helicity), variance-covariance matrices (for essential dynamics), indicator functions (for free energies), and so on. A major advantage of simulation-based methods is the ability to calculate a variety of such quantities from a single simulation. The right-hand integral yields the ensemble averaged quantity under the theoretical model (forcefield); it is this quantity that can be compared with real world experiments which are themselves averaged over both time and molecules in solution.

Because we can not run simulations infinitely long, we can only ever compute an approximation to the left-hand side of (3.4). So to use this result in practice, we need to know two things: how long must the simulation be run such that this approximation is “pretty good” (the convergence in (3.4) is approximately achieved), and how good is “pretty good” (error bounds on the computed quantities). Not only must the simulations have reached equilibrium, but they must have run in equilibrium long enough to produce accurate approximations of the time/ensemble averaged quantities of interest. From this perspective, MD simulation is simply a tool for computing the integral (3.4), and often alternative numerical integration methods

such as Monte Carlo sampling or replica-exchange dynamics may be more efficient than standard MD at this task. However these methods often disrupt the *kinetics* of the process; interestingly, recently developed simulation methods which do not guarantee proper ensemble sampling may be useful in taking ensemble samples generated by methods such as MC or REMD and reconstructing the kinetics. Snow et al. [2002].

The second important assumption is statistical, and provides guidance on these questions. It says that for well-behaved functions  $h(\mathbf{x})$  (those having finite variance under Boltzmann distribution  $\pi(\mathbf{x})$ ), and under stronger assumptions on the simulation dynamics (a sufficient condition is geometric ergodicity Tierney [1994]) which are difficult to verify in practice as shown in Chapter 6, the time-average of  $h$  computed from a simulation of  $N$  steps converges to the true value  $\langle h \rangle$  as  $N \rightarrow \infty$ . Moreover, this sample path average obeys a central limit theorem, converging in distribution to a normal random variable centered at the true value  $\langle h \rangle$ :

$$\hat{h} = \frac{1}{N} \sum_t h(\mathbf{x}^{(t)}) \xrightarrow{d} N(\langle h \rangle, \sigma_h^2) \quad \text{where} \quad \sigma_h^2 = \sigma_h^2 [1 + 2 \int_t \rho(t) dt], \quad (3.5)$$

where  $\sigma_h^2 = \langle h^2 \rangle - \langle h \rangle^2$  is the variance of  $h(\mathbf{x})$  under the Boltzmann distribution  $\pi(\mathbf{x})$ , and  $\rho(t) = \langle (h(\mathbf{x}_{t_0}) - h(\mathbf{x}_{t_0+t}))^2 \rangle / \sigma_h^2$  is the auto-correlation function for fluctuations in  $h$  of configurations at time separation  $t$  when the process is in equilibrium. Note that the Metropolis step in REMD creates a stochastic process as discussed in Chapter 5, so we state results in those terms; central limit theorems for deterministic ergodic dynamical systems exist but are somewhat more delicate. Determinism of MD for molecules in solution is artificial and often replaced with stochastic (Langevin

or Brownian) dynamics anyway. In the stochastic case; however, ergodicity of the system is not an assumption but can be shown directly, as seen in Chapter 5.

This theoretical result has important implications. It provides the *distribution* of errors obtained when we use the time average from a finite length simulation to approximate the theoretical ensemble average. This allows us to quantify uncertainty and produce error bars based on  $(100-\alpha)\%$  confidence intervals, which is critical for comparing the simulation output with experimental data. This in turn allows us to determine simulation time needed in order to approximate quantities to a predetermined level of accuracy. Failure to run a simulation long enough to adequately estimate quantities of interest is a common pitfall of molecular dynamics simulation [van Gunsteren and Mark, 1998].

In addition, knowledge that the errors are approximately normally distributed allows us to treat the simulation model as a (rather complicated) statistical model, and perform likelihood-based statistical inference on the simulation parameters, as described in Section 4.1.

### 3.2.1 Interval predictions

A critical aspect of comparing simulation output with experiment is to account for the inherent variability of both the simulation output and the experimental measurement. As described above, variability in the simulation output can be characterized by a central limit theorem: the quantity  $\hat{h}$  approaches  $\langle h \rangle$  in the limit of large  $N$ , with error  $\langle h \rangle - \hat{h}$  being normally distributed with variance  $\sigma_{\hat{h}}^2$  given by (3.5). This result allows us to construct normal-based confidence intervals for  $h$  of the form  $\langle h \rangle \pm 2\hat{\sigma}_{\hat{h}}$ .

The variance of  $\hat{h}$  therefore determines how long we need to run a given simulation to obtain a predetermined level of accuracy. Since  $\sigma_h$  depends on the function  $h$  of interest, some quantities can converge significantly faster than others, a fact observed empirically Smith et al. [2002]; however apparent convergence of some quantities while others have not converged can also be misleading. Theoretical guarantees on how long a simulation must be run are extremely difficult to come by, although recent progress has been made in this area for parallel tempering algorithms Woodard et al. [2008]. To determine this interval we require an estimate  $\hat{\sigma}_{\hat{h}}$  for  $\sigma_{\hat{h}}$ .

### 3.2.2 Integrated Autocorrelation Estimate

One approach we used initially to estimate the variance  $\sigma^2(h)$  was to directly estimate the integrated autocorrelation in (3.5). To do this we estimate the autocorrelation  $C_h(t)$  by its empirical counterpart:

$$\hat{C}_h(t) = \sum_{i=1}^{n-t} \frac{(h_i - \bar{h})(h_{i+t} - \bar{h})}{\hat{\sigma}^2}$$

where  $\hat{\sigma}^2 = \sum_{i=1}^n (h_i - \bar{h})^2$ . Unfortunately, the corresponding estimate of integrated autocorrelation:

$$\hat{I}_{ac} = \sum_{t=1}^T \hat{C}_h(t)$$

is not consistent (has infinite variance in the limit). We also tried a techniques used by Geyer [1992] for Markov chains, forming an estimate by taking the largest  $M$  such that  $\hat{\Gamma}_t = \hat{C}_h(t) + \hat{C}_h(t+1) > 0$  for all positive  $t < M$  and forming the partial sum

$$R = \sum_{t=1}^M \hat{C}_h(t)$$

$$\sigma^2(h) = \frac{1}{\tau} \int_{-\infty}^{\infty} C_h(t) dt \approx \frac{\hat{\sigma}^2}{M} [1 + 2R] \quad (3.6)$$

This method gave us inconsistent results because of the ad hoc choice of the point at which to stop the sum.

### 3.2.3 Batch Estimate

A common and relatively straightforward technique, which we use here, is the *batch* estimate, obtained by dividing the simulation of length  $N$  into  $a = N/M$  regions or *batches* of size  $M$ . Each batch is used to independently estimate  $\langle h \rangle$ :

$$\hat{h}_i = \frac{1}{M} \sum_{k=iM}^{(i+1)M} h(\mathbf{x}_k) \quad \text{and} \quad \hat{h} = \frac{1}{a} \sum_i \hat{h}_i$$

and  $M$  is chosen large enough to ensure the auto-correlation  $\rho_{\hat{h}_i, \hat{h}_{i+1}} \approx 0$ . The batch estimates are then approximately independent samples whose empirical variance

$$\hat{\sigma}_h^2 = \frac{1}{a-1} \sum_i (\bar{h}_i - \hat{h})^2$$

yields a simple estimate of the variance  $\sigma_h^2$ . The quantile plot in Figure 3.1 indicates approximate normality is a reasonable assumption for our converged simulations. The quantile plot compares a plot of the standardized residuals to a Gaussian distribution. Because the points lie along the diagonal line, the assumption that the error approximates a Normal distribution is reasonable.

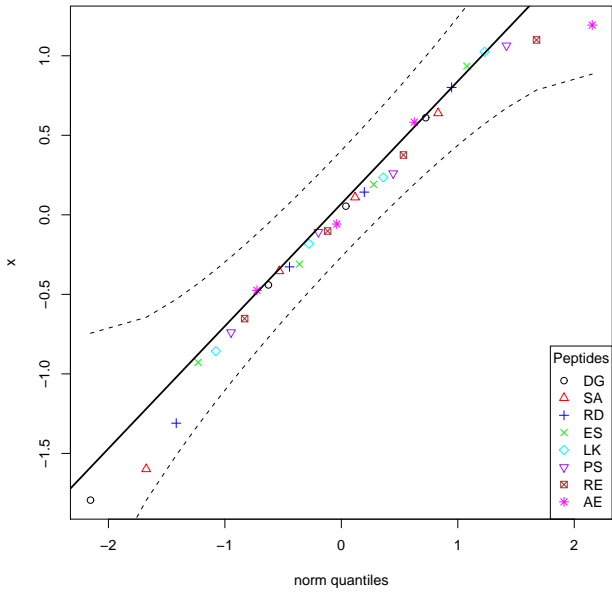


**Figure 3.1:** Quantile plots of standardized residuals  $(\hat{h}_{ij} - \hat{h}_i)/\sigma_{\hat{h}_{ij}}$  for the  $8 \times 4 = 32$  individual REMD simulations. The lack of significant deviation from the diagonal suggests the assumptions of normally distributed noise is reasonable.

### 3.2.4 Monitoring convergence

The energy surface of proteins and polypeptides is characterized by large energy barriers and multiple local minima, making adequate exploration of configuration space a major challenge of protein simulation. While theoretical guarantees are very difficult to obtain for complex simulations, and observing the output of a simulation can never guarantee convergence, convergence diagnostics can be constructed to identify *lack of* convergence from simulation output. Our preferred approach is the use of multiple parallel simulations starting from diverse initial conditions in order to monitor the convergence by comparison of sample path quantities across distinct simulations. We use the multiple-chain approach Gelman and Rubin [1992] to assess convergence of our simulations by running multiple independent REMD simulations

for each peptide in parallel starting from a diverse set of initial configurations, with each individual REMD simulation run according to the protocol of Section 3.1. Let  $M$  denote the number of simulations and  $\mathbf{x}_j^{(i)}$  for  $j = 1, \dots, M$  the configuration of the  $j^{\text{th}}$  simulation at time step  $i$ . Convergence of an observable quantity  $h(\mathbf{x})$  is shown by calculating

$$B_N = \frac{1}{M} \sum_{j=1}^M (\bar{h}_j - \bar{h})^2 \quad \text{and} \quad W_N = \frac{1}{NM} \sum_{j=1}^M \sum_{i=1}^N (h(\mathbf{x}_j^{(i)}) - \bar{h}_j)^2,$$

with  $\bar{h}_j = \frac{1}{N} \sum_{i=1}^N h_j^{(i)}$ , and  $\bar{h} = \frac{1}{M} \sum_{j=1}^M \bar{h}_j$ .  $B_N$  represents the *between-chain* variability and  $W_N$  represents the *within-chain* variability. When multiple starting configurations are chosen to be widely dispersed throughout configuration space, early in the simulation the chains will be sampling distinct regions of phase space and the between-chain variance will be significantly higher than the within-chain. As the simulations converge to sampling from the same equilibrium Boltzmann distribution, these two quantities will converge. Comparison is based on techniques from the analysis of variance to determine whether significant differences remain. The quantities

$$\hat{\sigma}_N^2 = \left( \frac{N-1}{N} W_N + B_N \right) \quad \text{and} \quad W_N$$

give upper and lower bounds for the variance of the quantity of interest over the simulation and convergence is monitored using the Gelman-Rubin *shrink factor*

$$\sqrt{R_N} = \sqrt{\frac{N-1}{N} + \frac{M+1}{M} \frac{B_N}{W_N} \frac{v_N}{v_N - 2}},$$

where  $v_N = 2(\hat{\sigma}_N^2 + \frac{B_N}{M})^2/W_N$ . The quantity  $\sqrt{R_N}$  estimates the reduction in variance of the estimator  $\hat{h}$  if the simulation were to be run infinitely long, and converges to one as all of the parallel simulations converge to equilibrium.

Once the chains have equilibrated, samples from all  $M = 4$  independent simulations can be combined to obtain a pooled estimate of  $\langle h \rangle$ , with individual chain estimates combined inversely proportional their respective variances:

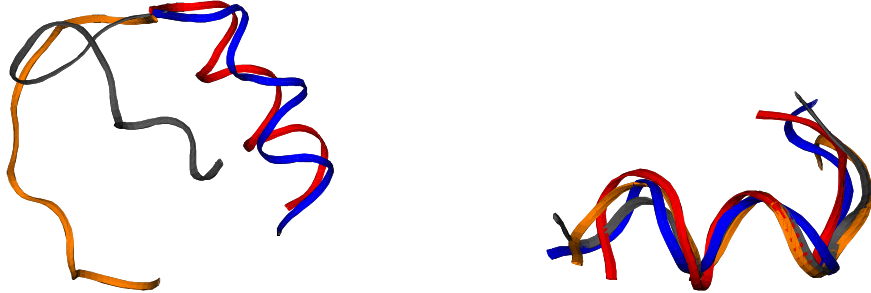
$$\hat{h} = \frac{\sum_j \hat{h}_j \hat{\sigma}_{\hat{h}_j}^{-2}}{\sum_j \hat{\sigma}_{\hat{h}_j}^{-2}} \quad \text{and} \quad \hat{\sigma}_h^2 = \left( \sum_j \hat{\sigma}_{\hat{h}_j}^{-2} \right)^{-1}. \quad (3.7)$$

Thus the effective trajectory length of the combined estimate is  $M\bar{N}$  where  $\bar{N}$  is the average production phase length; the only price paid for using multiple simulations compared to a single simulation is the replication of the equilibration phase. In our opinion, the advantage of being able to run in parallel and to obtain convergence diagnostics by inter-run comparisons far outweighs this cost in most situations. Note that combining the results of multiple simulations who have not been determined to have individually converged to the same stationary distribution, as is sometimes done in MD simulation, has no theoretical justification and can be badly misleading.

Numerous other convergence diagnostics have been developed in the statistics and operations research literature Cowles and Carlin [1996], including further developments of the approach used here Brooks and Gelman [1998], Fan et al. [2006]. Note that no diagnostic based on simulation output can ever guarantee convergence, all such diagnostics can be fooled Cowles and Carlin [1996]. However theoretical bounds on simulation time are very difficult to obtain; although relevant work in this direction is ongoing Woodard et al. [2008].

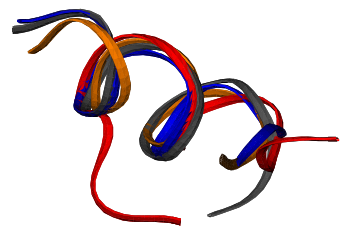
### 3.3 Results

REMD simulations were performed for the eight peptides given in Table 3.1. For each peptide, four REMD simulations were run in parallel, with each REMD simulation utilizing 30 temperatures according to the protocol of Section 3.1. Initial configurations for the four REMD runs were generated as follows for each peptide: one ideal helix; one extended conformation; and two random configurations, one generated by uniformly sampling  $(\phi, \psi)$  angles within the helical range and one generated by uniformly sampling  $(\phi, \psi)$  outside of the helical range. Figure 3.2(a) shows the starting configurations for a particular peptide at  $T_0$ . Initial velocities were generated randomly and independently for each configuration. Quantities monitored for convergence included backbone  $\phi$ - and  $\psi$ -angles of each amino acid, helicity of the peptide, and total energy. Convergence to equilibrium was declared when the Gelman-Rubin shrink factor for these quantities reached 1.1, and the sample paths up to this time (equilibration phase) discarded. Sample paths from this time on (production phase) were included in computing time-averaged quantities  $\hat{h}$ . Figure 3.3 shows plots of the Gelman-Rubin shrink factor for simulations of the eight peptides; for comparison a standard MD simulation (without replica-exchange) of one of the peptides is shown.



(a)

(b)



(c)

**Figure 3.2:** Three configuration snapshots from the four parallel REMD simulations of peptide SAEDAMRTAGGA. Shown are (a) the four starting configurations, (b) four configurations observed at time of convergence to equilibrium, and (c) four configurations from the experiment phase of the simulation.

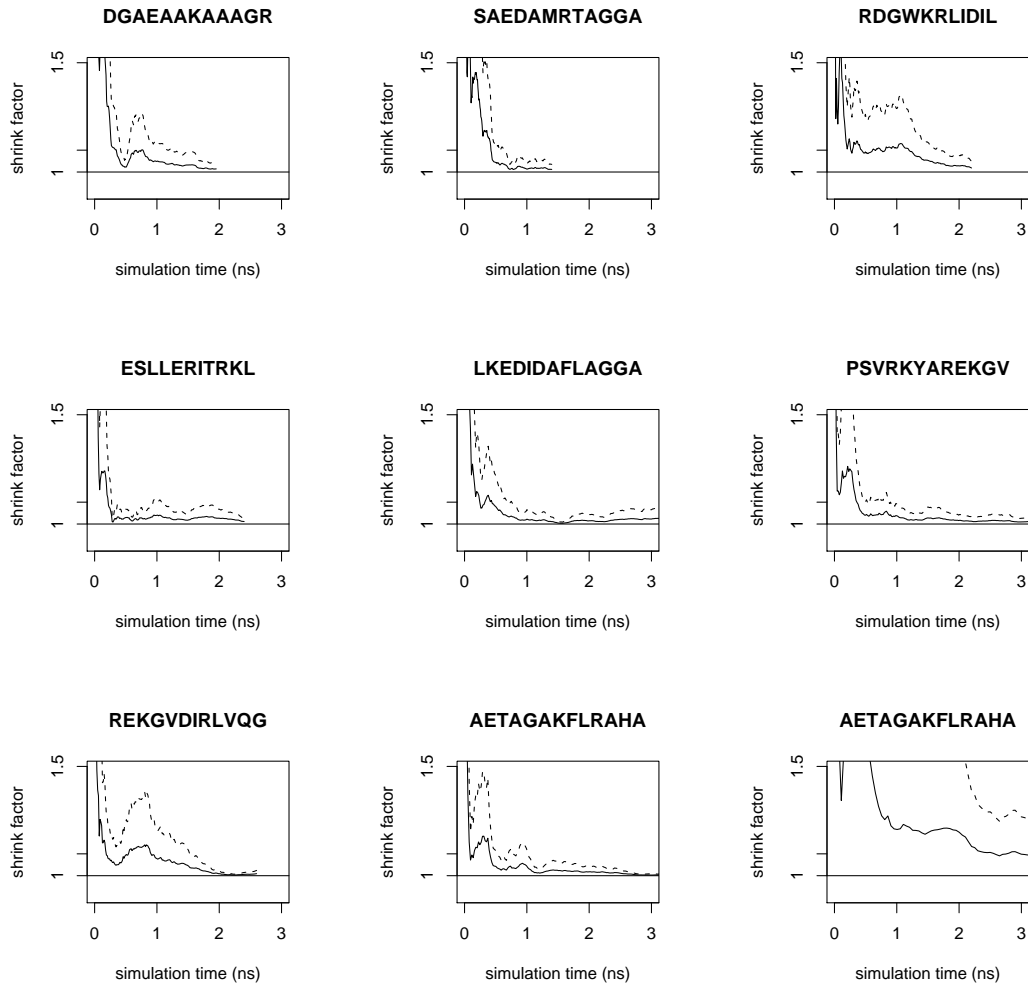


**Figure 3.3:** Convergence of REMD simulations of the eight peptides from Table 3.1, as measured by the Gelman-Rubin shrink factor for helical content. Plots represent convergence between 4 parallel simulations started from diverse initial configurations using parameters given in Table 3.2. Shown for comparison is a convergence plot for 4 standard MD simulations of peptide AE simulated without replica-exchange.

Helicity of a peptide configuration was defined as the fraction of amino acid  $(\phi, \psi)$  pairs lying in a predefined helical range with the potential to form hydrogen bonds:

$$h(\mathbf{x}) = \frac{1}{(l-2)} \sum_{i=2}^{l-1} \prod_{j=i-1}^{i+1} \mathbf{1}_{(\phi_{lo} \leq \phi(x_j) \leq \phi_{hi})} \mathbf{1}_{(\psi_{lo} \leq \psi(x_j) \leq \psi_{hi})} \quad (3.8)$$

for configuration  $\mathbf{x}$  of a peptide of length  $l$ , where  $\mathbf{1}_()$  is an indicator function. We use a standard range for defining helical angles:  $\{\phi_{lo}, \phi_{hi}\} = \{-87, -27\}$  and  $\{\psi_{lo}, \psi_{hi}\} = \{-77, -17\}$ ; see Section 4.1.3 for the effect of changing these boundaries on the resulting helicities.

Another method we considered for measuring helicity was based on Shalongo and Stellwagen [1997]. They measure whether an amino acid is helical by determining whether the  $\phi$  and  $\psi$  angles lie within a particular range. Then, they use a neighbor model to calculate the ellipticity of each amino acid. If an amino acid is helical and has two helical neighbors its ellipticity is  $e_2 = -40000$ , if it is helical and only has one helical neighbor its ellipticity is  $e_1 = -11200$ , and if it has no helical neighbors its ellipticity is 0. After calculating the ellipticity of the entire peptide  $e_{pep}$ , they convert to a helicity measure given by:

$$H_{mol} = (1/n) * (e_{pep} - e_c) / (-42500.0 * (1.0 - 3.0/n) - e_c) \quad (3.9)$$

where  $e_c = 640$  and  $n$  is the number of amino acids in the peptide. We can see in Figure 3.4 that this measurement over-estimates the helicity of the peptide simulations for each of the eight peptides run with the default parameter values given in Table 3.2.

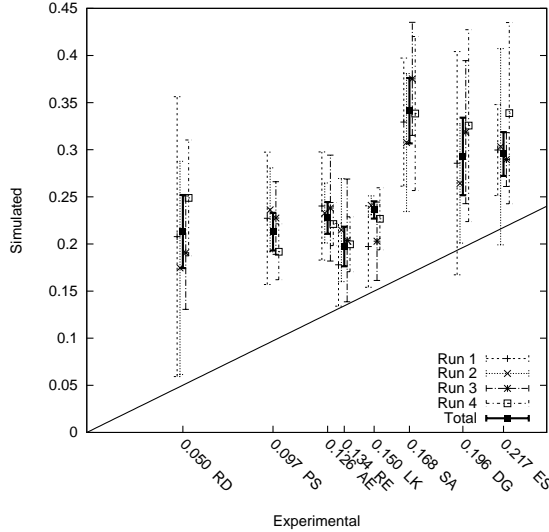


**Figure 3.4:** Peptide helicity as estimated from simulation using the method of Shallowo and Stellwagen [1997] versus experimentally measured helicity for the eight peptides in Table 3.1. The diagonal line  $y = x$  is shown as a reference. Simulation results are shown as 95% confidence intervals using standard errors estimates described in text, and are shown both for individual REMD runs and for the pooled estimates.

The total simulation time required to reach convergence for each peptide is shown in Table 3.3. After equilibration, each simulation was continued until the estimated variance  $\hat{\sigma}_h^2$  of the combined estimate of equilibrium helicity (3.7) decreased below 0.001. The total simulation times required in the production phase to meet this criteria are also shown in Table 3.3.

Peptide	DG	SA	RD	ES	LK	PS	RE	AE
Equilibration phase (ns)	0.8	0.6	0.8	0.8	1.0	1.0	1.0	1.4
Production phase (ns)	1.0	0.8	1.4	1.6	2.4	2.4	1.6	2.9

**Table 3.3:** Time length of equilibration and production phases for REMD simulations of each peptide; peptide identifiers are given in Table 3.1. Equilibration and production times were determined according to the statistical convergence criteria described in Section 3.2.4. Due to the use of replica-exchange, equilibration is significantly faster than physical timescales (see Figure 3.3).

Figure 3.5 shows the simulated equilibrium helicities versus the published ex-

perimental helicities in Table 3.1. All experimental helicities are derived from mean residue  $\theta_{222}$  ellipticity measured by circular dichroism. Simulated helicities are shown with 95% confidence intervals obtained as described in Section 3.2.1. For each peptide, we show the helicity interval obtained from each of the four independent REMD runs as well as the combined estimate  $\hat{h}$  (3.7). Simulated helicities are correlated with the experimental helicities but are not within perfect agreement even within sampling error of the simulations. Recent estimates place the standard deviation of experimental noise to be around .05, so the simulations may agree within the tolerance of combined noise due to finite simulation sampling *and* experimental error.

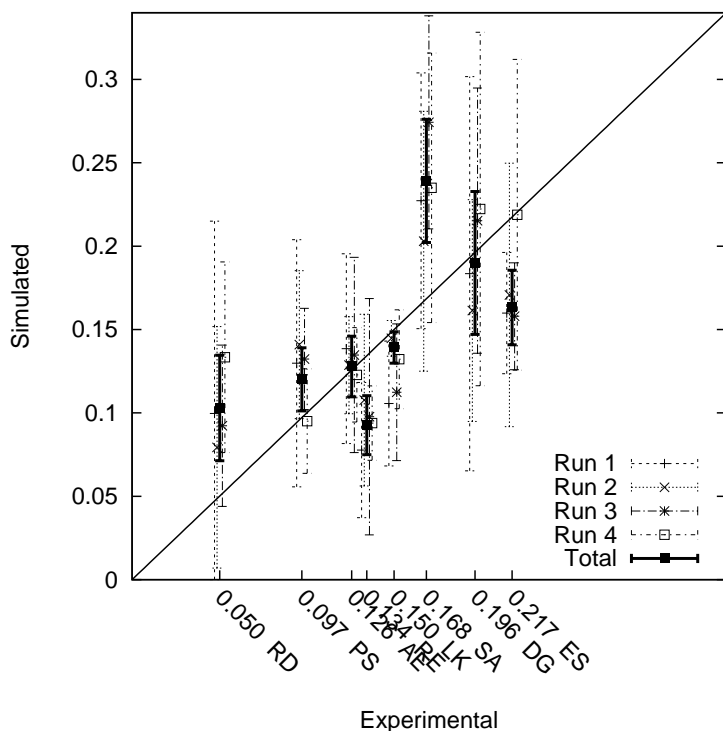


**Figure 3.5:** Peptide helicity as estimated from simulation versus experimentally measured helicity for the eight peptides in Table 3.1. The diagonal line  $y = x$  is shown as a reference. Simulation results are shown as 95% confidence intervals using standard errors estimates described in text, and are shown both for individual REMD runs and for the pooled estimates.

In this chapter we ran simulations for eight helical peptides with typical simulation parameters using a replica-exchange algorithm popular in the field. We used statistical methods to estimate convergence of our simulations and to compare our simulations with experiment. In the following chapters we start to question the fundamental assumptions used to make these comparisons. In the next chapter we start by questioning the parameters that define the simulation, asking how small changes in these parameters affect key simulation averages.

# Chapter 4

## Determination of Simulation Parameters

We begin this chapter by giving an example of using experimental results to statistically measure the effect of parameter changes on simulation results. After identifying two parameters,  $\epsilon_{in}$  and  $S_{nb}$ , with strong effects on REMD simulations, we explain the possible causes for these parameter effects using biochemical intuition and mathematical tools. We then further explore the effects of the parameter associated with the implicit solvent,  $\epsilon_{in}$ , by running lengthy replica-exchange simulations in parallel for eight helical peptides. For each peptide, we ran four replica-exchange simulations, each with 30 temperatures, for each of the six total chosen values of  $\epsilon_{in}$ . Each of these simulations were run for both the number of steps needed for convergence plus a number of steps from which to gather simulation data. Thus  $4 \times 6 \times 8 = 192$  replica-exchange simulations were run to gather the data used to estimate the  $\epsilon_{in}$  parameter. By running these simulations to use Bayesian estimation to choose the value that reflects the experimental results most accurately, we are able both to demonstrate a technique for refining parameter values and to underscore the need for more diligent justification of the myriad of parameter values used for dynamics

simulations.

We then give another example of parameter adaptation using the endpoints of the numerical range for helical  $\phi$  and  $\psi$  angles. The ranges we use in calculating helicity are based on past simulation papers [Garcia and Sanbonmatsu, 2002, Sorin and Pande, 2005a]. Nonetheless, there are other ranges being used in the literature, [Nymeyer and Garcia, 2003, Hansmann and Okamoto, 1999, Jas and Kuczera, 2004] and a consensus for measuring helicity with numerical ranges has not been reached. To test these ranges, we assume a uniform prior over all possible values of  $(\phi_{lo}, \phi_{hi}, \psi_{lo}, \psi_{hi})$  such that  $\phi_{lo} < \phi_{hi}$  and  $\psi_{lo} < \psi_{hi}$ . We then calculate the posterior distribution by measuring the difference between the experimental helicity and the simulated helicities using each set of bounds for  $\phi$  and  $\psi$ . This allows us to calculate the posterior distribution without running additional simulations, instead we are able to use the existing simulations.

Finally we use cross-validation to estimate the accuracy of our predictions for the parameter  $\epsilon_{in}$ . We remove one peptide at a time, calculating the posterior distribution based on the remaining peptides. Then by using the predicted value based on the resulting posterior distribution for the removed peptide, we calculate the mean squared error of using the predicted value. This error then gives an estimate for the predictive value of the best parameter value.

## 4.1 Parameter Adaptation

The energetics used in the above simulations involve a large number of parameters which must be specified in advance. The parameters associated with the AMBER94

energy potential are detailed in Section 3.1. The simulations of Section 3.3 utilize a default set of parameters given in Table 3.2, chosen to comply with standard practice as described in Section 3.1. Nevertheless, there is significant variation in the literature in values chosen for some of these parameters. Since the ensemble simulated is defined by these parameters, the simulation averages obtained and their comparison with experimental values will be a function of these parameter choices. It is therefore important to understand how the differences in these parameter values may be propagated into the resulting thermodynamic quantities estimated, and to determine the impact on the conclusions obtained.

#### 4.1.1 Sensitivity Analysis

To address the questions of sensitivity of simulation results to choice of simulation parameters described in the last section, we performed a one-way sensitivity analysis of six of the forcefield parameters described there: the external and internal dielectrics  $\epsilon_{ext}$  and  $\epsilon_{in}$ , the salt concentration constant used with implicit solvent, the weight terms  $S_{ee}$  and  $S_{nb}$ , for atom pairs in  $\Omega_{1-4}$ , and the dielectric constant  $\epsilon_{diec}$ , in addition to a simulation parameter: the non-bonded cutoff distance. Ranges for these parameters were chosen based on the variation in use in published simulation studies and recommended values in forcefield documentation.

Sensitivity analysis was performed via short REMD simulations of two peptides (DGAEAAKAAAGR and SAEDAMRTAGGA) starting from equilibrium states obtained from the longer simulations of Section 3.3. Parameters given in Table 3.2 were used as reference values, and each parameter was varied individually while holding

the others constant, performing short REMD simulations of 200ps for each peptide at 273K. Four copies of each were run from different equilibrium starting configurations to monitor convergence as described in Section 3.2.4. The resulting sensitivity of helicity to perturbations of these seven parameters is shown in Table 4.1. Of the parameters examined, the internal dielectric constant  $\epsilon_{in}$  has the most dramatic effect on the helicity obtained from simulation.

The results in Table 4.1 suggest that the variability among choices for both  $\epsilon_{in}$  and  $S_{nb}$  observed in the literature may significantly impact the thermodynamic quantities measured from these simulations. To evaluate the ability of this potential and solvent model to reproduce experimental helicities, we must obtain an appropriate consistent value for this and other parameters.

#### 4.1.2 Effect of $\epsilon_{in}$ and $S_{nb}$ Parameters

Variation of the two forcefield parameters  $\epsilon_{in}$  and  $S_{nb}$  showed a significant impact on the helicity of the two peptides studied in the one-way sensitivity analysis. We focus on determining an appropriate value for  $\epsilon_{in}$  in Section 4.1.3, but first we explore here the manner in which these parameters affect helicity. The value of  $\epsilon_{in}$  affects both the solute-solvent electrostatic polarization term in (3.3) and non-bonded electrostatic interactions in (3.1). The  $\Delta G_{pol}$  term represents a difference in electrostatic interaction energy resulting from solvent screening of charges. As  $\epsilon_{in}$  increases towards  $\epsilon_{ext}$  this difference shrinks, effectively increasing internal charge screening by making the interior of the molecule more polar. The electrostatic interactions in (3.1) also decrease as  $\epsilon_{in}$  increases, reducing the favorability of hydrogen bonds formed in helix

		DGAEAAKAAAGR		SAEDAMRTAGGA	
Parameter	Value	Mean	Variance	Mean	Variance
$\epsilon_{ext}$	100	0.188	0.0006	0.170	0.0183
	80	0.189	0.0024	0.209	0.0060
	78.5	0.170	0.0031	0.174	0.0183
	50	0.172	0.0006	0.232	0.0050
$\epsilon_{in}$	20	0.063	0.0002	0.091	0.0035
	10	0.124	0.0003	0.138	0.0087
	4	0.168	0.0021	0.177	0.0191
	3	0.260	0.0003	0.226	0.0110
	1	0.388	0.0037	0.227	0.0112
Salt	5.0	0.197	0.0015	0.219	0.0065
	2.0	0.161	0.0005	0.146	0.0188
	1.0	0.173	0.0002	0.186	0.0204
$S_{ee}$	5.0	0.238	0.0004	0.262	0.0197
	2.0	0.215	0.0010	0.235	0.0094
	1.5	0.179	0.0002	0.197	0.0184
	1.2	0.188	0.0016	0.176	0.0188
	1.0	0.161	0.0010	0.192	0.0155
$S_{nb}$	5.0	0.052	0.0001	0.039	0.0003
	2.0	0.109	0.0016	0.104	0.0070
	1.5	0.171	0.0009	0.093	0.0043
	1.2	0.176	0.0018	0.158	0.0122
	1.0	0.202	0.0006	0.175	0.0188
Cut-Off	99.0	0.167	0.0007	0.167	0.0254
	20.0	0.183	0.0008	0.173	0.0200
	15.0	0.177	0.0002	0.199	0.0230
	12.0	0.181	0.0004	0.228	0.0315
	10.0	0.171	0.0009	0.167	0.0160
	8.0	0.161	0.0002	0.209	0.0130
	5.0	0.111	0.0002	0.112	0.0052
$\epsilon_{dielc}$	100.0	0.059	0.0002	0.060	0.0015
	80.0	0.052	0.0009	0.089	0.0046
	78.5	0.065	0.0010	0.125	0.0039
	50.0	0.093	0.0011	0.105	0.0072
	20.0	0.091	0.0003	0.067	0.0039
	5.0	0.074	0.0011	0.115	0.0071
	3.0	0.083	0.0011	0.119	0.0111

**Table 4.1:** One-way sensitivity analysis of helicity as a function of simulation parameters. Shown are mean helicity and variance obtained for two peptides DGAEAAKAAAGR and SAEDAMRTAGGA at a range of values for each parameter studied.

formation. Thus we expect that increasing  $\epsilon_{in}$  will produce lower simulation helicity levels, as observed in Table 4.1. (Sensitivity to much larger changes in the structure of the solvation model has been previously reported [Peng and Hansmann, 2002, Nymeyer and Garcia, 2003], but our results show that even for a given solvation model the choice of parameter values may have a large impact.)

In contrast, Table 4.1 shows that as  $S_{nb}$  increases, peptide helicity decreases.  $S_{nb}$  scales the non-bonded Van der Waals interactions in the potential energy  $U$  (3.1). To interpret the effect of this parameter on helicity we examined its effect on each of the 1-4 interactions along the peptide backbone, as well as the relation of these 1-4 distances to amino acid helicity. The effect of the  $S_{nb}$  parameter on most 1-4 interactions had little effect on helicity, with the notable exceptions of nitrogen-to-nitrogen (N-N) and hydrogen-to-carbon (H-C) distances, as pictured in Figure 4.1. Equilibrium values of both of these distances (N-N and H-C) decrease as

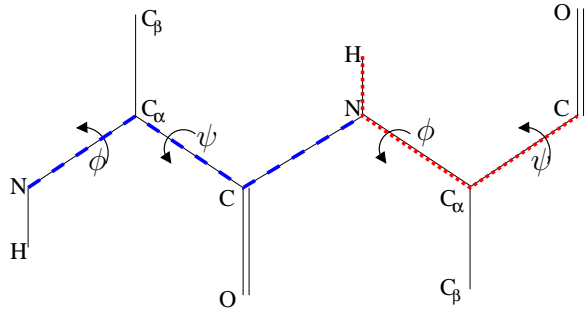


**Figure 4.1:** The N-N (blue) and H-C (red) 1-4 interactions along the peptide backbone, which are most affected by changes in the  $S_{nb}$  scaling constant in the AMBER potential. The effect of equilibrium distances for these atom pairs has a significant effect on the  $(\phi, \psi)$  angles of their respective amino acids, and hence on peptide helicity.

$S_{nb}$  increases, which in turn lowers the helicity of the associated amino acid as shown in Figure 4.2 in both peptides for which this sensitivity analysis was performed.

Changes in other 1-4 atom pair distances induced by  $S_{nb}$  increase had little effect on helicity; C <sub>$\alpha$</sub> -C <sub>$\alpha$</sub>  is shown as an example.

#### 4.1.3 Bayesian estimation of simulation parameters

Given the sensitivity of simulation results to certain forcefield parameters as demonstrated in Section 4.1.1, we would like to identify a standard set of values that could be used by various researchers to ensure consistency and comparability of simulations across different studies. A natural approach to determine such values is to optimize the parameter values with reference to experimental data. However, it is important to do so in such a way that the resulting parameter values are *generalizable* to other systems. A criticism commonly leveled at simulation research is that with the large number of parameters involved in specifying a potential energy function, a solvation model, and a simulation algorithm, the simulation may be adjusted to produce almost any behavior the investigator desires.

Such concerns can be addressed by standardized use of a common set of parameters, but the adaptation of these parameters to better match experimental observations remains important. The danger is that optimizing parameters on a specific set of data may provide good results, but generalize poorly to the study of other systems, a phenomenon known as *over-fitting*. One solution to over-fitting is the use of large datasets relative to the number of parameters, where the simultaneous adaptation to multiple experimental measurements ensures that no particular measurements are well-described at the expense of others. In fact we have large quantities of experimental helicity data available Schmidler et al. [2007], but we are

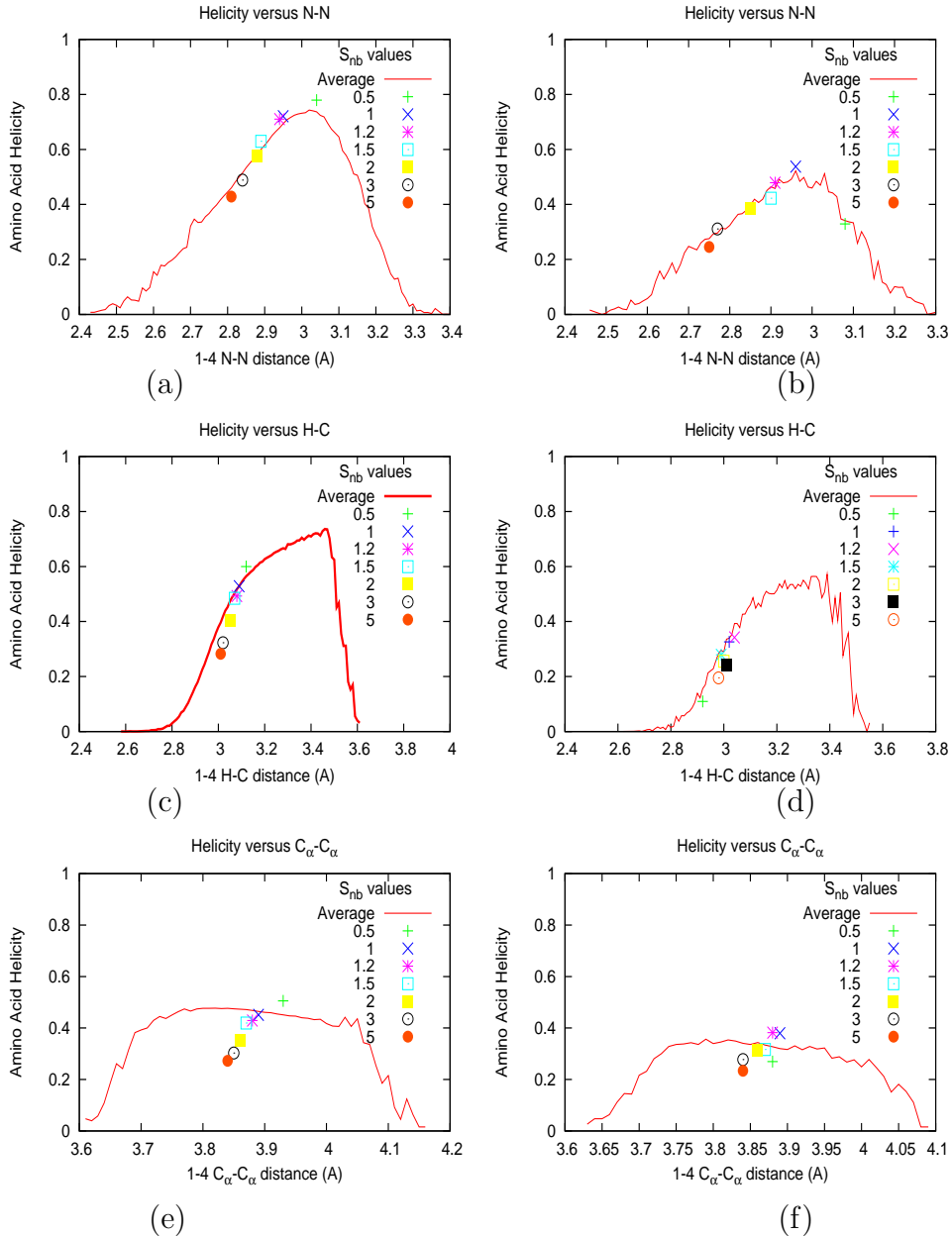


**Figure 4.2:** Effects of the non-bonded scaling parameter  $S_{nb}$  on the equilibrium distances of successive backbone nitrogen atoms (N-N), hydrogen-carbon atom pairs (H-C), and  $\alpha$ -carbons ( $C_\alpha$ - $C_\alpha$ ). Line represents the ensemble-mean helicity for the  $i^{th}$  amino acid as a function of the  $N_i$ - $N_{i+1}$  distance (plots a,b),  $H_i$ - $C_i$  distance (c,d), or  $C_\alpha$ - $C_\alpha$  distance (e,f) for the two peptides DGAEAAKAAAGR (a,c,e) and SAEDAM-RTAGGA (b,d,f). Individually labeled points give the average N-N or H-C distance for simulations with  $S_{nb} = \{0.5, 1, 1.2, 1.5, 2, 3, 5\}$ . Helicity changes in response to varying  $S_{nb}$  can be explained by sensitivity to N-N and H-C distances; other 1-4 atom pairs have little effect on helicity as demonstrated here for  $C_\alpha$ - $C_\alpha$ .

currently limited by the fact that each data point requires parallel simulations at nanosecond or greater timescales for inclusion. However over-fitting is also avoided by a variety of parameter estimation and predictive validation techniques developed in statistics, such as Bayesian analysis and regularization. These techniques, which penalize large parameter changes when insufficient data is available to justify them, regularly allow the adaptation of complex many-parameter models to relatively small data sets while avoiding over-fitting and producing parameters which generalize well. In this section we adopt a Bayesian approach, using prior information to adapt the parameters by Bayesian inference. Because computational considerations limit us to the use of the eight peptides in Table 3.1, we perform only a small example of this approach, adapting only one parameter at a time.

To evaluate generalizability of the parameters resulting from this adaptation approach, we apply the statistical method of cross-validation. This allows us to estimate *out-of-sample* prediction accuracy, or how accurately we can expect these parameters to perform when simulating a new peptide to predict its experimental helicity.

We first specify a simple statistical error model for the experimental data, which says that the measured helicities may be described as a combination of the theoretical equilibrium helicity under our forcefield, plus some experimental noise:

$$h_R^{exp} = \langle h_R \rangle_\theta + \varepsilon \quad \varepsilon \sim N(0, \sigma^2). \quad (4.1)$$

Here  $h_R^{exp}$  denotes the experimentally measured helicity of peptide  $R$ , and we now denote explicitly the dependence of  $\langle h \rangle$  on the peptide sequence  $R$  as well as the forcefield parameters  $\theta$ . If  $\langle h_R \rangle_\theta$  was a linear function of the parameters  $\theta$ , then (4.1) would simply be a linear regression model. Instead, the ensemble helicity  $\langle h_R \rangle_\theta$

is a complicated function given by the configuration integral under the Boltzmann distribution with potential function (3.1) parameterized by  $\theta$ . But similar statistical principles apply, allowing us to estimate the parameters  $\theta$  from data, with a slightly unique aspect arising from the difficulty in calculating  $\langle h_R \rangle_\theta$ , which can only be done approximately by the simulation average from a finite length simulation as described in Section 3.2.1. The assumption of normally distributed noise can be justified by the previously described central limit theorem for  $\langle \hat{h}_R \rangle$  as well as standard usage for experimental noise; the quantile plot in Figure 4.3 shows that this assumption is quite reasonable.

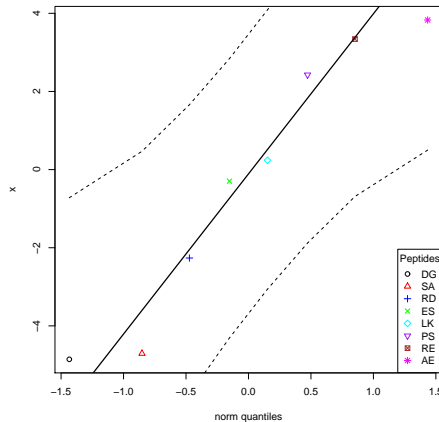


**Figure 4.3:** Quantile plots of standardized residuals  $(\hat{h}_i - h_i^{exp})/\sigma_{\hat{h}_i}$  for the eight combined simulation peptide helicities versus experiment. The lack of significant deviation from the diagonal suggests the assumptions of normally distributed noise is reasonable.

The Bayesian approach next specifies a prior distribution for the parameter  $P(\theta)$  which captures any background or biophysical knowledge we may have about the parameter, to supplement the information contained in the experimental data. We

then base our inference about the parameter on the posterior distribution:

$$P(\theta | \text{Data}) = \frac{P(\text{Data} | \theta)P(\theta)}{\int P(\text{Data} | \theta')P(\theta')d\theta'} \propto P(\theta) \prod_{i=1}^p \phi \left( \frac{\hat{h}_i^\theta - h_i^{\exp}}{\sigma_{\exp} + \sigma_{\hat{h}_i^\theta}} \right), \quad (4.2)$$

where  $p$  is the number of peptides,  $\phi$  is standard normal density function, and  $\hat{h}_i^\theta$  is the simulated helicity (3.7) for peptide  $i$  run at parameter value  $\theta$ . Note that  $\sigma_{\exp}^2$  reflects the variance in  $h_i^{\exp}$  arising from experimental noise, and  $\sigma_{\hat{h}_i^\theta}$  is the remaining simulation uncertainty in  $\hat{h}_i^\theta$  given in (3.7). We use the estimated Schmidler et al. [2007] value  $\sigma_{\exp} = .07$  for convenience; more formally  $\sigma_{\exp}$  could be estimated or integrated out to obtain the marginal posterior distribution [Gelman et al., 2004].

## Internal dielectric

To demonstrate this approach to parameter adaptation, we applied it to estimate the parameter  $\epsilon_{in}$  which was shown in Table 4.1 to have the most significant impact on equilibrium helicity. To estimate an optimal value for internal dielectric we discretized this parameter into a set of plausible values  $\epsilon_{in} \in \{1, 2, 3, 4, 5\}$  spanning the range of values which have been used previously in the literature [Nymeyer and Garcia, 2003, Sorin and Pande, 2005a]. A non-informative uniform prior distribution was assigned for  $\epsilon_{in}$  by giving each possible value of  $\epsilon_{in}$  equal prior probability. To obtain the posterior distribution (4.2) for  $\epsilon_{in}$ , REMD simulations as described in Section 3.1 were then run for each peptide at each discrete value of the dielectric constant with all other parameters fixed at their default values given in Table 3.2. The resulting posterior distribution over the discrete values of  $\epsilon_{in}$  is shown in Figure 4.4a. Given this shape, we decided to refine the discretization of  $\epsilon_{in}$  by adding

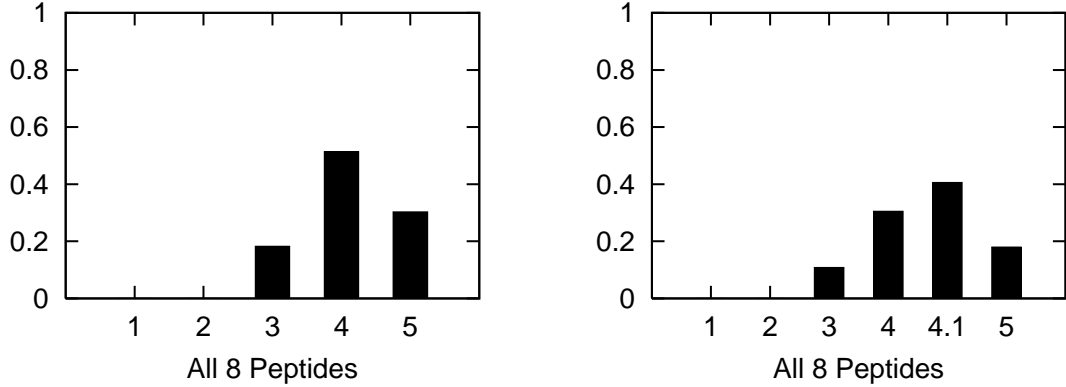


**Figure 4.4:** Posterior distributions for the dielectric constant  $\epsilon_{in}$  evaluated at discrete values, obtained using Bayesian parameter updating described in Section 4.1.3 under uniform prior. (a) Posterior over  $\epsilon_{in} \in \{1, 2, 3, 4, 5\}$ . (b) An additional simulation was run at  $\epsilon_{in} = 4.1$  to help identify the mode of the posterior distribution.

another value at  $\epsilon_{in} = 4.1$  to obtain a more detailed look at the posterior in the high probability region. (Each such point requires 8 peptides  $\times$  4 REMD runs  $\times$  30 MD replicas run to convergence to obtain equilibrium helicities, hence the coarseness of the original discretization.) The new posterior is shown in Figure 4.4b.

Figure 4.5 shows estimated helicities obtained by simulation versus experimental values for all eight peptides for the six different values of  $\epsilon_{in}$ , where it can be seen that the highest posterior probability value of 4.1 is the one which gives the closest approximation to the *set of* experimental values. Figure 4.6 plots the simulated helicity versus the experimental helicity individually for the eight peptides plotted at the different values of  $\epsilon_{in}$ . Figure 4.4b shows that resulting posterior distribution is clearly peaked at 4.1. (Note that further refinement of the discretization may well lead to an improvement between 4.0-4.1 or 4.1-5.) As more experimental data and associated simulations are included, this posterior distribution can be updated to reflect the information in the larger data set, further refining the optimal value.

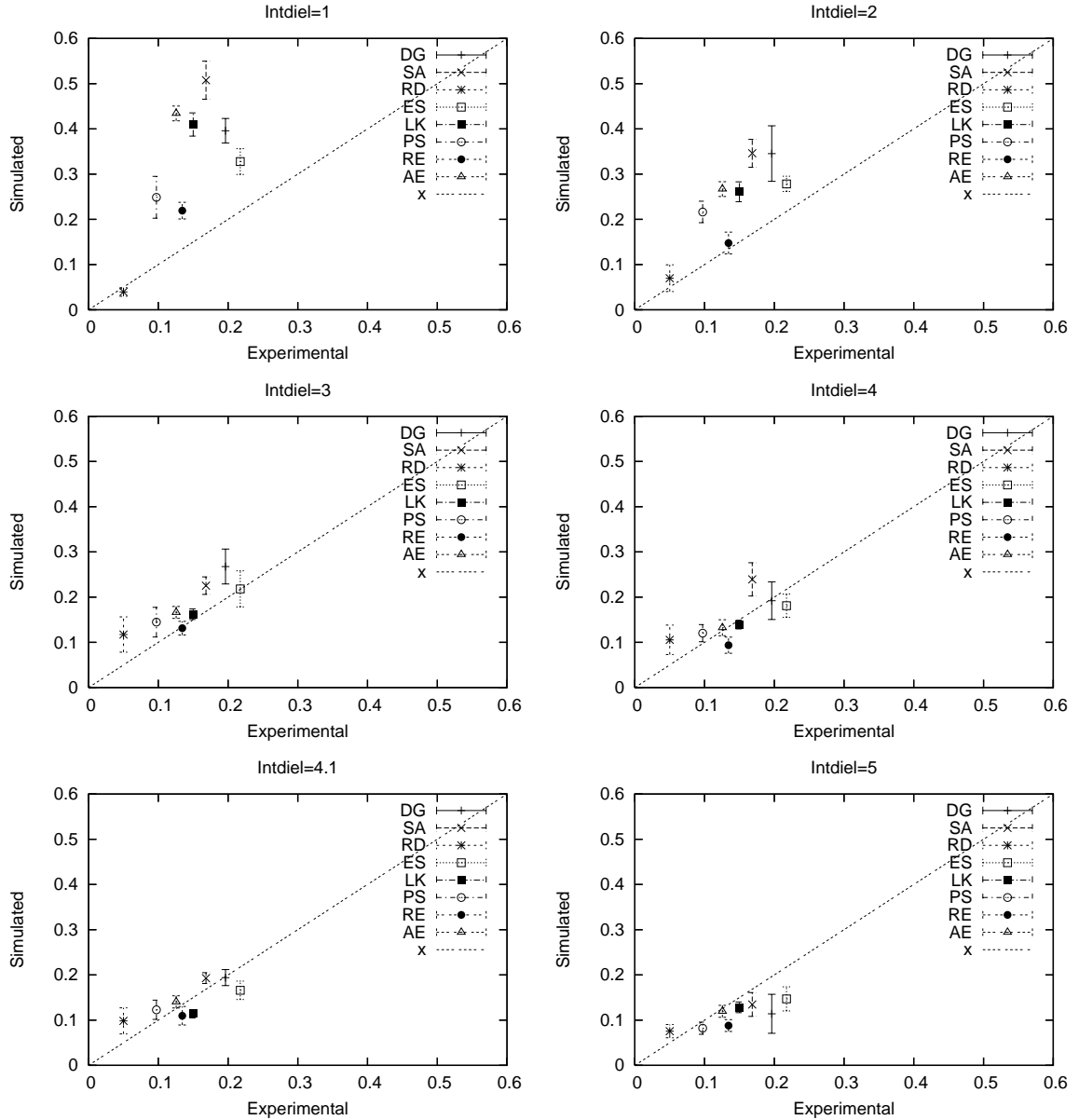


**Figure 4.5:** Simulated helicity versus experimental helicity for the peptides in Table 3.1 evaluated at a range of values of the internal dielectric parameter  $\epsilon_{in}$ .

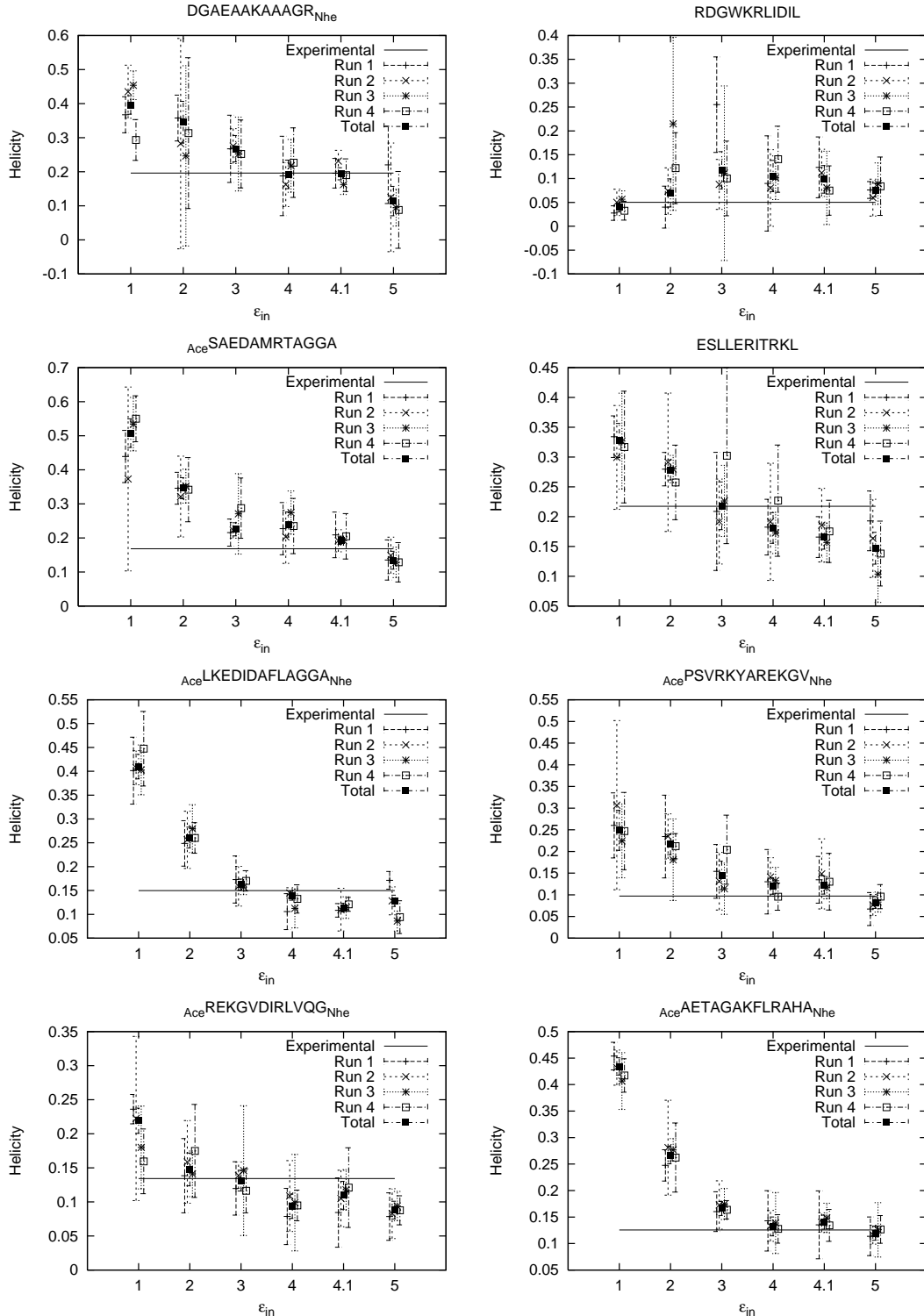


**Figure 4.6:** Helicity versus  $\epsilon_{in}$  for each peptide in Table 3.1 at values of  $\epsilon_{in} \in \{1, 2, 3, 4, 4.1, 5\}$ . The experimentally measured helicity for each peptide is plotted as a horizontal line.

## Helical backbone angles

As a second example, we consider the boundaries of the helical  $(\phi, \psi)$  region which define a “helical” backbone conformation in Equation 3.8. Although a general region may be defined based on Ramachandran plots to be approximately  $\phi \in \{\phi_{\min}, \phi_{\max}\} = \{-87, -27\}$  and  $\psi \in \{\psi_{\min}, \psi_{\max}\} = \{-77, -17\}$ , the exact region measured by CD at ellipticity  $\theta_{225}$  is somewhat ambiguous. We may view the boundaries of this region to be parameters of the statistical mechanical model and estimate them by Bayesian inference as above. In this case evaluation of the posterior at a range of  $\phi_{\max}^H, \phi_{\min}^H, \psi_{\max}^H, \psi_{\min}^H$  may be done more easily than for  $\epsilon_{in}$  since these are parameters of the statistical mechanical model for helicity but not of the forcefield which determines the simulation ensemble; thus we need simply re-analyze the trajectories rather than re-simulate for each value.

For simplicity, we again discretize and construct a four dimensional grid for possible values of  $(\phi_{\max}^H, \phi_{\min}^H, \psi_{\max}^H, \psi_{\min}^H)$ . The marginal posterior distributions obtained for  $(\phi_{\min}^H, \phi_{\max}^H)$  under a uniform prior are shown in Figure 4.7a, and for  $(\psi_{\min}^H, \psi_{\max}^H)$  in Figure 4.7b. Peaks representing high probability values of  $(\phi_{\min}, \phi_{\max})$  are seen at  $(-80, -50)$  and  $(-90, -40)$ , with a ridge for  $\phi_{\min}$  between  $-100$  and  $-70$ . The joint distribution for  $(\psi_{\min}, \psi_{\max})$  exhibits a sharp peak at  $(-60, -40)$  and a minor peak at  $(-50, -30)$ . The ranges of dihedral angles with the largest peaks for both  $\phi$  and  $\psi$  contain the values for an ideal helix  $(\phi, \psi) = (-57, -47)$ , but the joint mode of  $(\phi_{\min}, \phi_{\max}, \psi_{\min}, \psi_{\max}) = (-90, -40, -60, -40)$  yields a narrower range than that generally accepted for helical angles  $(-57 \pm 30, -47 \pm 30)$ . Ridges are centered near ideal values of  $-57$  for  $\phi$  and  $-47$  for  $\psi$ , further increasing the probability in these

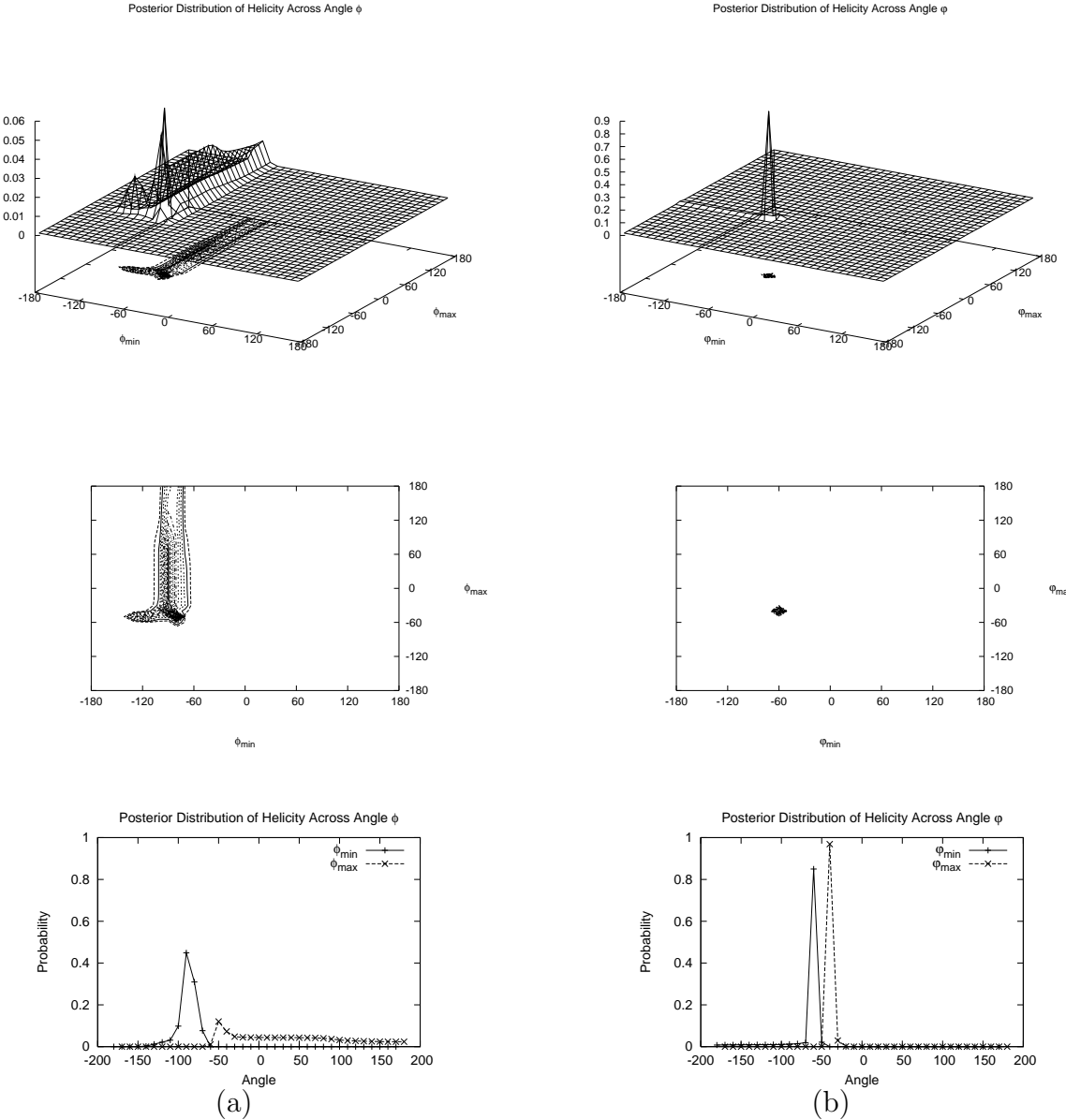


**Figure 4.7:** Marginal posterior distributions of boundaries of the helical angle region (a)  $\phi_{\min}$  and  $\phi_{\max}$ , and (b)  $\psi_{\min}$  and  $\psi_{\max}$ .

regions. The ridge suggests that the precise value of  $\phi_{max}$  is poorly identified, likely due to peptide backbone geometry where for  $\phi$  values below -100 and  $\psi$  values above -40, backbone steric clashes prevent configurations being sampled at all. This experiment only measures the accuracy of helical boundaries for  $\phi$  and  $\psi$  angles for this specific AMBER potential used with the default parameters listed in Table 3.2. For a more accurate boundary calculation, a more extensive experiment with helical and non-helical peptides would be required.

#### 4.1.4 Cross Validation

In order to run further simulations, we must choose a particular value for the internal dielectric parameter; a natural choice is the mode of the posterior distribution at  $\epsilon_{in} = 4.1$ . This value gives the best agreement between the experimental helicities and the simulated helicities for our observed peptides.

However we wish to know how sensitive this result is to the particular set of peptides chosen, and thus how well we can expect this choice to *generalize* to accurately simulate the helicity of new peptides outside our data set. Simply taking the accuracy of  $\epsilon_{in} = 4.1$  in predicting these eight peptides will tend to overestimate this accuracy, because this value has been optimized to perform well on those peptides. Nevertheless, we can estimate the future (out-of-sample) predictive accuracy from the current set of peptides using the statistical method of cross-validation. We measure predictive accuracy via the mean squared error (MSE) between the predicted and experimentally measured helicity values.

Cross-validation proceeds by removing one peptide (say the  $i^{th}$  one) from the

dataset, and using the other seven to estimate/optimize the parameter  $\epsilon_{in}$ . Denote the resulting parameter value by  $\hat{\epsilon}_{[-i]}$ . We then use this value to simulate the removed peptide and predict its helicity, calculating the squared error between predicted and experimental values. This process is then repeated to obtain similar predicted accuracies for each of the peptides in turn, always using the parameter value optimized over the other seven peptides, to calculate the overall estimated predictive accuracy:

$$\text{MSE}_{\text{cv}} = \frac{1}{p} \sum_{i=1}^p (h_i^{\text{exp}} - \hat{h}_i^{\hat{\epsilon}_{[-i]}})^2.$$

This procedure has well established properties as an unbiased estimator of the out-of-sample predictive accuracy of our parameter adaptation method Hastie et al. [2001]. Because the vast majority of our computational work is done upfront in running the simulations of each peptide at each value of  $\epsilon_{in}$ , the expense of calculating the cross-validated prediction accuracy is negligible.

Table 4.2 shows the MSE for each value of  $\epsilon_{in}$  and the cross-validated MSE; in this case the cross-validated MSE is equal to the MSE for  $\epsilon_{in} = 4.1$  since each  $\hat{\epsilon}_{[-i]}$  was equal to 4.1. Although this method is computationally cheap because we do not

$\epsilon_{in}$	1	2	3	4	4.1	5	CV
MSE	0.0405	0.0120	0.0025	0.0016	0.0013	0.0025	0.0013

**Table 4.2:** Mean-squared error (MSE) for each value of  $\epsilon_{in}$ , along with estimated out-of-sample prediction accuracy given by MSE obtained from cross-validation.

have to run new simulations, the ideal predictor of the accuracy of the parameter on new peptides would be to run new peptides with the predicted parameter value. Even though we are removing a peptide to run cross validation, the parameter 4.1 was chosen after starting with values of  $\epsilon_{in}$  from 1 to 5 with these 8 peptides. Thus

the very choice of the new parameter value was biased by the set of 8 peptides, and to make a completely unbiased estimate of the accuracy of the parameter, new peptides should be simulated.

## 4.2 Conclusions

This chapter is presented through a Bayesian lens: we adapt parameters, both of the molecular dynamics themselves,  $\epsilon_{in}$ , and of the tool we are using to measure the simulation data,  $(\phi_{lo}, \phi_{hi}, \psi_{lo}, \psi_{hi})$ . We start with a non-informative prior distribution and use simulation data to generate our posterior distributions on the parameters of interest; we are demonstrating a method of fine-tuning or completely altering parameters that have stark effects on simulation output. To generate molecular dynamics simulations that can not only be compared with experimental output but can also be used to predict experimental output, the parameters that govern these dynamics must each be studied with a fine tooth comb so that slight errors in parameter values do not cause chronic flaws.

# Chapter 5

## Preserving the Boltzmann Ensemble in Replica-Exchange Molecular Dynamics

REMD was derived from parallel tempering, a Monte Carlo algorithm which has certain desirable characteristics; however, REMD does not necessarily inherit these characteristics. Chief among these is the ability to generate configurations according to the Boltzmann ensemble, a key condition for computing experimental observables from simulation. In this chapter we consider convergence behavior of the REMD algorithm as commonly implemented in biomolecular simulation, focusing on certain theoretical shortcomings and their practical implications. In particular, we emphasize the properties of measure-invariance and ergodicity, show that isothermal dynamics algorithms commonly used do not exhibit these properties, and that as a result REMD using these standard integrators also fails to exhibit these properties.

We review necessary and sufficient conditions for dynamical systems and their integrators to be measure-preserving and ergodic. We then examine several commonly-used and proposed techniques for the isothermal dynamics required by REMD and show that all fail to satisfy these conditions. By proving rigorously these failures,

we resolve ambiguity in the literature stemming from purely empirical studies and assumptions. We also show that combining these dynamics via replica-exchange does not correct this problem. In some cases these failures are known, while in others our results are new; however, in all cases the impact on the theoretical properties and practical performance of REMD does not appear to have been appreciated. We conclude by showing that these failures can be addressed by the addition of stochastic hybrid Monte Carlo corrections, and demonstrate the significant practical differences obtained on some simple Hamiltonian systems.

## 5.1 Ergodicity and Invariance in Molecular Simulation

An important application of molecular simulation techniques in practice, as well as a key step in evaluating and improving forcefields (see Chapter 4), is the calculation of experimental observables via ensemble averages:

$$\langle f \rangle = \int_{\mathcal{X}} f(\mathbf{q}, \mathbf{p}) \pi(\mathbf{q}, \mathbf{p}) d\mathbf{q} d\mathbf{p}$$

A critical requirement of a (deterministic or stochastic) simulated molecular dynamical system is therefore that it be *ergodic*, namely that limiting long-run time averages equal averages over the configurational ensemble:

$$\lim_{t \rightarrow \infty} \frac{1}{t} \int_0^t f(\mathbf{q}(s), \mathbf{p}(s)) ds = \langle f \rangle,$$

or in practice, we require for the time-discretized dynamics given by the iterated mapping  $S$  that

$$\lim_{n \rightarrow \infty} \frac{1}{n} \sum_{k=1}^n f(S^k(\mathbf{q}_0, \mathbf{p}_0)) = \langle f \rangle, \quad (5.1)$$

for all integrable functions  $f$ . If (5.1) holds, time-averaged quantities computed from sufficiently long simulation trajectories can be used to compute thermodynamic properties of the system such as equilibrium constants and free energies, transition rates, and other experimental observables.

Ergodicity is often taken as an *assumption* in molecular simulation, but we will show that (5.1) does not hold for many simulation techniques in common use. It is important to note that although the ensemble (2.13) is completely determined by the potential (forcefield)  $U$ , a dynamical simulation which fails to satisfy (5.1) will not properly generate this ensemble and therefore not accurately reflect the forcefield.

It is well known that dynamical systems exhibit such ergodic limiting behavior if and only if they are both *invariant* (or *measure-preserving*), and *irreducible*, with respect to  $\pi$  [Billingsley, 1995, Choe, 2005]. Ergodicity and measure-invariance of a measure  $\pi$  are as defined in Chapter 2. Informally, invariance means that the dynamics has  $\pi$  as an equilibrium, and ergodicity guarantees the equilibrium is unique and the dynamics will converge to  $\pi$  from any starting point.

*Ergodicity and invariance of replica-exchange* Write the discretized dynamics of MD at fixed temperature  $T$  as a mapping on phase space  $S_T : \mathcal{X} \rightarrow \mathcal{X}$  taking positions and momenta at time  $t$  to new positions and momenta at time  $t + \Delta t$ . Then REMD can be written as a mapping  $S^* : \mathcal{X}^* \rightarrow \mathcal{X}^*$  formed as a composition  $S^* = S_1^r \circ S_2$  where  $S_1$  is a block-diagonal mapping given by the direct sum  $S_1 = \bigoplus_{i=1}^k S_{T_i}$ , and  $S_2$

is the stochastic temperature swap given by the transition kernel

$$S_2(\mathbf{x}, A) = \frac{1}{k^2} \sum_{i,j} \mathbf{1}_A((i,j)\mathbf{x}) \rho(\mathbf{x}, (i,j)\mathbf{x}) + \mathbf{1}_A(\mathbf{x}) \left[ 1 - \frac{1}{k^2} \sum_{i,j} \rho(\mathbf{x}, (i,j)\mathbf{x}) \right]$$

where  $\mathbf{x} = ((\mathbf{q}_{T_1}, \mathbf{p}_{T_1}), \dots, (\mathbf{q}_{T_n}, \mathbf{p}_{T_n}))$  and we use the transposition notation  $(i,j)\mathbf{x}$  to denote the state after swapping configurations between temperatures  $i$  and  $j$ , which is accepted or rejected according to the Metropolis criteria [Metropolis et al., 1953]:

$$\rho(\mathbf{x}, (i,j)\mathbf{x}) = \min \left\{ 1, \frac{\pi_{T_i}(\mathbf{x}_j) \pi_{T_j}(\mathbf{x}_i)}{\pi_{T_i}(\mathbf{x}_i) \pi_{T_j}(\mathbf{x}_j)} \right\}.$$

By construction,  $\rho$  ensures the swapping step  $S_2$  is reversible with respect to the joint Boltzmann distribution

$$\pi(\mathbf{x}) = \prod_{i=1}^k \pi_{T_i}(\mathbf{q}_i, \mathbf{p}_i)$$

and thus leaves the product measure  $\pi$  invariant. It follows that the replica-exchange dynamics  $S^*$  leave  $\pi(\mathbf{x})$  invariant on the product space  $\mathcal{X}^k$  if and only if the isothermal dynamics  $S_{T_j}$  leave  $\pi_{T_j}(\mathbf{q}_j, \mathbf{p}_j)$  invariant for each temperature  $T_j$ . In Section 5.3 we show that one commonly used simulation method fails to do so.

Because (2.13) is strictly positive for all  $T > 0$ ,  $S^*$  is ergodic if any of the individual  $S_{T_i}$ 's are ergodic. On the other hand, if the  $S_{T_i}$  are reducible for all  $i = 1, \dots, k$ , the combined dynamics may or may not be ergodic due to swapping: the ergodicity of  $S^*$  must be verified. In Section 5.3 we show that two common isothermal dynamics simulation methods, Nosé-Hoover and Nosé-Poincaré, fail to be ergodic and that REMD using these methods also fails to be ergodic. In other words,

if the underlying constant-temperature dynamics associated with individual replicas are non-ergodic, swapping them by replica-exchange is unlikely to fix the problem. In Section 5.4 we provide a simple fix for this problem.

If  $S^*$  is  $\pi$ -invariant and ergodic, then by (5.1) the individual temperature trajectories  $(\mathbf{q}_i^{(t)}, \mathbf{p}_i^{(t)})$  of an REMD simulation converge to ensemble averages under the constant temperature (canonical) Boltzmann ensemble for each  $T_i$ , and in particular for  $T_0$ , the temperature of interest.

## 5.2 Hamiltonian Dynamics and Symplectic Integrators

Most of the dynamical systems used in MD and REMD simulation which we consider satisfy (1) for the Boltzmann probability measure  $\pi_H(\mathbf{q}, \mathbf{p}) = \delta(\mathcal{H}(\mathbf{q}, \mathbf{p}) - \mathcal{H}(\mathbf{q}_0, \mathbf{p}_0))$ , by virtue of forming *Hamiltonian systems* (Section 2.2). Newtonian dynamics (2.1) is a Hamiltonian system with Hamiltonian  $\mathcal{H}(\mathbf{x}) = U(\mathbf{q}) + \sum_i \frac{\|\mathbf{p}_i\|^2}{2m_i}$ , and the corresponding Boltzmann distribution  $\pi$  is the *microcanonical* (or constant energy) ensemble. Any Hamiltonian system conserves its associated Hamiltonian  $\mathcal{H}$ :

$$\frac{d\mathcal{H}}{dt} = \frac{\partial\mathcal{H}}{\partial\mathbf{q}} \frac{d\mathbf{q}}{dt} + \frac{\partial\mathcal{H}}{\partial\mathbf{p}} \frac{d\mathbf{p}}{dt} = \frac{\partial\mathcal{H}}{\partial\mathbf{q}} \frac{\partial\mathcal{H}}{\partial\mathbf{p}} + \frac{\partial\mathcal{H}}{\partial\mathbf{p}} \left( -\frac{\partial\mathcal{H}}{\partial\mathbf{q}} \right) = 0.$$

and therefore

$$\begin{aligned} \int_{\mathcal{X}} f(\mathbf{q}, \mathbf{p}) d\pi &= \int_{\mathcal{X}} f(\mathbf{q}, \mathbf{p}) \frac{1}{Z} e^{-\mathcal{H}(\mathbf{q}, \mathbf{p})/(k_B T)} d\mathbf{q} d\mathbf{p} \\ &= \int_{\mathcal{X}} f(S(\mathbf{q}, \mathbf{p})) \frac{1}{Z} e^{-\mathcal{H}(S(\mathbf{q}, \mathbf{p}))/(k_B T)} |J_s| d\mathbf{q} d\mathbf{p} \\ &= \int_{\mathcal{X}} f(S(\mathbf{q}, \mathbf{p})) \frac{1}{Z} e^{-\mathcal{H}(\mathbf{q}, \mathbf{p})/(k_B T)} |J_s| d\mathbf{q} d\mathbf{p} = \int_{\mathcal{X}} f(S(\mathbf{q}, \mathbf{p})) d\pi \end{aligned}$$

Therefore to be  $\pi$ -invariant,  $S$  must have Jacobian equal to one. Liouville's theorem states that this holds for any Hamiltonian dynamics - namely that Hamiltonian dynamics are volume- (or *Lebesgue measure-*) preserving [Arnold, 1989]. Note that often  $S$  may not be ergodic on  $\pi_H$ , and so from Section 5.1 still does not generate the microcanonical ensemble, i.e. does not satisfy (5.1).

### 5.2.1 Symplectic integrators

A key point is that the properties of Section 5.1 - invariance and ergodicity - must hold not only for the theoretical continuous time dynamical system, but also for the time-discretized dynamics obtained in practice by application of numerical integration on a computer. In practice, the numerical integrators chosen for MD, such as the leap-frog integrator (2.9), are chosen to be *symplectic* [Channell and Scovel, 1990], a property that implies phase-space volume preserving. For any  $\Delta t > 0$  however, they only approximately conserve the Hamiltonian  $\mathcal{H}$ . (The hybrid Monte Carlo modifications given in Section 5.4 corrects for this.)

It is easily checked that the leap-frog integrator (2.9) is volume preserving, by writing:

$$S_a : (\mathbf{q}, \mathbf{p}) \mapsto (\mathbf{q}', \mathbf{p}') = (\mathbf{q}, \mathbf{p} + F(\mathbf{q})\Delta t),$$

$$S_b : (\mathbf{q}', \mathbf{p}') \mapsto (\mathbf{q}'', \mathbf{p}'') = (\mathbf{q}' + \frac{\mathbf{p}'}{m}\Delta t, \mathbf{p}'),$$

with

$$J_{S_a} = \begin{vmatrix} 1 & 0 \\ F'(\mathbf{q})\Delta t & 1 \end{vmatrix} = 1 \quad J_{S_b} = \begin{vmatrix} 1 & \frac{1}{m}\Delta t \\ 0 & 1 \end{vmatrix} = 1.$$

However, replica-exchange dynamics relies on *isothermal* (constant temperature) dynamics to generate the canonical ensemble, rather than the microcanonical (constant energy) ensemble generated by Newtonian dynamics. Isothermal dynamics requires modified Hamiltonians and specialized integrators. We will see that not all of the numerical integrators used in such dynamics are in fact volume-preserving; while in other cases the underlying dynamics fail to be ergodic.

### 5.3 Isothermal Molecular Dynamics

Replica-exchange molecular dynamics relies on the use of *isothermal* (constant temperature) or *canonical ensemble* molecular dynamics simulations at each level of the temperature ladder. In the original formulation of REMD, Sugita and Okamoto [1999] utilized the Berendsen heat-bath algorithm [Berendsen et al., 1984] to achieve isothermal dynamics, and this has been standard practice in REMD simulations [Daura et al., 1998, 1999, Garcia and Sanbonmatsu, 2002, Smith et al., 2002, Nymeyer and Garcia, 2003]. More recently, the Nosé-Hoover thermostat algorithm has also been applied for this purpose [Nymeyer and Garcia, 2003]. We briefly review these and related methods for performing deterministic isothermal dynamics. Our focus is on viewing these algorithms with respect to the invariance and irreducibility properties defined in Section 2.4; as we will see, *all* of these algorithms fail to yield an ergodic replica-exchange dynamics.

### 5.3.1 Velocity rescaling and the Berendsen heat-bath

By far the most commonly used algorithm for constant temperature MD is the Berendsen heat bath [Berendsen et al., 1984], due to its ease of implementation and availability in standard software packages [Pearlman et al., 1995, Phillips et al., 2005, Lindahl et al., 2001]. In this approach, the system is weakly coupled to a heat bath by rescaling the momenta after each step to adjust the temperature, at rate proportional to the difference between current and target temperatures:

$$\frac{dT(t)}{dt} = \frac{1}{\tau}(T - T(t))$$

This amounts to convolving the mapping  $R : (\mathbf{q}, \mathbf{p}) \mapsto (\mathbf{q}, \lambda\mathbf{p})$  with the ( $\Delta t$ -discretized) dynamics, where

$$\lambda^2 = 1 + \frac{\Delta t}{\tau} \left( \frac{T}{\hat{T}(t)} - 1 \right) \quad \hat{T}(t) = \left( \frac{3p}{2} k_B T \right)^{-1} \sum_{i=1}^p \frac{\|\mathbf{p}_i\|^2}{2m_i}.$$

However, it is easily seen (and well-known, see e.g. Frenkel and Smit [1996]) that this mapping is not invariant under the canonical distribution:

$$\begin{aligned} \int_{\mathcal{X}} f(\mathbf{q}', \mathbf{p}') d\pi(\mathbf{q}', \mathbf{p}') &= \int_{\mathcal{X}} f(\mathbf{q}', \mathbf{p}') \frac{e^{-\mathcal{H}(\mathbf{q}', \mathbf{p}')/(k_B T)}}{Z} d\mathbf{q}' d\mathbf{p}' \\ &= \int_{\mathcal{X}} f(\mathbf{q}, \lambda\mathbf{p}) \frac{e^{-\mathcal{H}(\mathbf{q}, \lambda\mathbf{p})/(k_B T)}}{Z} \lambda d\mathbf{q} d\mathbf{p} \neq \int_{\mathcal{X}} f(\mathbf{q}, \mathbf{p}) d\pi(\mathbf{q}, \mathbf{p}). \end{aligned}$$

In addition, the resulting dynamics are clearly not time-reversible. Thus the Berendsen heat bath approach to isothermal MD does not generate canonical ensemble (although Morishita [2000] argues that it approximately preserves certain properties). Since we saw in Section 5.1 that REMD is  $\pi$ -invariant if and only if each replica is

$\pi_T$ -invariant, REMD fails to generate the canonical ensemble when implemented via the Berendsen algorithm. Given the extensive use of the Berendsen heat-bath in MD and REMD simulations [Sugita and Okamoto, 1999, Daura et al., 1998, 1999, Garcia and Sanbonmatsu, 2002, Smith et al., 2002, Nymeyer and Garcia, 2003], this is a source of some concern. In Section 5.5, we demonstrate significant failures of the Berendsen-based REMD algorithm on examples.

### 5.3.2 Extended Lagrangian methods

#### Nosé-Hoover thermostat

An alternative method for isothermal dynamics based on an extended Lagrangian was introduced by Nosé [1984], and reformulated by Hoover [1985]. This approach has been used as an alternative to the Berendsen thermostat to generate constant temperature dynamics for REMD [Nymeyer and Garcia, 2003]. Nosé adds an additional coordinate  $s$ , rescaling time to  $dt' = dt/s$ , and introducing the augmented Hamiltonian:

$$\mathcal{H}_{\text{Nosé}} = U(\mathbf{q}) + \sum_i \frac{\|\mathbf{p}_i\|^2}{2m_i s^2} + \frac{p_s^2}{2Q} + gk_B T \ln s, \quad (5.2)$$

where  $s$  is a time-scale variable with conjugate momentum  $p_s$ ,  $Q$  is a parameter of dimension energy·time<sup>2</sup> which behaves like a mass for the motion of  $s$ , and  $g$  is the

degrees of freedom plus one. The equations of motion then become

$$\begin{aligned}\frac{d\mathbf{q}_i}{dt'} &= \frac{\partial \mathcal{H}}{\partial \mathbf{p}_i} = \frac{\mathbf{p}_i}{m_i s^2}, \\ \frac{d\mathbf{p}_i}{dt'} &= -\frac{\partial \mathcal{H}}{\partial \mathbf{q}_i} = -\frac{\partial}{\partial \mathbf{q}_i} U(\mathbf{q}), \\ \frac{ds}{dt'} &= \frac{\partial \mathcal{H}}{\partial p_s} = \frac{p_s}{Q}, \\ \frac{dp_s}{dt'} &= -\frac{\partial \mathcal{H}}{\partial s} = \left( \sum_i \frac{\|\mathbf{p}_i\|^2}{m_i s^2} - gkT \right) / s.\end{aligned}$$

As with all Hamiltonian systems, these dynamics preserve the Hamiltonian  $\mathcal{H}_{\text{Nosé}}$ :

$$\begin{aligned}\frac{d\mathcal{H}}{dt'} &= \frac{\partial \mathcal{H}}{\partial p_s} \frac{dp_s}{dt'} + \frac{\partial \mathcal{H}}{\partial s} \frac{ds}{dt'} + \sum_i \left( \frac{\partial \mathcal{H}}{\partial \mathbf{q}_i} \frac{d\mathbf{q}_i}{dt'} + \frac{\partial \mathcal{H}}{\partial \mathbf{p}_i} \frac{d\mathbf{p}_i}{dt'} \right) \\ &= \frac{\partial \mathcal{H}}{\partial p_s} \left( -\frac{\partial \mathcal{H}}{\partial s} \right) + \frac{\partial \mathcal{H}}{\partial s} \left( \frac{\partial \mathcal{H}}{\partial p_s} \right) + \sum_i \left( \frac{\partial \mathcal{H}}{\partial \mathbf{q}_i} \left( \frac{\partial \mathcal{H}}{\partial \mathbf{p}_i} \right) + \frac{\partial \mathcal{H}}{\partial \mathbf{p}_i} \left( -\frac{\partial \mathcal{H}}{\partial \mathbf{q}_i} \right) \right) \\ &= 0\end{aligned}$$

and Nosé showed that the microcanonical ensemble in this augmented phase-space yields the canonical ensemble for  $(\mathbf{q}, \mathbf{p}/s)$ , independent of choice of  $Q$  and the initial value of  $\mathcal{H}_{\text{Nosé}}$ . However, because time is scaled by  $s$  which changes as the differential equation evolves, the system is not convenient for computation. Hoover [1985] remedied this problem by modifying the Nosé dynamics to create a non-Hamiltonian dynamics. The system simplifies to three equations:

$$\dot{\mathbf{q}}_i = \frac{\mathbf{p}_i}{m_i}, \quad \dot{\mathbf{p}}_i = -\frac{\partial}{\partial \mathbf{q}_i} U(\mathbf{q}) - \zeta \mathbf{p}_i, \quad \dot{\zeta} = \frac{1}{Q} \left( \sum_i \frac{\mathbf{p}_i}{m_i} - gkT \right), \quad (5.3)$$

where  $g = N_f$  is degrees of freedom of the real system, compared to  $g = N_f + 1$  in the Nosé system. Although the Nosé-Hoover system is no longer Hamiltonian, it

conserves the *extended energy*:

$$E_{ext}(\mathbf{q}, \mathbf{p}, \zeta) = U(\mathbf{q}) + \sum_i \frac{\|\mathbf{p}_i\|^2}{2m_i} + \frac{Q\zeta^2}{2}, \quad (5.4)$$

and Hoover [Hoover, 1985] argues that it also conserves the associated Boltzmann distribution

$$\pi(\mathbf{q}, \mathbf{p}, \zeta) = Z^{-1} e^{-\frac{1}{k_B T} E_{ext}(\mathbf{q}, \mathbf{p}, \zeta)},$$

by use of the conservation of mass or continuity equation  $\frac{d\pi}{dt} = \frac{\partial\pi}{\partial t} + \nabla \cdot (\pi \mathbf{u}) = 0$  where  $\mathbf{u} = [d\mathbf{q}/dt, d\mathbf{p}/dt, d\zeta/dt]$  is the “fluid” velocity. However, although the Nosé-Hoover dynamics conserve the density  $\pi$ , they do not preserve the underlying measure (phase-space volume) and so are not symplectic. To see this consider  $\lim_{t \rightarrow 0} (|V(t)| - |V(0)|)/t$  which goes to zero for Hamiltonian dynamics by Liouville’s theorem [Arnold, 1989], but not for Nosé-Hoover dynamics. Let  $\mathbf{x} = (\mathbf{q}, \mathbf{p})$  and define  $g^t(\mathbf{x}) = (\mathbf{q}, \mathbf{p}) + (\dot{\mathbf{q}}, \dot{\mathbf{p}})t + O(t^2)$ . Then:

$$\begin{aligned} |V(t)| &= \int_{V(0)} \det \left( \frac{\partial g^t(\mathbf{x})}{\partial \mathbf{x}} \right) d\mathbf{q} d\mathbf{p} = \int_{V(0)} [1 - \zeta t + O(t^2)] d\mathbf{q} d\mathbf{p} \\ &= V(0)(1 - \zeta t) + O(t^2). \end{aligned}$$

We can then see that  $\lim_{t \rightarrow 0} (|V(t)| - |V(0)|)/t = -\zeta V(0) \neq 0$ , so the volume of the phase-space is not preserved, as recognized by Hoover [1985]. But then the Nosé-Hoover dynamics are not  $\pi$ -invariant since

$$\begin{aligned} \int_{\mathcal{X}} f(\mathbf{x}') d\pi(\mathbf{x}') &= \int_{\mathcal{X}} f(\mathbf{q}', \mathbf{p}', \zeta') \frac{e^{-[U(\mathbf{q}') + \sum_i \frac{\|\mathbf{p}'_i\|^2}{2m_i} + \frac{Q\zeta'^2}{2}]/(k_B T)}}{ZZ_\zeta} d\mathbf{q}' d\mathbf{p}' d\zeta' \\ &= \int_{\mathcal{X}} f(\mathbf{q}, \mathbf{p}, \zeta) \frac{e^{-[U(\mathbf{q}) + \sum_i (\frac{\|\mathbf{p}_i\|^2}{2m_i}) + \frac{Q\zeta^2}{2}]/(k_B T)}}{ZZ_\zeta} |J_T| d\mathbf{q} d\mathbf{p} d\zeta \\ &\neq \int_{\mathcal{X}} f(\mathbf{x}) d\pi(\mathbf{x}). \end{aligned}$$

Specialized integrators have been developed for Nose-Hoover dynamics simulation. The method of Winkler et al. [1995] addresses shortcomings of others and is described in Section 5.3.3, but is also not symplectic. Of greater concern is that the underlying continuous time Nosé-Hoover dynamics themselves fail to be irreducible, as observed empirically by Hoover [1985] and noted by many others [Martyna et al., 1992, Frenkel and Smit, 1996, Morishita, 2000]. As Nosé-Hoover has been used in REMD simulation [Nymeyer and Garcia, 2003], we show in Section 5.3.5 that REMD using Nose-Hoover dynamics also fails to be ergodic; i.e., the stochastic swapping of introduced by replica-exchange is not sufficient to achieve irreducibility.

### 5.3.3 Nosé-Hoover Integrators

Winkler et al. [1995] modified a time-reversible integrator developed by Toxvaerd [1993] for Nosé-Hoover dynamics:

$$\begin{aligned} \mathbf{q}_i(t + \Delta t) &= \mathbf{q}_i(t) + \frac{\mathbf{p}_i(t)}{m_i} \Delta t + \left[ \frac{\partial}{\partial \mathbf{q}_i} U(\mathbf{q}(t)) - \zeta(t) \mathbf{p}_i(t) \right] \frac{\Delta t^2}{2m_i}, \\ \mathbf{p}_i \left( t + \frac{1}{2} \Delta t \right) &= \mathbf{p}_i(t) + \left[ \frac{\partial}{\partial \mathbf{q}_i} U(\mathbf{q}(t)) - \zeta(t) \mathbf{p}_i(t) \right] \frac{\Delta t}{2}, \\ \zeta(t + \Delta t) &= \zeta(t) + \left[ \sum_{i=1}^{N_f} m_i \|\mathbf{p}_i\|^2 \left( t + \frac{1}{2} \Delta t \right) - gkT \right] \frac{\Delta t}{Q}, \\ \mathbf{p}_i(t + \Delta t) &= \left( \mathbf{p}_i \left( t + \frac{1}{2} \Delta t \right) + \left[ \frac{\partial}{\partial \mathbf{q}_i} U(\mathbf{q}(t + \Delta t)) \right] \frac{\Delta t}{2} \right) / \left( 1 + \zeta(t + \Delta t) \frac{\Delta t}{2} \right). \end{aligned}$$

However, considering the phase space over the variables  $(\mathbf{q}, \mathbf{p}, \zeta)$ , we can see that the

mapping is not volume-preserving or symplectic. Define

$$R_1 : (\mathbf{q}, \mathbf{p}, \zeta) \mapsto (\mathbf{q}', \mathbf{p}', \zeta') = \left( \mathbf{q} + \frac{\mathbf{p}}{m} \Delta t + (F(\mathbf{q}) - \zeta \mathbf{p}) \frac{\Delta t}{2m}, \mathbf{p} + (F(\mathbf{q}) - \zeta \mathbf{p}) \frac{\Delta t}{2}, \zeta \right),$$

$$R_2 : (\mathbf{q}', \mathbf{p}', \zeta') \mapsto (\mathbf{q}'', \mathbf{p}'', \zeta'') = \left( \mathbf{q}', \mathbf{p}', \zeta + \left[ \sum m_i (\mathbf{p}')^2 - gkT \right] \frac{\Delta t}{2} \right),$$

$$R_3 : (\mathbf{q}'', \mathbf{p}'', \zeta'') \mapsto (\mathbf{q}''', \mathbf{p}''', \zeta''') = \left( \mathbf{q}'', \left( \mathbf{p}'' + F(\mathbf{q}'') \frac{\Delta t}{2} \right) / \left( 1 + \zeta'' \frac{\Delta t}{2} \right), \zeta''' \right).$$

Then the Jacobian of the composition map  $S(\mathbf{q}, \mathbf{p}, \zeta) = R_3 \circ R_2 \circ R_1$  is

$$\begin{aligned} J_S &= J_{R_3} J_{R_2} J_{R_1} \\ &= \begin{vmatrix} 1 & 0 & 0 \\ \frac{F'(\mathbf{q})}{2+\zeta\Delta t} & \frac{2}{2+\zeta\Delta t} & \frac{-2\mathbf{p}-F'(\mathbf{q})\Delta t}{(2+\zeta\Delta t)^2} \frac{\Delta t}{2} \\ 0 & 0 & 1 \end{vmatrix} \cdot \begin{vmatrix} 1 & 0 & 0 \\ 0 & 1 & 0 \\ 0 & \frac{m\Delta t}{Q} f(\mathbf{p}) & 1 \end{vmatrix} \\ &\cdot \begin{vmatrix} 1 + F'(\mathbf{q}) \frac{\Delta t^2}{2m} & \frac{\Delta t}{m} - \zeta \frac{\Delta t^2}{2m} & -\frac{\mathbf{p}\Delta t}{2m} \\ F'(\mathbf{q}) \frac{\Delta t}{2} & 1 - \zeta \frac{\Delta t}{2}, -\frac{\mathbf{p}\Delta t}{2} & 1 \\ 0 & 0 & 1 \end{vmatrix} = \frac{2 - \zeta \Delta t}{2 + \zeta \Delta t}, \end{aligned}$$

so  $J_S < 1$  for  $\Delta t > 0$ . Winkler et al. [1995] also introduced an alternative method, but it is not phase-space volume preserving for systems with many degrees of freedom such as polypeptides.

### Nosé-Poincaré Hamiltonian

To circumvent the difficulties which arise from the non-Hamiltonian nature of the Nosé-Hoover dynamics, Bond et al. [1999] constructed a Poincaré time transformation of the original Nosé system. The Poincaré transformation of the Nosé Hamiltonian (5.2) yields a new Hamiltonian

$$\tilde{\mathcal{H}} = s \Delta \mathcal{H} = s \left( U(\mathbf{q}) + \sum_i \frac{\|\mathbf{p}_i\|^2}{2m_i s^2} + \frac{p_s^2}{2Q} + gkT \ln s - \mathcal{H}_0 \right), \quad (5.5)$$

where  $\Delta\mathcal{H} = \mathcal{H}_{\text{Nosé}} - \mathcal{H}_0$  and  $\mathcal{H}_0$  is the initial value of  $\mathcal{H}$  at time  $t = 0$ . The resulting Hamiltonian system is then

$$\begin{aligned}\frac{d\mathbf{q}_i}{dt} &= \frac{\partial \tilde{\mathcal{H}}}{\partial \mathbf{p}_i} = \frac{\mathbf{p}_i}{m_i s}, \\ \frac{d\mathbf{p}_i}{dt} &= -\frac{\partial \tilde{\mathcal{H}}}{\partial \mathbf{q}_i} = -s \frac{\partial}{\partial \mathbf{q}_i} U(\mathbf{q}), \\ \frac{ds}{dt} &= \frac{\partial \tilde{\mathcal{H}}}{\partial p_s} = \frac{s p_s}{Q}, \\ \frac{dp_s}{dt} &= -\frac{\partial \tilde{\mathcal{H}}}{\partial s} = \sum_i \frac{\|\mathbf{p}_i\|^2}{m_i s^2} - gkT + \Delta\mathcal{H}(\mathbf{q}, \mathbf{p}, s, p_s),\end{aligned}$$

and  $\mathcal{H}_0$  is chosen so that initially  $\Delta\mathcal{H} = 0$ . Since this is a Hamiltonian system, it conserves the Hamiltonian (5.5) and by Liouville's theorem is volume-preserving. Bond et al. [1999] show that if the Nosé-Poincaré dynamics are ergodic, they also generate the correct marginal Boltzmann distribution of  $(\mathbf{q}, \mathbf{p})$  (2.13). Nosé [2001] gives an explicit, time-reversible, symplectic integrator for the Nosé-Poincaré dynamics, which is used in Section 5.5 and described in the next section.

### 5.3.4 Nosé Poincaré Integrators

Nosé [2001] gives an explicit, time-reversible, symplectic integrator for the Nosé-Poincaré dynamics:

$$\begin{aligned}
s_i \left( t + \frac{1}{2} \Delta t \right) &= s_i(t) \left( 1 + \frac{p_s(t)}{2Q} \frac{\Delta t}{2} \right)^2, \\
p_s^* &= \frac{p_s(t)}{1 + \frac{p_s(t)}{2Q} \frac{\Delta t}{2}}, \\
\mathbf{p}_i \left( t + \frac{\Delta t}{2} \right) &= \mathbf{p}_i(t) - s \left( t + \frac{\Delta t}{2} \right) \frac{\partial}{\partial \mathbf{q}_i} U(\mathbf{q}(t)) \frac{\Delta t}{2}, \\
\mathbf{q}_i(t + \Delta t) &= \mathbf{q}_i(t) + \frac{\mathbf{p}_i \left( t + \frac{\Delta t}{2} \right)}{m_i s \left( t + \frac{\Delta t}{2} \right)} \Delta t, \\
\mathbf{p}_i(t + \Delta t) &= \mathbf{p}_i \left( t + \frac{\Delta t}{2} \right) - s \left( t + \frac{\Delta t}{2} \right) \frac{\partial}{\partial \mathbf{q}_i} U(\mathbf{q}(t + \Delta t)) \frac{\Delta t}{2}, \\
p_s^{**} &= p_s^* + \left[ \sum_i \frac{1}{2m_i} \left( \frac{\mathbf{p}_i(t + \Delta t)}{s \left( t + \frac{\Delta t}{2} \right)} \right)^2 - \frac{1}{2} (U(\mathbf{q}(t)) + U(\mathbf{q}(t + \Delta t))) \right. \\
&\quad \left. - gkT \ln s \left( t + \frac{\Delta t}{2} \right) + H_0 - gkT \right] \Delta t, \\
s(t + \Delta t) &= s \left( t + \frac{\Delta t}{2} \right) \left( 1 + \frac{p_s^{**}}{2Q} \frac{\Delta t}{2} \right)^2, \\
p_s(t + \Delta t) &= \frac{p_s^{**}}{1 + \frac{p_s(t)}{2Q} \frac{\Delta t}{2}}.
\end{aligned}$$

We can see that this integrator preserves phase-space volume by writing the mappings:

$$R_1 : (\mathbf{q}, \mathbf{p}, s, p_s) \mapsto \left( \mathbf{q}, \mathbf{p}, s \left( 1 + \frac{p_s}{2Q} \frac{\Delta t}{2} \right)^2, \frac{p_s}{1 + \frac{p_s}{2Q} \frac{\Delta t}{2}} \right),$$

$$R_2 : (\mathbf{q}, \mathbf{p}, s, p_s) \mapsto \left( \mathbf{q}, \mathbf{p} - sF(\mathbf{q}) \frac{\Delta t}{2}, s, p_s \right),$$

$$R_3 : (\mathbf{q}, \mathbf{p}, s, p_s) \mapsto \left( \mathbf{q} + \frac{\mathbf{p} \Delta t}{ms}, \mathbf{p}, s, p_s \right),$$

$$R_4 : (\mathbf{q}, \mathbf{p}, s, p_s) \mapsto \left( \mathbf{q}, \mathbf{p} - sF(\mathbf{q}) \frac{\Delta t}{2}, s,$$

$$p_s + \left[ \frac{|\mathbf{p}|^2}{2ms^2} - \frac{1}{2}(U(\mathbf{q}) + U(\mathbf{q}')) - gkT \ln s + H_0 - gkT \right] \Delta t \right),$$

and noting that the integration mapping  $J_S$  is a composition  $J_S = J_{R_1} \circ J_{R_4} \circ J_{R_3} \circ J_{R_2} \circ J_{R_1}$ , and verifying that  $|J_{R_1}| = |J_{R_2}| = |J_{R_3}| = |J_{R_4}| = 1$ :

$$|J_S| = |J_{R_1}| \cdot |J_{R_4}| \cdot |J_{R_3}| \cdot |J_{R_2}| \cdot |J_{R_1}|$$

$$\begin{aligned} &= \begin{vmatrix} 1 & 0 & 0 & 0 \\ 0 & 1 & 0 & 0 \\ 0 & 0 & \left(1 + \frac{p_s \Delta t}{4Q}\right)^2 & 2s \left(1 + \frac{p_s \Delta t}{2Q}\right) \frac{\Delta t}{4Q} \\ 0 & 0 & 0 & 1/\left(1 + \frac{p_s \Delta t}{4Q}\right)^2 \end{vmatrix} \cdot \begin{vmatrix} 1 & 0 & 0 & 0 \\ -sF'(\mathbf{q}) \frac{\Delta t}{2} & 1 & -F(\mathbf{q}) \frac{\Delta t}{2} & 0 \\ 0 & 0 & 1 & 0 \\ 0 & 0 & 0 & 1 \end{vmatrix} \\ &\cdot \begin{vmatrix} 1 & \frac{\Delta t}{ms} & -\frac{\mathbf{p} \Delta t}{ms^2} & 0 \\ 0 & 1 & 0 & 0 \\ 0 & 0 & 1 & 0 \\ 0 & 0 & 0 & 1 \end{vmatrix} \cdot \begin{vmatrix} 1 & 0 & 0 & 0 \\ -sF'(\mathbf{q}) \frac{\Delta t}{2} & 1 & -F(\mathbf{q}) \frac{\Delta t}{2} & 0 \\ 0 & 0 & 1 & 0 \\ F(\mathbf{q}) + F(\mathbf{q}^*) & \frac{1}{2ms^2} G(\mathbf{p}) & -\frac{|\mathbf{p}|^2}{ms^3} - \frac{gkT}{s} & 1 \end{vmatrix} \\ &\cdot \begin{vmatrix} 1 & 0 & 0 & 0 \\ 0 & 1 & 0 & 0 \\ 0 & 0 & \left(1 + \frac{p_s \Delta t}{4Q}\right)^2 & 2s \left(1 + \frac{p_s \Delta t}{2Q}\right) \frac{\Delta t}{4Q} \\ 0 & 0 & 0 & 1/\left(1 + \frac{p_s \Delta t}{4Q}\right)^2 \end{vmatrix} = 1. \end{aligned}$$

### 5.3.5 Failure of ergodicity in REMD using isothermal dynamics

We showed in Section 5.3.1 that the Berendsen thermostat fails to preserve the Boltzmann measure, and therefore by definition (Section 5.1) isothermal dynamics simulations using Berendsen, and REMD simulations with Berendsen-controlled temperatures, fail to be ergodic. In this section we demonstrate that REMD simulations using both Nosé-Hoover and Nosé-Poincaré dynamics also fail to be ergodic, due to reducibility in phase space. Significant attention has been paid in the literature to empirical evidence of ergodicity or lack thereof for these methods, including new variants (chains) introduced to 'enhance ergodicity'. Here we show rigorously that these methods fail to be ergodic, removing any ambiguity. The practical impact of these failures are demonstrated on several examples in Section 5.5.

#### REMD with Nosé-Hoover is not ergodic

To show that replica-exchange using Nosé-Hoover dynamics fails to be ergodic, we first demonstrate that a single Nosé-Hoover dynamics fails to be ergodic. This was observed by Hoover [Hoover, 1985] and has since been noted by many others [Martyna et al., 1992, Frenkel and Smit, 1996, Morishita, 2000].

**Lemma 3.** *The Nosé-Hoover differential system (5.3) with unbounded potential energy  $|U(\mathbf{q})|$  is not ergodic under the Boltzmann measure.*

*Proof.* Define the phase-space subsets

$$A = \left\{ (\mathbf{q}, \mathbf{p}, \zeta) : U(\mathbf{q}) + \sum_i \frac{\|\mathbf{p}_i\|^2}{2m_i} < a, \frac{Q\zeta^2}{2} < b \right\} \quad \text{and}$$

$$B = \left\{ (\mathbf{q}, \mathbf{p}, \zeta) : U(\mathbf{q}) + \sum_i \frac{\|\mathbf{p}_i\|^2}{2m_i} > a + b \right\},$$

for some constants  $a, b$ , and note that  $A$  and  $B$  both have positive Boltzmann measure. Then Nosé-Hoover dynamics cannot reach  $A$  from  $B$ , since the mapping  $S_{\text{NH}}$  preserves the extended energy (5.4), and so for any  $(\mathbf{p}, \mathbf{q}, \zeta) \in A$  and  $n \geq 1$  we have

$$E_{ext}(S_{\text{NH}}^{-n}(\mathbf{p}, \mathbf{q}, \zeta)) = U(\mathbf{q}) + \sum_i \frac{\|\mathbf{p}_i\|^2}{2m_i} + \frac{Q\zeta^2}{2} < a + b,$$

and since  $\frac{Q\zeta^2}{2} \geq 0$ , we have  $\pi(B \cap S_{\text{NH}}^{-n}A) = 0$ .  $\square$

We can now show that REMD using Nosé-Hoover dynamics fails to be ergodic, by showing that for any set of initial configurations  $\{(\mathbf{q}_{T_i}^0, \mathbf{p}_{T_i}^0, \zeta_{T_i}^0)\}$ , there exists a set  $B$  with  $\pi_{T_i}(B) > 0$  that no trajectory can reach.

**Theorem 4.** *REMD using Nosé-Hoover dynamics with unbounded potential energy  $|U(\mathbf{q})|$  is not ergodic under the Boltzmann measure.*

*Proof.* Given any set of initial configurations  $\{\mathbf{x}_{T_i}^0 = (\mathbf{q}_{T_i}^0, \mathbf{p}_{T_i}^0, \zeta_{T_i}^0)\}_{i=1}^k$ , let  $a = \max_i \{U(\mathbf{q}_{T_i}^0) + \sum_j \frac{\|\mathbf{p}_{T_i,j}^0\|^2}{2m_j}\}$ , and  $b = \max_i \{Q(\zeta_{T_i}^0)^2/2\}$ . Define sets

$$A = \{\mathbf{x} : E_{ext}(\mathbf{x}) < a + b\} \quad \text{and}$$

$$B = \left\{ \mathbf{x} : U(\mathbf{q}) + \sum_i \frac{\|\mathbf{p}_i\|^2}{2m_i} > a + b \right\}.$$

Then  $\mathbf{x}_{T_i}^0 \in A$  for all  $T_i$ , and by Lemma 3 the Nosé-Hoover mapping  $S_{T_i}$  at any temperature  $T_i$  cannot reach  $B$  from  $A$  since  $\pi_{T_i}(S_{T_i}^{-n}A \cap B) = 0$  for all  $n$ . But the temperature swap  $S_2$  does not change the value of  $E_{ext}$  for any configuration, since  $T_i$  does not appear in (5.4). Now define sets  $A^* = \{\{\mathbf{x}_{T_i}\}_{i=1}^k : E_{ext}(\mathbf{x}_{T_i}) < a + b \forall i\}$  and  $B^* = \{\{\mathbf{x}_{T_i}\}_{i=1}^k : U(\mathbf{q}_{T_i}) + \sum_j \frac{\|\mathbf{p}_{T_i,j}\|^2}{2m_j} > a + b \forall i\}$ . Then  $\{\mathbf{x}_{T_i}^0\} \in A^*$ , and neither the Nosé-Hoover dynamics nor the temperature swap enable any chain to move from  $A$  to  $B$ , so  $\pi(B^* \cap S^{*-n}A^*) = 0$  for all  $n$ .  $\square$

### Nosé-Hoover Chains

As mentioned in Section 5.3.5, the failure of Nosé-Hoover to be ergodic is well known. Martyna et al. [1992] introduced a modification called *Nosé-Hoover chains*, which adds on  $M$  chains so that the conserved quantity becomes

$$\sum_{i=1}^p \frac{\|\mathbf{p}_i\|^2}{2m_i} + U(\mathbf{q}) + \sum_{i=1}^M \frac{Q_i \zeta_i^2}{2}, \quad (5.6)$$

where  $m_i, Q_i \geq 0$  for all  $i$ . However, although the addition of the  $\zeta_i$ 's increases the range of accessible potential energies (adding REMD replicas has a similar effect in this regard), this range remains bounded by the initial values of the  $\zeta_i$ 's and  $\mathbf{p}_i$ 's.

**Corollary 5.** *Nosé-Hoover chains as defined by Martyna et al. [1992] are not ergodic.*

*Proof.* The sum defined by  $\sum_{i=1}^M \frac{Q_i \zeta_i^2}{2}$  is always positive if  $Q_i > 0$  for all  $i$ , so the argument from Lemma 3 holds.  $\square$

Thus for unbounded energy functions  $U$  such as commonly used molecular mechanics forcefields, neither Nosé-Hoover nor Nosé-Hoover chains are truly ergodic,

as one can always find a value of the potential energy that cannot be reached. In addition if the system fails to be ergodic in this way, it may fail in others also.

### REMD with Nosé-Poincaré is not ergodic

Similarly, we will show that the Nosé-Poincaré dynamics are not ergodic, and that this implies that REMD using Nosé-Poincaré isothermal components fails to be ergodic.

**Lemma 6.** *Neither the Nosé-Poincaré method [Bond et al., 1999] nor the original Nosé method is ergodic on  $\mathcal{Q} \times \mathcal{P}$ .*

*Proof.* The Nosé-Poincaré system is Hamiltonian and thus preserves the Hamiltonian (5.5) given by  $\tilde{\mathcal{H}} = s(\mathcal{H}_{\text{Nosé}} - \mathcal{H}_0)$ . Because  $\mathcal{H}_0$  is a constant chosen such that the initial value of  $\tilde{\mathcal{H}}$  is zero, the value of  $\mathcal{H}_{\text{Nosé}}$  is also preserved by Nosé-Poincaré dynamics. The following argument uses only the preservation of  $\mathcal{H}_{\text{Nosé}}$  and so applies to both Nosé-Poincaré and Nosé dynamics. Define two sets

$$A = \left\{ (\mathbf{q}, \mathbf{p}, s, p_s) : |U(\mathbf{q})| < \epsilon; \sum_i \frac{\|\mathbf{p}_i\|^2}{2m_i} < \alpha; |gkT \ln s| < \beta \right\},$$

$$B = \left\{ (\mathbf{q}, \mathbf{p}, s, p_s) : U(\mathbf{q}) > V; \sum_i \frac{\|\mathbf{p}_i\|^2}{2m_i} > 1 \right\},$$

with  $V$  chosen as follows. Note that  $|gkT \ln s| < \beta$  implies  $s^{-2} < e^{2\beta/gkT}$  so for  $(\mathbf{q}, \mathbf{p}, s, p_s) \in A$

$$\sum_i \frac{\|\mathbf{p}_i\|^2}{2m_i s^2} < \epsilon e^{2\beta/gkT} \triangleq \gamma,$$

and so  $V$  can be chosen to satisfy  $V > \alpha + \beta + \gamma + \epsilon - \frac{gkT}{2}[1 + \ln 2 - \ln(gkT)]$ . Then a dynamics preserving  $\mathcal{H}_{\text{Nosé}}$  and starting from  $A$  cannot reach  $B$ , because for potential energy  $U(\mathbf{q})$  to increase to  $V$  requires

$$\sum_i \frac{\|\mathbf{p}_i\|^2}{2m_i s^2} + \frac{p_s^2}{2Q} + gkT \ln s < \alpha + \beta + \gamma - V.$$

To see that this cannot occur, let  $c = gkT$  and notice that in the set  $B$ ,

$$\sum_i \frac{\|\mathbf{p}_i\|^2}{2m_i s^2} + \frac{p_s^2}{2Q} + c \ln s \geq \frac{1}{s^2} + c \ln s,$$

since  $\sum_i \frac{\|\mathbf{p}_i\|^2}{2m_i} > 1$ . Differentiation shows that  $f(s) = \frac{1}{s^2} + c \ln s$  achieves a minimum of  $\frac{c}{2}[1 + \ln 2 - \ln c]$  at  $s = \sqrt{2/c}$ , so for positive  $s$ :

$$\sum_i \frac{\|\mathbf{p}_i\|^2}{2m_i s^2} + \frac{p_s^2}{2Q} + gkT \ln s \geq \frac{gkT}{2} [1 + \ln 2 - \ln(gkT)] > \alpha + \beta + \gamma - V.$$

Therefore preserving  $\mathcal{H}_{\text{Nosé}}$  requires  $U(\mathbf{q}) < V$ , so set  $B$  can never be reached.  $\square$

Note that because Nosé-Poincaré is time-reversible,  $A$  cannot be reached from  $B$  either. Looking at the choice of sets used in the lemma, we see that if we are unable to choose an initial configuration with sufficiently low potential energy, *it may be impossible to reach the region including the minimum potential energy configuration* with Nosé-Poincaré or Nosé-Hoover dynamics. So the failure to be ergodic has significant practical consequences; we show examples where exactly this phenomenon occurs in Section 5.5. We conclude this section by showing that, as with Nosé-Hoover, the non-ergodicity at individual temperatures translates to non-ergodicity of the replica-exchange dynamics as well.

**Theorem 7.** REMD using Nosé-Poincaré dynamics is not ergodic for unbounded positive potential energy  $U(\mathbf{q}) > 0$ .

*Proof.* Given initial configurations  $\mathbf{x}_{T_i}^0 = (\mathbf{q}_{T_i}^0, \mathbf{p}_{T_i}^0, s_{T_i}^0, p_{s,T_i}^0)$  for  $i = 1 \dots k$ , define constants

$$a = \max_i \{U(\mathbf{q}_{T_i}^0)\},$$

$$b = \max_{i,j} \left\{ \sum_j \frac{\|\mathbf{p}_{T_i,j}^0\|^2}{2m_j(s_{T_i}^0)^2} + \frac{(p_{s,T_i}^0)^2}{2Q} + gkT_j \ln s_{T_i}^0 \right\},$$

$$c = \min_{i,s} \left\{ \frac{1}{s^2} + gkT_i \ln s \right\},$$

and define the sets

$$A = \left\{ \mathbf{x} : U(\mathbf{q}) < a; \sum_i \frac{\|\mathbf{p}_i\|^2}{2m_i} + \frac{p_s^2}{2Q} + gkT_i \ln s < b \right\},$$

$$B = \left\{ \mathbf{x} : U(\mathbf{q}) > k(a + b + c); \sum_i \frac{\|\mathbf{p}_i\|^2}{2m_i} > 1 \right\}.$$

From the proof of Lemma 3, we can see that for any individual temperature,  $\pi_{T_i}(B \cap S_{T_i}^{-n} A) = 0$  because the maximum possible value for  $U(\mathbf{q})$  at any temperature is less than  $a + b + c$ . For Nosé-Poincaré dynamics, unlike for Nosé-Hoover dynamics, the conserved quantity depends on  $T_i$ . However, the total increase in potential energy over all replicas is bounded by  $k(a + b + c)$  since  $(a + b + c)$  is the maximum increase at any temperature due to conservation of the Hamiltonian. Thus for any individual replica the total increase in  $U(\mathbf{q})$  is also bounded by  $k(a + b + c)$ . Now define the

sets

$$A^* = \left\{ \{\mathbf{x}_{T_i}\}_{i=1}^k : U(\mathbf{q}_{T_i}) < a; \sum_j \frac{\|\mathbf{p}_{T_i,j}\|^2}{2m_j} + \frac{p_{s,T_i}^2}{2Q_s} + gkT_i \ln s_{T_i} < b \quad \forall i \right\},$$

$$B^* = \left\{ \{\mathbf{x}_{T_1}\}_{i=1}^k : U(\mathbf{q}_{T_i}) > n(a + b + c); \sum_j \frac{\|\mathbf{p}_{T_i,j}\|^2}{2m_j} > 1 \quad \forall i \right\}.$$

For every  $T_i$ , we have  $\pi_{T_i}(B \cap S_{T_i}^{-n} A) = 0$  and  $\pi(B^* \cap S_2^{-n} A^*) = 0$ , so we have  $\pi(B^* \cap (S^{*-n} A^*)) = 0$ .  $\square$

### 5.3.6 Nosé-Poincaré Chains

Following the apparent success of chains in improving the behavior of Nosé-Hoover dynamics, chains have also been added to the Nosé-Poincaré integrator [Bond et al., 1999, Laird and Leimkuhler, 2003, Leimkuhler and Sweet, 2004]. Unfortunately, as with the Nosé-Hoover chains, these methods which aim to 'enhance ergodicity' [Laird and Leimkuhler, 2003] do not make the system ergodic. The general form of the Nosé-Poincaré chains introduced by Laird and Leimkuhler [2003] have Hamiltonian  $\mathcal{H} = s(\hat{\mathcal{H}} - \hat{\mathcal{H}}_0)$  where

$$\hat{\mathcal{H}} = \sum_{i=1}^p \frac{\|\mathbf{p}_i\|^2}{2m_i s^2} + U(\mathbf{q}) + gkT \ln s + \frac{\mathbf{p}_s^2}{2Q_s} + f(s, p_s, \sigma_i, p_{\sigma_i}). \quad (5.7)$$

Laird and Leimkuhler [2003] introduce two chain methods, both using functions  $f$  that are strictly positive. However, since  $\hat{\mathcal{H}} - \hat{\mathcal{H}}_0 = 0$  by conservation of the Hamiltonian, by Lemma 6,  $(\hat{\mathcal{H}} - U(\mathbf{q}))$  has a minimum for any initial values of  $\mathbf{q}, \mathbf{p}, s, p_s$ . Thus for  $f$  positive  $U$  remains bounded above, and the dynamics are not ergodic. More recently, Leimkuhler and Sweet [2004] use functions  $f$  that can be

take both positive and negative values, so the above proof does not extend directly, and it remains unclear if the method can be ergodic.

## 5.4 Stochastic dynamics

An alternative to deterministic molecular dynamics (2.1) is the use of stochastic dynamics, including hybrid Monte Carlo [Duane et al., 1987] and Langevin or Brownian dynamics [Pastor, 1994], where the stochastic element corresponds to solvent collisions/thermal fluctuation. In contrast to deterministic dynamics, establishing ergodicity of stochastic dynamics is generally considerably easier due to the probabilistic nature of individual transitions.

### 5.4.1 Metropolis correction and Hybrid Monte Carlo

An alternative is to use deterministic dynamics simulations to generate *proposed* moves, which are then accepted or rejected according to an appropriate Metropolis-Hastings criteria [Metropolis et al., 1953, Hastings, 1970]. The *hybrid Monte Carlo* (HMC) algorithm [Duane et al., 1987, Neal, 1993] simulates a Hamiltonian system at temperature  $T$  starting from initial position and momentum vectors  $(\mathbf{q}_0, \mathbf{p}_0)$  via the following iteration:

1. Generate a random momentum vector  $\mathbf{p} \sim N(\mathbf{0}, (k_B T) \mathbf{I}_{3d})$ , where  $N(\mu, \Sigma)$  denotes the normal (Gaussian) distribution.
2. Simulate  $L$  steps of MD using a time-reversible volume-preserving integrator to generate a proposed new state  $(\mathbf{x}', \mathbf{p}')$

3. Accept the proposed state  $(\mathbf{q}', \mathbf{p}')$  with probability  $\alpha$ , otherwise reject and remain at current state  $(\mathbf{q}, \mathbf{p})$ , where  $\alpha((\mathbf{q}, \mathbf{p}); (\mathbf{q}', \mathbf{p}')) = \min \{1, \exp(\Delta\mathcal{H}/k_B T)\}$  and  $\Delta\mathcal{H} = \mathcal{H}(\mathbf{q}, \mathbf{p}) - \mathcal{H}(\mathbf{q}', \mathbf{p}')$ .

The resulting stochastic process is  $\pi_{\mathcal{H}}$ -invariant as long as the dynamics are time-reversible and volume-preserving, as argued by [Duane et al., 1987, Neal, 1993] and shown carefully by [Liu, 2001]. In addition, the randomization of the momenta guarantees that the underlying stochastic process is ergodic, as we show below. Here  $L$  must be chosen along with  $\Delta t$  to yield an appropriate acceptance rate.

Hybrid Monte Carlo can be viewed as introducing stochastic corrections to the deterministic dynamics, correcting for the lack of both invariance and irreducibility. The Metropolis acceptance provides an exact correction for the approximate conservation of the Hamiltonian arising from time discretization. Similarly, we show below that the randomization of momenta turns the reducible deterministic dynamics into an irreducible stochastic process.

The HMC construction applies for any time-reversible volume-preserving dynamics. When applied to microcanonical dynamics it yields the HMC algorithm of [Duane et al., 1987]. In Section 5.5, we apply it to Nosé-Poincaré dynamics using the integrator in Section 5.3.4, yielding a  $\pi$ -invariant ergodic algorithm due to the symplectic property of the Nosé-Poincaré dynamics and integrator. We also apply the HMC correction to the Berendsen-thermostat MD, which should be seen only as a heuristic correction for ergodicity but does not yield  $\pi$ -invariance, since the Berendsen heat-bath is neither measure-preserving nor time-reversible.

## Ergodicity of hybrid Monte Carlo

**Lemma 8.** *Hybrid Monte Carlo using the leap-frog (2.9) or the Nosé-Poincaré (5.3.4) integrators is ergodic.*

*Proof.* Denote by  $S$  the one step integrator mapping, and let  $K_H$  denote the transition kernel associated with one step of HMC:

$$\begin{aligned} K_H((\mathbf{q}, \mathbf{p}), A) &= \int_{\mathcal{P}} f(\tilde{\mathbf{p}}) \mathbf{1}_A(S^L(\mathbf{q}, \tilde{\mathbf{p}})) \alpha((\mathbf{q}, \mathbf{p}), S^L(\mathbf{q}, \tilde{\mathbf{p}})) d\tilde{\mathbf{p}} \\ &\quad + \mathbf{1}_A((\mathbf{q}, \mathbf{p})) \left[ 1 - \int_{\mathcal{P}} f(\tilde{\mathbf{p}}) \alpha((\mathbf{q}, \tilde{\mathbf{p}}), S^L(\mathbf{q}, \tilde{\mathbf{p}})) d\tilde{\mathbf{p}} \right], \end{aligned}$$

where  $f$  denotes the multivariate normal density  $N(\mathbf{0}, (k_B T) \mathbf{I}_{3d})$ . Liu [2001] formalizes argument of [Duane et al., 1987, Neal, 1993] to show that  $S$  time-reversible and volume-preserving implies  $K_H$  is  $\pi$ -invariant. Thus we need only show that  $K_H$  is also irreducible.

For a  $\pi$ -invariant stochastic process to be irreducible (and hence ergodic), it suffices that it be  $\phi$ -irreducible for some distribution  $\phi$  [Meyn and Tweedie, 1993]. That is, for every  $A \subset \mathcal{X}$  with  $\phi(A) > 0$ , there exists an  $n$  such that  $K_H^n(\mathbf{x}, A) > 0$  for all  $\mathbf{x} \in \mathcal{X}$ .  $K$  is *strongly*  $\phi$ -irreducible if this holds for  $n = 1$ . We show that HMC is strongly  $\phi$ -irreducible, first for  $L = 1$  MD step and then for general  $L$ .

Define the set  $B = \{(\mathbf{q}, \mathbf{p}) : a < U(\mathbf{q}) < b\}$  and let  $\phi$  be the uniform distribution over  $B$ . Then for any measurable  $A \subseteq B$  and  $(\mathbf{q}, \mathbf{p}) \in \mathcal{X}$  we require  $K_H((\mathbf{q}, \mathbf{p}), A) > 0$ . For  $S$  volume-preserving, it suffices that

$$\forall \mathbf{q}' \in \mathcal{Q}, \exists \tilde{\mathbf{p}} \in \mathcal{P} \text{ such that } S(\mathbf{q}, \tilde{\mathbf{p}}) = (\mathbf{q}', \mathbf{p}') \text{ for some } \mathbf{p}' \quad (5.8)$$

Then for  $A \subseteq B$  measurable, the set  $P_{\mathbf{q},A}^1 = \{\mathbf{p} : S(\mathbf{q}, \mathbf{p}) \in A\}$  of momenta that take  $\mathbf{q}$  to  $A$  in one step is also measurable (i.e.  $\pi(P_{\mathbf{q},A}^1) > 0$ ), and therefore:

$$K_H((\mathbf{q}, \mathbf{p}), A) \geq \int_{P_{\mathbf{q},A}^1} f(\tilde{\mathbf{p}}) \alpha((\mathbf{q}, \tilde{\mathbf{p}}), S(\mathbf{q}, \tilde{\mathbf{p}})) d\tilde{\mathbf{p}} > 0, \quad (5.9)$$

since  $f(\mathbf{p}')$  and  $\alpha((\mathbf{q}, \mathbf{p}), (\mathbf{q}', \mathbf{p}'))$  are strictly positive for  $\mathcal{H}(\mathbf{q}', \mathbf{p}') < \infty$ . To see that (5.8) holds for the leap-frog integrator (2.9), note that for any  $\tilde{\mathbf{q}} \in \mathcal{Q}$  we have  $\tilde{\mathbf{p}}_i = m_i(\tilde{\mathbf{q}}_i - \mathbf{q}_i)/\Delta t + \frac{\partial}{\partial \mathbf{q}_i} U(\mathbf{q}) \frac{\Delta t}{2}$ . To see that (5.8) holds for Nosé-Poincaré, note that for any  $\mathbf{q}, \tilde{\mathbf{q}}$ , and any  $s, p_s$  we have  $\tilde{\mathbf{p}}_i = (m_i(\tilde{\mathbf{q}}_i - \mathbf{q}_i)/\Delta t + \frac{\partial}{\partial \mathbf{q}_i} U(\mathbf{q}) \frac{\Delta t}{2})(1 + p_s \Delta t / 4Q)^2 s$ . To see that this argument remains true for  $L > 1$ , recall that  $S$  is volume-preserving and time-reversible, so  $A$  measurable implies  $S^{-L}(A)$  measurable implies  $P_{\mathbf{q},S^{-L}(A)}^1$  measurable, and (5.9) holds with  $S$  replaced by  $S^L$ .

Therefore we have  $K_H(\mathbf{x}, A) > 0$  for all  $\mathbf{x} \in \mathcal{X}$  and  $\phi(A) > 0$ , so HMC is (strongly)  $\phi$ -irreducible, and therefore irreducible and ergodic.  $\square$

### 5.4.2 Langevin Dynamics

For comparison, we include another common choice for stochastic dynamics, namely Langevin dynamics. Langevin dynamics is described by the stochastic ordinary differential equation:

$$\begin{aligned} d\mathbf{q} &= \mathbf{p} dt \\ d\mathbf{p} &= -\gamma \mathbf{p} dt - \nabla U(\mathbf{q}) + \sigma dW, \end{aligned}$$

where  $W$  is standard  $p$ -dimensional Brownian motion, and  $U$  is the potential energy as before. We use the popular BBK integrator [Brünger et al., 1984]:

$$\begin{aligned}\mathbf{p}_i(t + \frac{\Delta t}{2}) &= \left(1 - \frac{\gamma \Delta t}{2}\right) \mathbf{p}_i(t) + \frac{\Delta t}{2} \left(-\frac{\partial U}{\partial \mathbf{q}_i} + \frac{\sigma}{\sqrt{\Delta t}} Z(t)\right), \\ \mathbf{q}_i(t + \Delta t) &= \mathbf{q}_i(t) + \Delta t \mathbf{p}_i \left(t + \frac{\Delta t}{2}\right), \\ \mathbf{p}_i(t + \Delta t) &= \frac{\mathbf{p}_i \left(t + \frac{\Delta t}{2}\right) + \frac{\Delta t}{2} \left(-\frac{\partial U}{\partial \mathbf{q}_i} + \frac{\sigma}{\sqrt{\Delta t}} Z(t + \Delta t)\right)}{1 + \frac{\gamma \Delta t}{2}},\end{aligned}$$

where  $Z(t)$  is a vector of standard normal random variables.

Because of the random motion introduced by the Brownian motion, Langevin dynamics is irreducible, and has been shown to be ergodic under certain conditions on  $U(\mathbf{q})$  and for specific integrators [Mattingly et al., 2002]. However those conditions are not satisfied by standard molecular mechanics forcefields and integrators, and it remains to be seen if ergodicity can be established for these systems. As such the Langevin dynamics results in Section 5.5 are provided only for illustration. Note that when HMC is applied to Langevin dynamics ( $L = 1$ ), it yields an algorithm similar to the Metropolis-corrected Langevin diffusion algorithm [Roberts and Tweedie, 1996] which corrects for the numerical error introduced by discretizing Langevin diffusion. However it is unclear if this remains measure-preserving using the BBK integrator.

## 5.5 Examples

The practical impact of the failures of invariance and ergodicity described in the previous sections can be illustrated on simple examples, where the effect on the

entire ensemble may be visualized directly.

### 5.5.1 Harmonic oscillators and Gaussian mixtures

We first consider two model Hamiltonian systems. The first has target Boltzmann distribution given by a bivariate standard normal (Gaussian) distribution:

$$\pi_1(\mathbf{q}) = \frac{1}{2\pi\sigma^2} \exp \left\{ -\frac{1}{2\sigma^2} \|\mathbf{q}\|^2 \right\},$$

and the second given by a mixture of bivariate normals centered at (0,0) and (8,8), respectively:

$$\pi_2(\mathbf{q}) = \frac{\rho}{2\pi\sigma^2} \exp \left\{ -\frac{1}{2\sigma^2} \|\mathbf{q}\|^2 \right\} + \frac{(1-\rho)}{2\pi\sigma^2} \exp \left\{ -\frac{1}{2\sigma^2} \|\mathbf{q} - 8\|^2 \right\}.$$

In the examples below we use  $\sigma^2 = 1$  and  $\rho = \frac{1}{2}$ . Taking  $k_B T = \sigma^2$ , the potential energy of  $\pi_1$  is given by  $U(\mathbf{q}) = -\log(\pi_1(\mathbf{q})) = \log 2\pi + \frac{1}{2} \sum_{i=1}^2 x_i^2$ . Combining this with a kinetic term  $K(\mathbf{p}) = \frac{1}{2} \sum_{i=1}^2 p_i^2$  (with masses  $m_1 = m_2 = 1$ ) yields the Hamiltonian:

$$\mathcal{H}_1(\mathbf{q}, \mathbf{p}) = U(\mathbf{q}) + K(\mathbf{p}) = \log 2\pi + \frac{1}{2} \sum_{i=1}^2 x_i^2 + \frac{1}{2} \sum_{i=1}^2 p_i^2. \quad (5.10)$$

and the resulting Hamiltonian system

$$\dot{\mathbf{q}}_i = \frac{\partial \mathcal{H}_1}{\partial \mathbf{p}_i} = \mathbf{p}_i, \quad \dot{\mathbf{p}}_i = -\frac{\partial \mathcal{H}_1}{\partial \mathbf{q}_i} = -\mathbf{q}_i,$$

is easily recognized as simple harmonic motion in the plane, with solution

$$\mathbf{q}_i = A_i \cos t + B_i \sin t \quad (5.11)$$

obtained by writing the system as a linear second order differential equation  $\ddot{\mathbf{q}}_i = -\mathbf{q}_i$ , where  $\mathbf{q}_0 = (A_1, A_2)$  and  $\mathbf{p}_0 = (B_1, B_2)$  are the initial position and momentum, respectively. Although (5.11) is the unique solution for (5.10) with initial conditions  $(\mathbf{q}_0, \mathbf{p}_0)$ , this solution trajectory does not reach all points of equal energy from a single initial condition, but instead traverses a set of points of equal energy along the curves  $\mathbf{q}_i = A_i \cos t + B_i \sin t$ . Thus the Hamiltonian dynamics fail to be ergodic even under the microcanonical ensemble.

Similarly, the Hamiltonian for  $\pi_2$  is of the form

$$\mathcal{H}_2(\mathbf{q}, \mathbf{p}) = \log \left( e^{-\frac{1}{2}\|\mathbf{q}\|^2} + e^{-\frac{1}{2}\|\mathbf{q}-\mathbf{8}\|^2} \right) + \frac{1}{2}\|\mathbf{p}\|^2 - \log(4\pi).$$

Dynamical simulation of these Hamiltonian systems can therefore be applied to generate the corresponding Boltzmann ensembles  $\pi_1$  and  $\pi_2$ .

*Numerical results* To demonstrate the practical impact of the theoretical results of Section 5.3.5 on commonly used simulation protocols, we compare several of the dynamics analyzed in previous sections for simulating the Boltzmann ensembles  $\pi_1$  and  $\pi_2$ : microcanonical dynamics with a leap-frog integrator, canonical dynamics based on leap-frog with Berendsen heat bath, Nosé-Poincaré, and stochastic Langevin dynamics.

Leap-frog (with or without a Berendsen heat bath) and Langevin dynamics used a step-size of 0.1s, and Nosé-Poincaré used a 0.01s step-size. Simulations without hybrid Monte Carlo or replica-exchange were run for 100,000 steps, or 1,000 seconds. Hybrid Monte Carlo proposal trajectories utilized  $L = 50$  steps of the corresponding numerical integrator (leap-frog, leap-frog with Berendsen with  $\tau_T = 10$ , BBK, or the

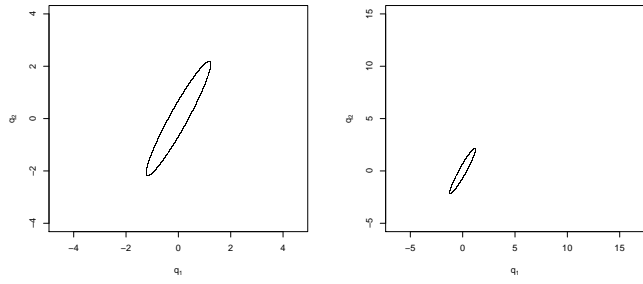
Nosé-Poincaré integrator (Section 5.3.4)). Step sizes and  $L$  were chosen to achieve a HMC acceptance rate between 20% and 60%. REMD utilized 10 parallel MD simulations, attempted swaps every 100 steps, and ran for 1,000s. Replica-exchange with hybrid Monte Carlo followed each 50 step trajectory with a Metropolis acceptance, before proposing a temperature swap.

The results of these simulations are shown in Figures 5.1-5.4. In each figure, simulations of  $\pi_1$  are shown in the left column, and  $\pi_2$  in the right. Figure 5.1 compares microcanonical MD and canonical MD via a Berendsen heat-bath, Nosé-Poincaré, and Langevin dynamics, for both target distributions. It is clearly seen that the microcanonical, Berendsen, and Nosé-Poincaré dynamics are not ergodic. The Nosé-Poincaré shows clear signs of not being able to reach the low-energy region near the origin, as indicated in Section 5.3.5 as a potential consequence of Theorem 7. Langevin dynamics (without the HMC correction) appears to generate the target ensemble  $\pi_1$ , but fails to cross the energy barrier in  $\pi_2$ .

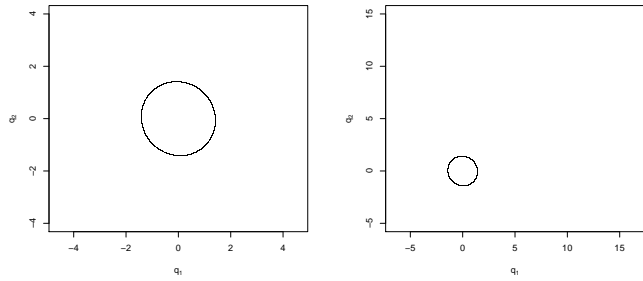
Figure 5.2 compares REMD simulations, each performed using the respective isothermal dynamics algorithm for its (10) individual replicas. Again microcanonical dynamics generates constant- $\mathcal{H}$  trajectories dependent on the initial coordinates; since each replica has distinct random initial coordinates, many additional trajectories are observed, but the simulation clearly still fails to be ergodic. Similarly, the Berendsen thermostat again fails to generate the correct ensemble. Nosé-Poincaré appears to remain reducible, restricted to orbits based on initial coordinates. Langevin dynamics is now able to cross the energy barrier in  $\pi_2$ , and appears to generate both ensembles correctly.

Figure 5.3 repeats the experiments of Figure 5.1 (without replica-exchange), but utilizing the hybrid Monte Carlo correction described in Section 5.4. The micro-canonical dynamics now becomes standard Hybrid Monte Carlo [Duane et al., 1987] and is ergodic as proven in Section 5.4, thus will generate the correct  $\pi_1$  ensemble. However it fails to cross the energy barrier of  $\pi_2$  in the absence of replica-exchange. (Although it is ergodic and will eventually cross with probability one, this may take a long time.) The Berendsen thermostat still shows significant artifacts arising from its failure to be measure preserving. Nosé-Poincaré actually crosses the barrier of  $\pi_2$ , but not sufficiently easily to equilibrate between the two energy wells without replica-exchange. Langevin dynamics also fails to cross the energy barrier of  $\pi_2$  in the absence of replica-exchange.

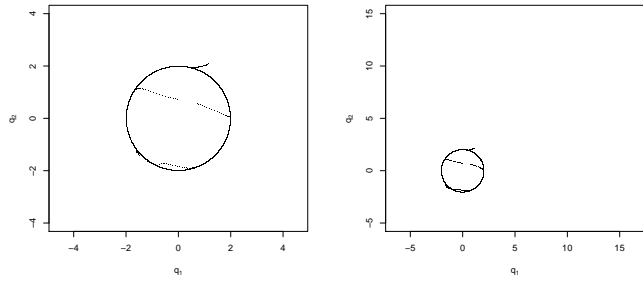
Finally, Figure 5.4 shows the results of using the HMC correction in combination with replica-exchange. In this case all of the algorithms except the Berendsen thermostat are measure-preserving and ergodic, and able to cross the energy barrier, so generate the correct ensembles for both  $\pi_1$  and  $\pi_2$ . Note that in these cases, there is no distinction between 'replica-exchange' using the HMC correction, and the original parallel tempering algorithm Geyer [1991]; the underlying Markov chains just happen to be being generated by hybrid Monte Carlo [Duane et al., 1987, Neal, 1993]. The Berendsen thermostat, which is not measure-preserving, still clearly fails to converge to the proper ensembles as expected.



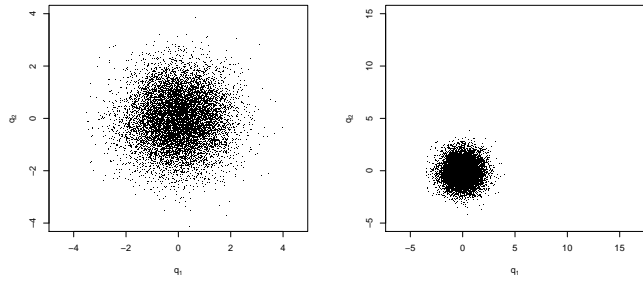
Leap-frog



Leap-frog with Berendsen heat bath



Nosé-Poincaré



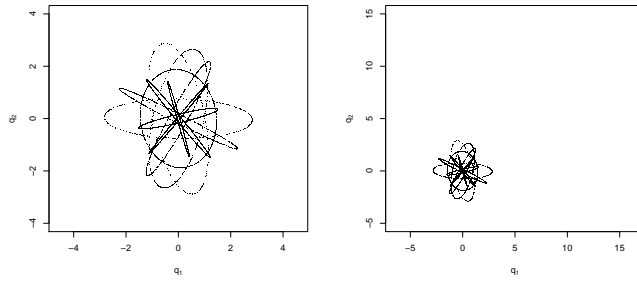
Langevin

**Figure 5.1:** Comparison of four dynamics simulation algorithms for the target distributions  $\pi_1$  (left column) and  $\pi_2$  (right column) defined in text. Algorithms are (top to bottom): microcanonical dynamics using leap-frog integrator; canonical dynamics using Berendsen heat bath; canonical dynamics using Nosé-Poincaré integrator; and canonical Langevin dynamics.

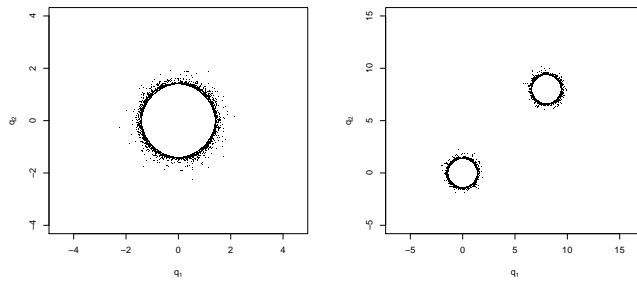
### 5.5.2 Alanine dipeptide

To demonstrate the implications for a molecular system under a standard forcefield, we simulated the small Alanine dipeptide (see Figure 5.5) under REMD using the Berendsen thermostat as commonly done in practice for peptide simulations [Sugita and Okamoto, 1999, Garcia and Sanbonmatsu, 2002, Smith et al., 2002, Daura et al., 1998, 1999], and compared the results to those obtained using parallel tempering with hybrid Monte Carlo, which we have shown guarantees invariance and ergodicity. Results for Langevin dynamics are also shown for comparison. Alanine dipeptide has been extensively studied computationally and experimentally; we choose it here because the molecule has only two internal dihedral angles, making it possible to ensure adequate sampling quickly, and to easily visualize the generated ensemble. Each simulation was run without solvent under the AMBER94 forcefield as implemented in the NAMD suite of programs [Phillips et al., 2005], with 1fs time step and 10Åcutoff, at a target temperature  $T_0$  of 273K.

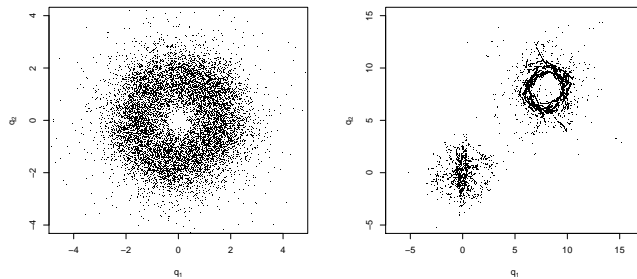
In each case, three Berendsen-coupling REMD, three HMC parallel tempering, and three Langevin dynamics parallel tempering simulations were run, each using ten replicas with temperatures distributed exponentially between 273K and 2000K, and swaps between neighboring temperatures attempted every 100 steps. For all three algorithms, the three simulations were initialized to three distinct  $\phi/\psi$  conformations, representing regions of favorable energy determined by trial simulations and confirmed in previous studies in the literature:  $(\phi, \psi) \in \{(-75, 40), (-150, 160), (60, -50)\}$ . Total running time was 2ns per replica, well beyond that needed for equilibration and production phases; convergence was established using parallel simulation convergence



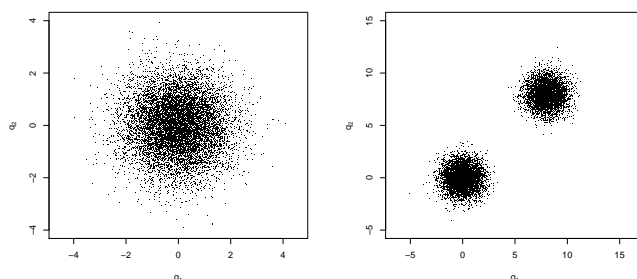
Leap-frog



Leap-frog with Berendsen heat bath

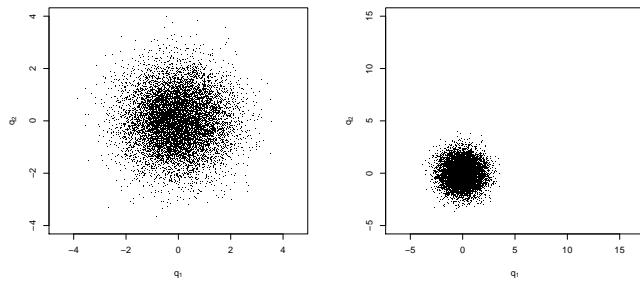


Nosé-Poincaré

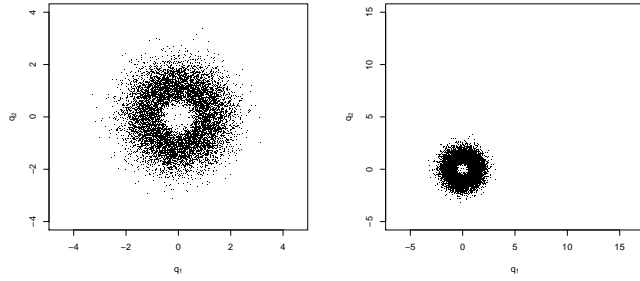


Langevin

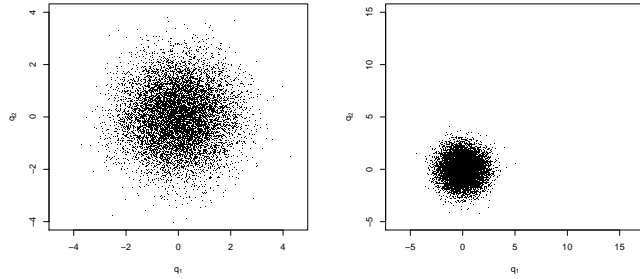
**Figure 5.2:** Replica-exchange dynamics using each of the four dynamics algorithms, for simulating  $\pi_1$  (left) and  $\pi_2$  (right). Each REMD involves 10 replicas of the corresponding dynamics.



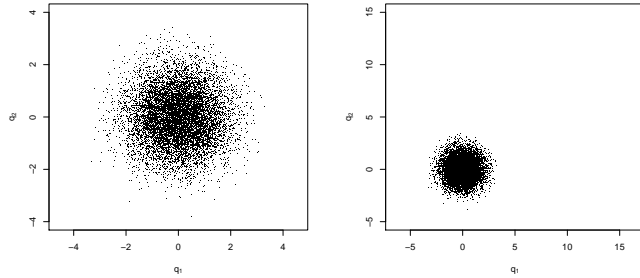
Leap-frog



Leap-frog with Berendsen heat bath

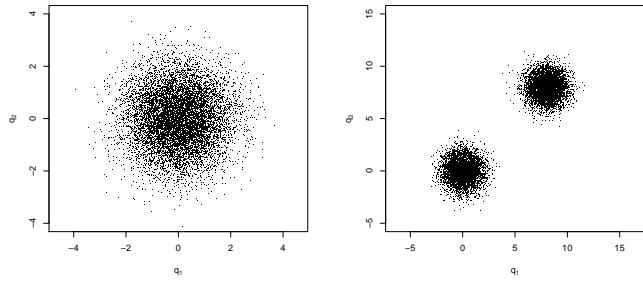


Nosé-Poincaré

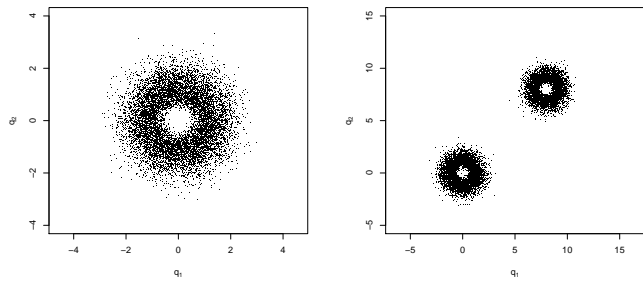


Langevin

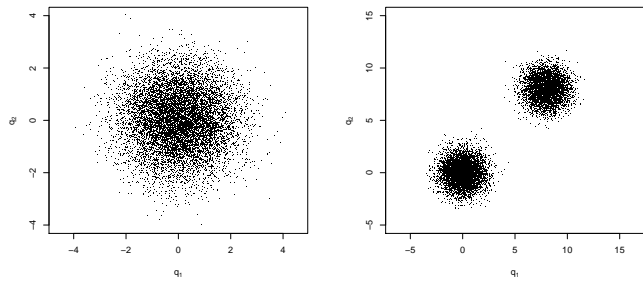
**Figure 5.3:** The four dynamics algorithms of Figure 5.1, augmented with the hybrid Monte Carlo correction described in text.



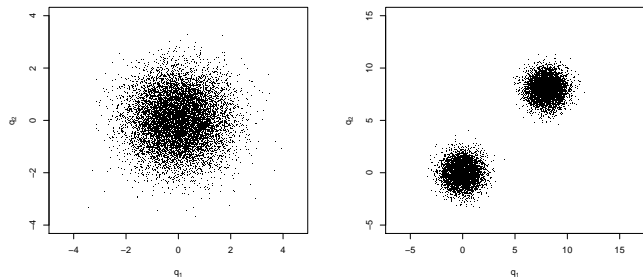
Leap-frog



Leap-frog with Berendsen heat bath



Nosé-Poincaré



Langevin

**Figure 5.4:** Replica-exchange simulations using the four respective dynamics algorithms, each with the hybrid Monte Carlo correction. The microcanonical and Langevin algorithms thus become parallel tempering HMC and parallel tempering Langevin dynamics respectively, both of which are measure-invariant and ergodic.

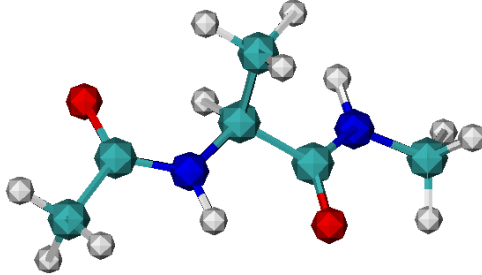


**Figure 5.5:** Molecular structure of alanine dipeptide.

diagnostics as described previously in Chapter 3.

The resulting ensembles generated at  $T_0$  (273K) are shown in Figure 5.6. The non-measure-preserving Berendsen thermostat has clearly altered the target Boltzmann ensemble, to the extent that an entire energy well ( $\phi > 0$ ) is not preserved. Note that the Berendsen MD leaves that region even when initialized there and never returns, indicating that with REMD it is not a mixing problem. (In the absence of replica-exchange, Langevin dynamics is unable to cross the barrier between energy wells even in this small system, sampling the  $\phi > 0$  region only when initialized there; plots not shown.) This example demonstrates that for molecular systems under standard forcefields, the failure of the commonly used Berendsen thermostat to be measure-preserving can have a significant impact on the ensemble simulated. Such effects clearly compromise attempts to validate and refine forcefields based on calculation of experimental quantities.

### 5.5.3 High dimensional systems and irregular energy landscapes

It is often suggested that ergodicity problems such as those identified here arise only in small systems with low or weakly coupled degrees of freedom. However, our theorems of Section 5.3 hold for systems of *any* size. Thus the belief that ergodicity

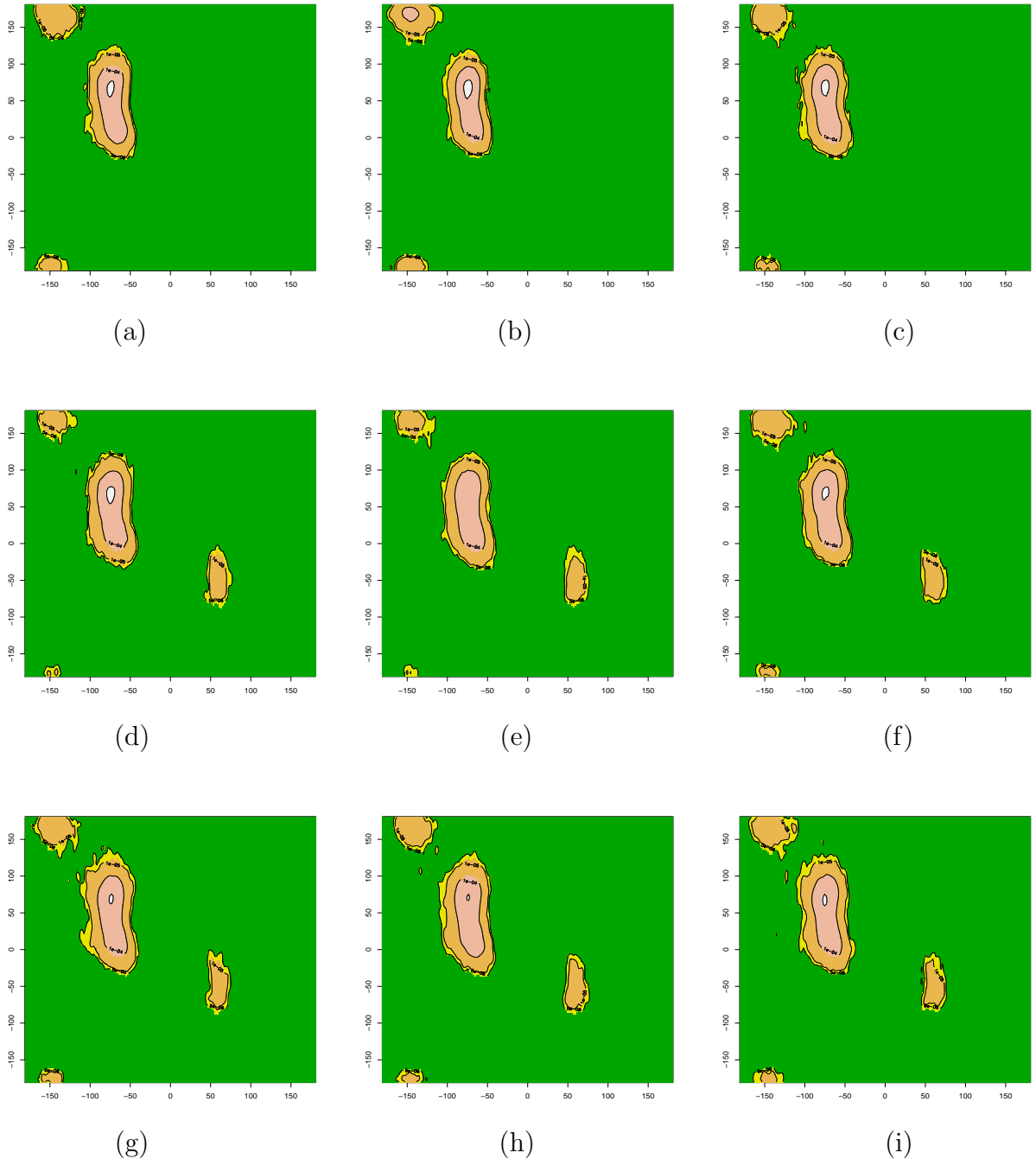


**Figure 5.6:** Heatmap plots with an overlayed contour plot of the Ramachandran plots generated by the 273K replica of the REMD simulations of Alanine dipeptide with Berendsen coupling (a-c) versus Hybrid Monte Carlo (d-f). Also shown for comparison are Langevin dynamics (g-i). Simulations were started from the three major energy well regions of  $(\phi, \psi)$  space ( $(-75, 40)$  for (a,e,g),  $(-150, 160)$  for (b,d,h),  $(60, -50)$  for (c,f,i)), and run to equilibrium.

failures do not persist in larger systems most likely simply reflects the difficulty of accurately observing complex high-dimensional ensembles. This confusion further emphasizes the importance of establishing formal proofs of algorithm properties, since empirical observation may fail to identify non-ergodic behavior in complex high-dimensional systems.

To demonstrate the persistence of these failures in higher dimensions and under more complex energy landscapes, we extended our simulation experiments to two additional target ensembles. These are (a) a 50-dimensional normal distribution  $N(0, \Sigma)$  with random positive-definite covariance matrix  $\Sigma$  generated by  $\Sigma = M^T M$ , with  $M$  a  $50 \times 50$  matrix of independent  $N(0, 1)$  random variates, generating a highly coupled and irregular energy landscape[Roberts and J.S. Rosenthal, 2006]; and (b) a two-component normal mixture in 50 dimensions, also highly-coupled due to two distinct significant energy wells. For each target ensemble we performed REMD simulations using HMC, Berendsen, and Nosé-Poincaré as before; Langevin results were identical to HMC and are omitted for space. Although quantitative summarization and comparison of high-dimensional ensembles is difficult in general, the target ensembles here are chosen to enable this. In particular, the *marginal* distributions of ensemble (a) are all known (normal) and the samples can be evaluated for their ability to generate the correct marginals. Figure 5.7 shows normal quantile-quantile plots for the marginal distributions for the first seven degrees of freedom. Deviations from the diagonal represent departures from the correct distribution; the 'S' shape indicates that the ensembles generated by the Berendsen and NP algorithms have insufficient samples near the mode (energy minimum) and too many farther

away. This indicates the same sort of behavior shown in the two-dimensional case of Figure 5.2, which is easier to visualize in 2D but as shown by the qq plots still persists in high dimensions as well. For further comparison, Figure 5.8 shows the energy histograms for the ensembles generated by the three algorithms. Again it is clear that the ensembles generated by the Berendsen and Nosé-Poincaré dynamics differ significantly from the correct ensemble generated by HMC.

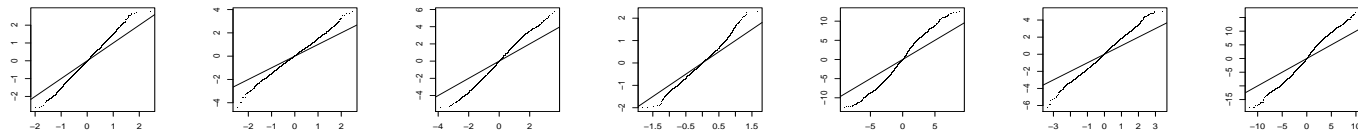
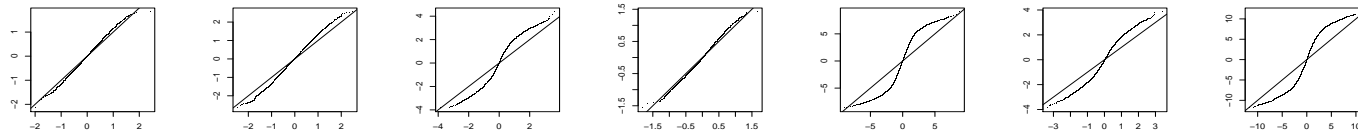
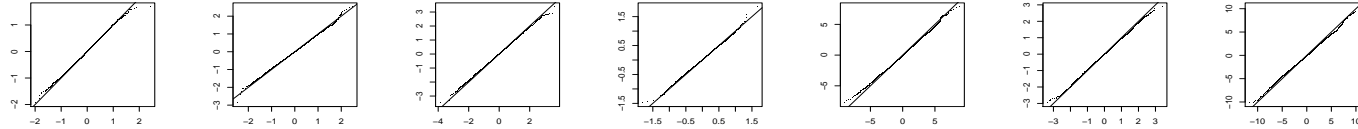


**Figure 5.7:** Normal quantile-quantile plots for the marginal distributions of dimensions one through seven, calculated from the ensembles generated by the hybrid Monte Carlo (first row), Berendsen (second row), and Nosé-Poincaré (third row) algorithms for the high-dimensional random-covariance target ensemble described in the text. Deviations from the diagonal represent departures from the true ensemble, with the 'S' shape indicating heavy tails: regions near the energy minimum are significantly under-sampled by the non-HMC algorithms.

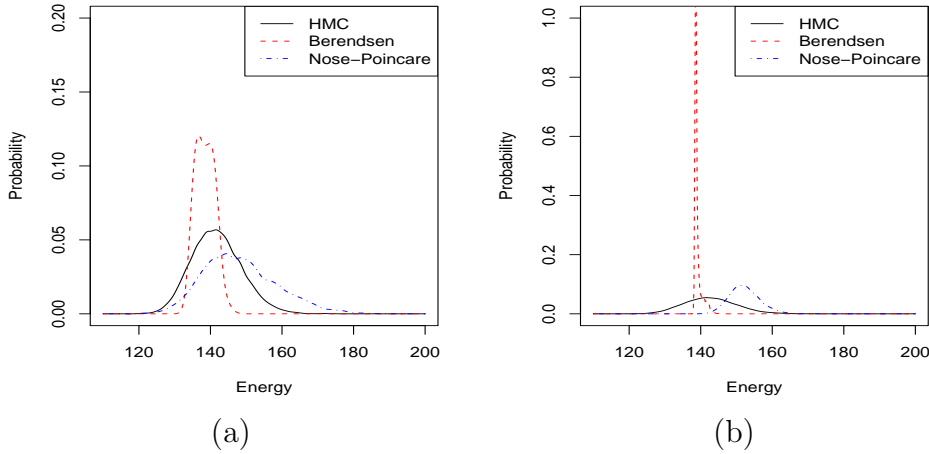


**Figure 5.8:** Energy histograms generated by Berendsen, Nosé-Poincaré, and hybrid Monte Carlo algorithms for two high-dimensional target ensembles: (a) 50-dimensional normal distribution with random covariance matrix, yielding highly irregular coupling, and (b) mixture of two 50-dimensional normals. These energy profiles indicate that the ensembles generated by Berendsen and NP deviate significantly from the correct ensemble generated by HMC.

## 5.6 Discussion

A critical step in improving existing macromolecular forcefields is the comparison of simulated quantities to experimental measurements [Daura et al., 1998, Garcia and Sanbonmatsu, 2002]. To make such comparisons quantitatively, the simulated quantities must accurately reflect the ensemble induced by the associated forcefield. Here we have demonstrated that this may not be the case for the implementations of replica-exchange molecular dynamics currently in use for biomolecular simulation. Failures of isothermal molecular dynamics to yield correct ensembles and ergodic averages, either through failure to preserve measure or failure to be ergodic, persist when these algorithms are used as constant-temperature components of replica-exchange. We have made explicit the theoretical shortcomings of commonly used

algorithms, and demonstrated that these failures can have significant practical impact on even small systems. Our results demonstrate the importance of formal analysis of new simulation methods, where empirical studies may fail to show such defects simply due to the difficulties in evaluating correctness of high-dimensional ensembles.

Fortunately these failures come entirely from the use of deterministic dynamics, and stochastic versions are available which correct these theoretical and practical shortcomings. In deterministic dynamics simulations ergodicity must be *assumed*, and as we have shown this assumption is often incorrect; in contrast, for stochastic dynamics ergodicity can generally be guaranteed by basic theorems of stochastic processes. Since real macromolecules in solvent behave stochastically anyway, there appears to be little advantage to using purely deterministic dynamics methods. Arguments that stochastic thermostats disrupt the ability to simulate dynamic properties such as diffusion coefficients are common (see e.g. Frenkel and Smit [1996], and most of the isothermal dynamics papers cited in Section 5.3), but are in our view overwhelmed by the potential for failures in ergodicity. It is worth emphasizing that if the system is not ergodic, dynamic properties computed can not be assumed accurate in any case. Moreover, the use of replica-exchange dynamics to enable crossing of energy barriers already fundamentally disrupts the dynamics of the  $T_0$  system by configuration swapping. Thus we see little advantage to using deterministic replica-exchange molecular dynamics, over stochastic versions. In the latter case, REMD reduces to the original parallel tempering algorithm from which it was adapted.

# Chapter 6

## Geometric Ergodicity

In this chapter, we shift our focus from asymptotic convergence to the correct Boltzmann ensemble to the rate of convergence: from ergodicity to geometric ergodicity. Our interest in geometric ergodicity stems from the desire to determine the length of simulation needed to obtain a given degree of accuracy of our simulations. In Chapters 3 and 4 we assumed a central limit theorem to make estimates of the error of simulation averages. A sufficient condition for the existence of a central limit theorem is geometric ergodicity [Tierney, 1994]. In this chapter we show geometric ergodicity for a simplified example with the eventual goal of establishing the geometric ergodicity of stochastic differential equations integrating a more general biomolecular potential.

In molecular dynamics simulations it is often stated that simulations were run to equilibrium, meaning simply that the simulations were run for a long time. The concept of ergodicity, while guaranteeing convergence to the correct distribution in the limit, does not address the rate of convergence. Although simulations can be tested statistically for lack of equilibrium as in Chapter 3, without any information

about rate of convergence there is no guarantee that the equilibrium will be reached by any specific finite simulation time.

**Definition 9.** *An ergodic Markov chain with invariant distribution  $\pi$  is geometrically ergodic if there exists a non-negative extended real-valued function  $M$  with  $\pi[M] \leq \infty$  and a positive constant  $\lambda < 1$  such that*

$$\|P^n(x, \cdot) - \pi\|_{TV} \leq M(x)\lambda^n, \quad (6.1)$$

where  $\|\pi\|_{TV} = \sup_{A \in \mathcal{X}} \pi(A) - \inf_{A \in \mathcal{X}} \pi(A)$ .

We first define the space we are working in and give two conditions that we will use to show geometric ergodicity. Consider a Markov chain  $x(t)$  ( $t \in \mathbb{R}^+$ ) on a state space  $\mathcal{X} = \mathbb{R}^d$ . Let  $\mathcal{B}(\mathbb{R}^d)$  denote the Borel  $\sigma$ -algebra on  $\mathbb{R}^d$  and  $\mathcal{B}_\delta(x)$  the open ball of radius  $\delta$  centered at  $x$ . We denote the transition kernel of the Markov chain by

$$P_t(x, A) = \mathbb{P}(x(t) \in A | x(0) = x), \quad t \in \mathbb{R}^+, x \in \mathbb{R}^d, A \in \mathcal{B}(\mathbb{R}^d).$$

We cite two conditions that give geometric ergodicity, the first of which combines a uniform reachability condition with a condition on the transition density.[Mattingly and McKinley, 2008]

**Condition 10.** *The Markov chain or process  $\{x(t)\}$  with transition kernel  $P_t(x, A)$  satisfies, for some fixed compact set  $C \in \mathcal{B}(\mathbb{R}^d)$ , the following*

1. *for some  $y^+ \in \text{int}(C)$ ,  $\forall t > t_0$ ,  $\exists \alpha = \alpha(t)$  such that  $\inf_{x \in C} P_t(x, \mathcal{B}_\delta(y^+)) > \alpha$*
2. *for  $t \in \mathbb{R}^+$  the transition kernel possesses a density  $p_t(x, y)$  such that*

$$P_t(x, A) = \int_A p_t(x, y) dy \quad \forall x \in C, A \in \mathcal{B}(\mathbb{R}^d) \cap \mathcal{B}(C),$$

*and  $p_t(x, y)$  is jointly continuous in  $(x, y) \in C \times C$ .*

The second part of Condition 10 will be satisfied because our SDE is a uniformly elliptic diffusion, and the first part we will show in Section 6.2. The second condition is called a *drift condition* because the purpose of the condition is to ensure the Markov chain does not drift to infinity. A Lyapunov function  $V$  is used in the drift condition and  $\mathcal{F}_n$  denotes the  $\sigma$ -algebra of events up to and including the  $n^{th}$  iteration.

**Condition 11.** *There is a function  $V : \mathbb{R}^d \rightarrow [1, \infty)$ , with  $\lim_{x \rightarrow \infty} V(x) = \infty$ , and real numbers  $a \in (0, 1)$  and  $b \in [0, \infty)$  such that*

$$\mathbb{E}[V(x_{n+1})|\mathcal{F}_n] \leq aV(x_n) + b$$

Conditions 10 and 11 together imply geometric ergodicity.[Meyn and Tweedie, 1993]

## 6.1 Simplified System

We define a stochastic Langevin diffusion constructed to simulate a Boltzmann distribution. We choose a simplified system of two atoms with a simplified potential energy function that maintains key parts of the AMBER potential of Equation 3.1.

The simplified system is shown in Figure 6.1 with potential energy given by

$$U(\mathbf{q}) = K_{12}(|\mathbf{q}_1 - \mathbf{q}_2| - b_{12})^2 + \frac{A_{12}}{|\mathbf{q}_1 - \mathbf{q}_2|^{12}}. \quad (6.2)$$

The first term is the bond length term with bond length parameter  $b_{12} > 0$  and bond weight  $K_{12} > 0$ , and the second term is the dominant part of the van der Waals term with parameter  $A_{12}$ . The other terms in the potential 3.1 can be bounded by either

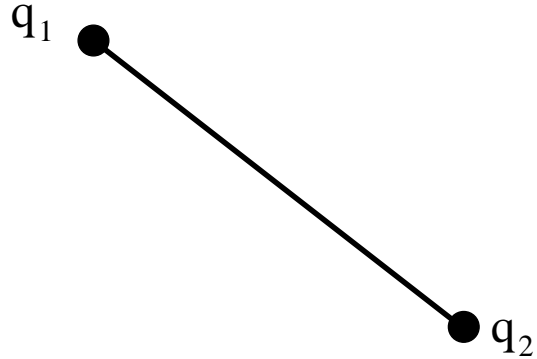


**Figure 6.1:** This figure shows two atoms bonded together and represents the configuration of atoms used in this chapter.

by constants or by the dominant part of the van der Waals term and do not affect our argument here.

Because the potential function  $U$  in Equation 6.2 is defined only in terms of the bond distance  $|\mathbf{q}_1 - \mathbf{q}_2|$ , the Boltzmann distribution is not integrable over the set of all  $(\mathbf{q}_1, \mathbf{q}_2)$  because translation does not change the energy  $U$ . Molecular dynamics simulations of peptide do not in general compute translational differences and are focused on intermolecular behavior and molecule-solvent interaction; moreover, translation is usually periodically subtracted out from simulations. For our problem, we remove translational differences by focusing only on the bond vector  $\mathbf{r} = \mathbf{q}_1 - \mathbf{q}_2$ , and re-write  $U$  in terms of  $\mathbf{r}$

$$U(\mathbf{r}) = K_{12}(|\mathbf{r}| - b_{12})^2 + \frac{A_{12}}{|\mathbf{r}|^{12}}. \quad (6.3)$$

A Langevin diffusion with invariant measure given by the corresponding Boltzmann distribution,

$$\pi(\mathbf{r}) = \frac{e^{-U(\mathbf{r})/k_B T}}{\int_{\mathbb{R}^2} e^{-U(\mathbf{r}')/k_B T} d\mathbf{r}'}, \quad (6.4)$$

is then given by

$$d\mathbf{r} = \Sigma d\mathbf{B}_t + \mu(\mathbf{r})dt, \quad (6.5)$$

where  $\mu(\mathbf{r}) = \frac{1}{2}\nabla \log \pi(\mathbf{r})$ ,  $\mathbf{B}_t$  is 2-dimensional Brownian motion, and  $\Sigma = \sigma I$  is chosen to be a constant multiple of the identity matrix. This gives us

$$d\mathbf{r} = \sigma d\mathbf{B}_t - \frac{1}{k_B T} \nabla U(\mathbf{r})dt. \quad (6.6)$$

We want to show that this stochastic differential equation is geometrically ergodic with respect to the Boltzmann distribution in Equation 6.4. In the next section we show that the SDE in Equation 6.6 satisfies Condition 10.

## 6.2 Control Function

To establish the Condition 10, we use a stochastic control. For any  $\epsilon'$  small, choose constant  $K(\epsilon')$  so that for all  $\mathbf{r}$  in the set  $C = \{\mathbf{r} : V(\mathbf{r}) \leq R(\epsilon')\}$ ,  $|\mathbf{r}| > \epsilon'$ . Such a  $K$  exists because the set  $C$  forms an annulus around the origin for small  $\epsilon'$ . With this set  $C$  we prove Condition 10 part one.

*Proof.* We define a control function, following the argument of Mattingly et al. [2002]. Consider the following control problem. Let  $R : \mathbb{R}^+ \rightarrow \mathcal{X}$  be a solution of the following SDE with control input  $S$ :

$$\frac{dR}{dt} = \mu(R) + \Sigma \frac{dS}{dt}. \quad (6.7)$$

For  $t \in [0, 1]$ ,  $\mathbf{r} \in C$ , and  $\mathbf{r}^+ \in C$ , we define a stochastic control  $S : \mathbb{R}^+ \rightarrow \mathcal{X}$  such that (6.7) is satisfied and  $R(0) = \mathbf{r}$ ,  $R(1) = \mathbf{r}^+$ . To find such an  $S$ , first write down

Equation 6.7 for potential  $U$  (6.2,

$$\frac{dR}{dt} + \frac{1}{K_B T} \nabla U(R) = \sigma \frac{dS}{dt}. \quad (6.8)$$

For any  $\mathbf{r}^+$ , we choose  $R$  to be the continuous path that concurrently rotates and rescales  $\mathbf{r}$  to  $\mathbf{r}^+$  such that  $\min\{|\mathbf{r}|, |\mathbf{r}|^+\} \leq |\mathbf{r}| \leq \max\{|\mathbf{r}|, |\mathbf{r}|^+\}$ . Note that this path stays entirely in  $C$  and thus avoids all points where  $|\mathbf{r}| \leq \epsilon$ . Within  $C$ , the potential function  $U$  is Lipschitz continuous. For  $0 \leq t \leq 1$ , we write down a trajectory  $\rho(t)$  of the SDE in Equation 6.5 and the trajectory  $R(t)$  of Equation 6.7:

$$\begin{aligned} \rho(t) &= \mathbf{r} + \int_0^t \mu(\rho(s)) ds + \Sigma B(t) \\ R(t) &= \mathbf{r} + \int_0^t \mu(R(s)) ds + \Sigma S(t). \end{aligned}$$

The event

$$\sup_{0 \leq t \leq 1} \|B(t) - S(t)\| \leq \epsilon$$

occurs with positive probability for any  $\epsilon > 0$ , since the Wiener measure of any such tube is positive in our compact set  $C$ . Assuming this event  $\|W(t) - S(t)\|$  occurs, note that

$$\begin{aligned} \|\rho(t) - R(t)\| &\leq \int_0^t \|\mu(\rho(s)) - \mu(R(s))\| ds + \|\Sigma\| \epsilon \\ &\leq \int_0^t M \|\rho(s) - R(s)\| ds + \|\Sigma\| \epsilon. \end{aligned} \quad (6.9)$$

since  $U$  and thus  $\mu$  are Lipschitz continuous over  $C$ . We then have that

$$\|\rho(t) - R(t)\| \leq K' \epsilon$$

for all  $t \in [0, 1]$  because for Equation 6.9 to hold for all  $t \in [0, 1]$ , the quantity  $\|\rho(t) - R(t)\|$  must go to zero as  $\epsilon$  goes to zero. So for any  $\delta$  we can choose  $\epsilon$  such that

$$P_t(\mathbf{r}, \mathcal{B}_\delta(\mathbf{r}^+)) > 0 \quad \forall \mathbf{r}.$$

Because we are on a compact set we can find  $\alpha > 0$  such that

$$\inf_{\mathbf{r} \in C} P_t(\mathbf{r}, \mathcal{B}_\delta(\mathbf{r}^+)) > \alpha.$$

□

### 6.3 Drift Condition

For stochastic differential equations, Has'minskii [1980] give an equivalent condition to Condition 11 in terms of the infinitesimal generator of the stochastic differential equation.

**Condition 12.** *There is a function  $V : \mathbb{R}^d \rightarrow [1, \infty)$ , with  $\lim_{\|\mathbf{r}\| \rightarrow \infty} V(\mathbf{r}) = \infty$ , and real numbers  $a \in (0, \infty)$ ,  $b \in (0, \infty)$  such that*

$$\mathcal{A}\{V(\mathbf{r})\} \leq -\alpha V(\mathbf{r}) + \beta, \tag{6.10}$$

where  $\mathcal{A}$  is the infinitesimal generator for Equation 6.5 given by

$$\mathcal{A}g = \sum_{i=1}^d \mu_i(\mathbf{r}) \frac{\partial g}{\partial \mathbf{r}_i} + \frac{1}{2} \sum_{i,j=1}^d [\Sigma \Sigma^T]_{ij} \frac{\partial^2 g}{\partial \mathbf{r}_i \partial \mathbf{r}_j}, \tag{6.11}$$

for  $g$  a twice integrable function.

Providing a function  $V$  that satisfies this assumption therefore establishes a drift condition for the SDE of Equation 6.6. First define

$$V(\mathbf{r}) = \frac{1}{|\mathbf{r}|} + \frac{1}{2}(|\mathbf{r}| - b_{12})^2 + 1 \quad (6.12)$$

and note that as  $|\mathbf{r}| \rightarrow \infty$ ,  $V(\mathbf{r}) \rightarrow \infty$ . To establish that Condition 12 holds, we consider the first term of  $\mathcal{A}\{V\}$ :

$$\begin{aligned} \mu(\mathbf{r}) \frac{\partial V}{\partial \mathbf{r}} &= -\frac{1}{k_B T} \left( \frac{2K_{12}(|\mathbf{r}| - b_{12})\mathbf{r}}{|\mathbf{r}|} - \frac{12A_{12}\mathbf{r}}{|\mathbf{r}|^{14}} \right) \left( \frac{(|\mathbf{r}| - b_{12})\mathbf{r}}{|\mathbf{r}|} - \frac{(\mathbf{r})}{|\mathbf{r}|^3} \right) \\ &= -\frac{1}{k_B T} \left( K_{12}(|\mathbf{r}| - b_{12})^2 - \frac{6A_{12}(|\mathbf{r}| - b_{12})}{|\mathbf{r}|^{13}} + \frac{6A_{12}}{|\mathbf{r}|^{15}} - \frac{K_{12}(|\mathbf{r}| - b_{12})}{|\mathbf{r}|^2} \right) \\ &= -\frac{1}{k_B T} \left( K_{12}(|\mathbf{r}| - b_{12})^2 + \frac{6A_{12}}{|\mathbf{r}|^{15}} + \frac{6A_{12}b_{12}}{|\mathbf{r}|^{13}} - \frac{6A_{12}}{|\mathbf{r}|^{12}} + \frac{b_{12}K_{12}}{|\mathbf{r}|^2} - \frac{K_{12}}{|\mathbf{r}|} \right). \end{aligned}$$

And since  $\Sigma = \sigma I$ , the second term of  $\mathcal{A}\{V\}$  is:

$$\frac{1}{2}\sigma^2 \frac{\partial^2 V}{\partial \mathbf{r}^2} = \frac{\sigma^2}{2} \left( 2 - \frac{2}{|\mathbf{r}|^3} + \frac{3}{|\mathbf{r}|^5} \right).$$

We then require that  $\mathcal{A}\{V\} \leq -\alpha V + \beta$ , or

$$\mathcal{A}\{V\} \leq -\alpha \left( \frac{1}{|\mathbf{r}|} + \frac{1}{2}(|\mathbf{r}| - b_{12})^2 \right) + \beta.$$

for some  $\alpha, \beta$ . Set  $\alpha = K_{12}/(k_B T)$  and the inequality simplifies to

$$\begin{aligned} &-\frac{1}{k_B T} \left( \frac{6A_{12}}{|\mathbf{r}|^{15}} + \frac{6A_{12}b_{12}}{|\mathbf{r}|^{13}} - \frac{6A_{12}}{|\mathbf{r}|^{12}} + \frac{b_{12}K_{12}}{|\mathbf{r}|^2} - \frac{K_{12}}{|\mathbf{r}|} \right) + \sigma^2 \left( 2 - \frac{2}{|\mathbf{r}|^3} + \frac{3}{|\mathbf{r}|^5} \right) \\ &\leq -\frac{K_{12}}{k_B T} \left( \frac{1}{|\mathbf{r}|} \right) + \beta. \end{aligned}$$

Choosing  $\beta = 5\sigma^2 + (6A_{12} + K_{12})/(k_B T)$  satisfies Condition 12 for all  $\mathbf{r}$ ; thus we have established the required drift condition.

The uniform reachability condition obtained in Section 6.2 and the drift condition obtained above are sufficient to establish geometric ergodicity of the simplified system given by Equation 6.6. However for practical problems we are interested in systems with  $n >> 2$ . The drift condition may be expanded to a system of  $n$  atoms connected in a chain with both the bond term and the van der Waals term acting on consecutive atoms in the chain. However, the proof of Condition 10 relies on the geometry of annulus shape created by level curves of the Lyapunov function  $V$ . For larger  $n$ , an argument using a sequential control function translating one bond at a time may work.

Note that this result is for the theoretical continuous time system given by the SDE 6.6. As pointed out in Chapter 5, it is important to verify that the results hold for the discrete-time dynamical system obtained via a choice of numerical integrator. We have not done this here, and it is an important subject for future work.

# Chapter 7

## Conclusion

The research for this thesis started out as protein structure prediction and evolved into peptide folding, comparing simulation to experiment, and verifying the accuracy of the methods used for simulation. This verification is important for biomolecular simulation so that as energy functions evolve and more effort is made to simulate biomolecules, the mathematics behind the simulation are sound.

When statistical methods such as parallel tempering are adapted for use in molecular simulation, or when novel isothermal numerical integrators are introduced, the validity of the methods must be checked for proper behavior. We have made an effort to examine a wide range of numerical integrators that are being used or have been developed for biomolecular simulation and have shown that many of these methods either need modification, or should not be used at all.

We have also made a concerted effort to address the overused assumption of ergodicity by biomolecular simulations. Numerical integrators either are ergodic or are not ergodic and cannot be adjusted to improve ergodicity. Although ergodicity can be hard to prove, we have shown that for some integrators, it is easy to disprove,

and thus should not be automatically assumed.

Our simulation of peptides in Chapters 3 and 4 were done using an integrator popular at the time, but Chapter 5 shows that the Berendsen heat bath does not preserve the Boltzmann distribution. It is therefore of interest to rerun our simulations with the stochastic integrators of Chapter 5 and 6 to determine the extent of the error introduced by the Berendsen heat bath, but we have not yet done so.

## 7.1 Future Work

A natural extension of the work in Chapter 6 is to establish the geometric ergodicity of Langevin dynamics and the accuracy of the stochastic numerical methods being used, such as the BBK integrator [Brünger et al., 1984]. As the simulation community has become more aware of the errors introduced by methods such as Berendsen, there has been a shift towards Langevin dynamics. However, although deterministic methods have been constructed to be symplectic to preserve the Lebesgue measure, the construction of SDE numerical integrators has not been as well studied.

Our results in Chapter 5 showing the shortcomings of other popular methods such as Nosé-Hoover chains and current versions of Nosé-Poincaré suggest that simulators should instead consider stochastic methods such as the BBK integrator or other Langevin integrators. It is desirable to formally establish the convergence properties of these methods so that this can be done with confidence, or to clarify whether better methods should be developed for stochastic use.

# Bibliography

- B. J. Alder and T. E. Wainwright. Phase transition for a hard-spere system. *Journal of Chemical Physics*, 27(5):1208, 1957.
- V. I. Arnold. *Mathematical Methods of Classical Mechanics*. Springer-Verlag, 2nd edition, 1989.
- D A Beck, G W White, and V Daggett. Exploring the energy landscape of protein folding using replica-exchange and conventional molecular dynamics simulations. *Journal of Structural Biology*, 157(3):514–523, 2007.
- H. J. C. Berendsen, J. P. M. Postma, W. F. van Gunsterenand A. DiNola, and J. R. Haak. Molecular dynamics with coupling to an external bath. *Journal of Chemical Physics*, 81:3684–90, 1984.
- Nayantara Bhatnagar and Dana Randall. Torpid mixing of simulated tempering on the Potts model. In *Proceedings of the 15th ACM/SIAM Symposium on Discrete Algorithms (SODA)*, pages 478–487, 2004.
- P. Billingsley. *Probability and Measure*. Wiley, 3<sup>rd</sup> edition, 1995.
- Stephen D Bond, Benedict J Leimkuhler, and Brian B Laird. The Nosé-Poincaré method for constant temperature molecular dynamics. *Journal of Computational Physics*, 151:114–134, 1999.
- Carl Branden and John Tooze. *Introduction to Protein Structure*. Garland, 2<sup>nd</sup> edition, 1999.
- Michael Braxenthaler, Ron Unger, Auerbach Ditz, James A. Given, and John Moult. Chaos in protein dynamics. *Proteins: Structure, Function, and Genetics*, 29:417–425, 1997.
- B. R. Brooks, R. E. Bruccoleri, B. D. Olafson, D. J. States, S. Swaminathan, and M. Karplus. CHARMM: A program for macromolecular energy, minimization, and dynamics calculations. *Journal of Computational Chemistry*, 4(2):187–218, 1983.
- Charles L. Brooks and David A. Case. Simulations of peptide conformational dynamics and thermodynamics. *Chemical Reviews*, 93:2487–2502, 1993.
- Stephen P. Brooks and Andrew Gelman. General methods for monitoring convergence of iterative simulations. *Journal of Computational and Graphical Statistics*, 7(4):434–455, 1998.

- A. Brünger, C.L. Brooks III, and M. Karplus. Stochastic boundary conditions for molecular dynamics simulations of st2 water. *Chemical Physics Letters*, 105(5):495–500, 1984.
- P. J. Channell and C. Scovel. Symplectic integration of Hamiltonian systems. *Nonlinearity*, 3:231–259, 1990.
- Geon Ho Choe. *Computational Ergodic Theory*. Springer-Verlag, 2005.
- Ben Cooke and Scott C. Schmidler. Statistical prediction and molecular dynamics simulation. *Biophysical Journal*, 95(10):4497–4511, 2008a.
- Ben Cooke and Scott C. Schmidler. Preserving the boltzmann ensemble in replica-exchange molecular dynamics. *Journal of Chemical Physics*, 129(16):1–17, 2008b.
- Mary Kathryn Cowles and Bradley P. Carlin. Markov chain Monte Carlo convergence diagnostics: A comparative review. *Journal of the American Statistical Association*, 91(434):883–904, 1996.
- Valerie Daggett, Peter A. Kollman, and Irwin D. Kuntz. A molecular dynamics simulation of polyalanine: An analysis of equilibrium motions and helix-coil transitions. *Biopolymers*, 31:1115–1134, 1991.
- Xavier Daura, Bernhard Juan, Dieter Seebach, Wilfred F. van Gunsteren, and Alan E. Mark. Reversible peptide folding in solution by molecular dynamics simulation. *Journal of Molecular Biology*, 280:925–932, 1998.
- Xavier Daura, Karl Gademann, Bernhard Jaun, Dieter Seebach, Wilfred F. van Gunsteren, and Alan E. Mark. Peptide folding: When simulation meets experiment. *Agnew. Chem. Int. Ed.*, 38(1/2):236–240, 1999.
- Y. Duan and Peter A. Kollman. Pathways to a protein folding intermediate observed in a 1-microsecond simulation in aqueous solution. *Science*, 282:740–744, October 1998.
- S. Duane, A.D. Kennedy, B.J. Pendleton, and D. Roweth. Hybrid Monte Carlo. *PhysLettB*, 195:216–222, 1987.
- Y. Fan, Stephen P. Brooks, and Andrew Gelman. Output assessment for Monte Carlo simulations via the score statistic. *Journal of Computational and Graphical Statistics*, 15(1):178–206, 2006.
- B. Forood, E. J. Feliciano, and K. P. Nambiar. Stabilization of  $\alpha$ -helical structures in short peptides via end capping. *Proc. Natl. Acad. Sci.*, 90:838–842, 1993.

- Daan Frenkel and Berend Smit. *Understanding Molecular Simulation*. Academic Press, 1996.
- Angel E. Garcia and Kevin Y Sanbonmatsu.  $\alpha$ -helical stabilization by side chain shielding of backbone hydrogen bonds. *Proceedings of the National Academy of Sciences USA*, 99(5):2782–2787, 2002.
- Andrew Gelman and Donald B. Rubin. Inference from iterative simulation using multiple sequences. *Statistical Science*, 7:457–511, 1992.
- Andrew Gelman, John B. Carlin, Hal S. Stern, and Donald B. Rubin. *Bayesian Data Analysis*. Chapman & Hall, 2<sup>nd</sup> edition, 2004.
- Charles J. Geyer. Practical Markov chain Monte Carlo. *Statistical Science*, 7:473–511, 1992.
- Charlie J. Geyer. Markov chain Monte Carlo maximum likelihood. In *Computing Science and Statistics: Proc. 23<sup>rd</sup> Symp. Interface*, pages 156–163, 1991.
- S. Gnanakaran, Hugh Nymeyer, John Portman, Kevin Y. Sanbonmatsu, and Angel E. Garcia. Peptide folding simulations. *Current Opinion in Structural Biology*, 13:168–174, 2003.
- E. M. Goodman and P. S. Kim. Folding of a peptide corresponding to the alpha-helix in bovine pancreatic trypsin inhibitor. *Biochemistry*, 28:4343–7, 1989.
- Ulrich H. E. Hansmann and Yuko Okamoto. Finite-size scaling of helix-coil transitions in poly-alanine studied by multicanonical simulations. *Journal of Chemical Physics*, 110(2):1267–1276, 1999.
- R. Z. Has'minskii. *Stochastic Stability of Differential Equations*. Sijthoff and Noordhoff, 1980.
- Trevor Hastie, Robert Tibshirani, and Jerome Friedman. *The Elements of Statistical Learning*. Springer, 2001.
- W.K. Hastings. Monte Carlo sampling methods using Markov chains and their applications. *Biometrika*, 57:97–109, 1970.
- R.W. Hockney. The potential calculation and some applications. *Methods in Computational Physics*, 9:136–211, 1970.
- William G Hoover. Canonical dynamics: Equilibrium phase-space distributions. *Physical Review A*, 31(3):1695–1697, 1985.

- Gouri S. Jas and Krzysztof Kuczera. Equilibrium structure and folding of a helix-forming peptide: Circular dichroism measurements and replica-exchange molecular dynamics simulations. *Biophysical Journal*, 87:3786–3798, 2004.
- Brian B. Laird and Benedict J. Leimkuhler. Generalized dynamical thermostating technique. *Phys. Rev. E*, 68(1):016704, Jul 2003.
- Andrew R. Leach. *Molecular Modelling: Principles and Applications*. Addison Wesley Longman Ltd., 1996.
- Benedict J. Leimkuhler and Christopher R. Sweet. The canonical ensemble via symplectic integrators using Nosé and Nosé-Poincaré chains. *Journal of Chemical Physics*, 121(1):108–116, 2004.
- Erik Lindahl, Berk Hess, and David van der Spoel. GROMACS 3.0: a package for molecular simulation and trajectory analysis. *Journal of Molecular Modeling*, 7: 306–317, 2001.
- Jun S. Liu. *Monte Carlo Strategies in Scientific Computing*. Springer-Verlag, 2001.
- Neal Madras and Zhongrong Zheng. On the swapping algorithm. *Random Structures & Algorithms*, 1:66–97, 2003.
- Glenn J Martyna, Michael L Klein, and Mark Tuckerman. Nosé-Hoover chains: The canonical ensemble via continuous dynamics. *Journal of Chemical Physics*, 97(4): 2635–2643, 1992.
- Jonathan Mattingly and Scott McKinley. Ergodicity of a bead-spring pair with stochastic Stokes forcing. In preparation, 2008.
- Jonathan Mattingly, Andrew M. Stuart, and D. J. Higham. Ergodicity for SDEs and approximations: Locally Lipschitz vector fields and degenerate noise. *Stochastic Processes and their Applications*, 101:185–232, 2002.
- N. Metropolis, A. W. Rosenbluth, M. N. Rosenbluth, A. H. Teller, and E. Teller. Equation of state calculations by fast computing machines. *Journal of Chemical Physics*, 21:1087–1092, 1953.
- S.P. Meyn and R.L. Tweedie. *Markov Chains and Stochastic Stability*. Springer-Verlag, 1993.
- T. Morishita. Fluctuation formulas in molecular-dynamics simulations with the weak coupling heat bath. *Journal of Chemical Physics*, 113(8):2976–2982, 2000.
- Victor Munoz and Luis Serrano. Development of the multiple sequence approximation within the AGADIR model of  $\alpha$ -helix formation: Comparison with Zimm-Bragg and Lifson-Roig formalisms. *Biopolymers*, 41(5):495–509, 1997.

- R.M. Neal. Probabilistic inference using Markov chain Monte Carlo methods. Technical Report CRG-TR-93-1, University of Toronto, 1993.
- P H Nguyen, Y Mu, and G Stock. Structure and energy landscape of a photoswitchable peptide: a replica exchange molecular dynamics study. *Proteins: Structure, Function, and Genetics*, 60(3):485–494, 2005.
- Shuichi Nosé. A unified formulation of the constant temperature molecular dynamics methods. *Journal of Chemical Physics*, 81(1):511–519, 1984.
- Shuichi Nosé. An improved symplectic integrator for Nosé-Poincaré thermostat. *Journal of the Physical Society of Japan*, 70(1):75–77, 2001.
- Hugh Nymeyer and Angel E Garcia. Simulation of the folding equilibrium of  $\alpha$ -helical peptides: A comparison of the generalized Born approximation with explicit solvent. *Proceedings of the National Academy of Sciences USA*, 100:13934–13939, 2003.
- R. W. Pastor. Techniques and applications of Langevin dynamics simulations. In G. R. Luckhurst and C. A. Veracini, editors, *The Molecular Dynamics of Liquid Crystals*, pages 85–138. Kluwer Academic, 1994.
- D A Pearlman, D A Case, J W Caldwell, W R Ross, T E Cheatham III, S DeBolt, D Ferguson, G Seibel, and P Kollman. AMBER, a computer program for applying molecular mechanics, normal mode analysis, molecular dynamics and free energy calculations to elucidate the structures and energies of molecules. *Comp. Phys. Commun.*, 91:1–41, 1995.
- Yong Peng and Ulrich H. E. Hansmann. Solvation model dependency of helix-coil transition in polyalanine. *Biophysical Journal*, 82:3269–3276, 2002.
- X Periole and A E Mark. Convergence and sampling efficiency in replica exchange simulations of peptide folding in explicit solvent. *Journal of Chemical Physics*, 126(1):014903, 2007.
- James C. Phillips, Rosemary Braun, Wei Wang, James Gumbart, Emad Tajkhorshid, Elizabeth Villa, Christophe Chipot, Robert D. Skeel, Laxmikant Kale, and Klaus Schulten. Scalable molecular dynamics with namd. *Journal of Computational Chemistry*, 26:1781–1802, 2005.
- G.O. Roberts and J.S. Rosenthal. Examples of Adaptive MCMC. *J. Comp. Graph. Stat. (to be published)*, 2006.
- G.O. Roberts and R.L. Tweedie. Exponential convergence of Langevin distributions and their discrete approximations. *Bernoulli*, 2(4):341–363, 1996.

- A E Roitberg, A Okur, and C Simmerling. Coupling of replica exchange simulations to a non-Boltzmann structure reservoir. *JPhysChem B*, 111(10):2415–2418, 2007.
- J. P. Ryckaert, G. Ciccotti, and H. J. C. Berendsen. Numerical integration of the Cartesian equations of motion of a system with constraints: Molecular dynamics of n-alkanes. *J. Comp. Phys.*, 23:327–341, 1977.
- Tamar Schlick. *Molecular Modeling and Simulation*. Springer-Verlag, 2002.
- Scott C. Schmidler, Joe Lucas, and Terrence G. Oas. Statistical estimation in statistical mechanical models: Helix-coil theory and peptide helicity prediction. *Journal of Computational Biology*, 14(10):1287–1310, 2007.
- J. Martin Scholtz and Robert L. Baldwin. The mechanism of  $\alpha$ -helix formation by peptides. *Annual Review of Biophysics and Biomolecular Structure*, 21:95–118, 1992.
- M M Seibert, A Patriksson, B Hess, and D van der Spoel. Reproducible polypeptide folding and structure prediction using molecular dynamics simulations. *Journal of Molecular Biology*, 354(1):173–183, 2005.
- William Shalongo and Earle Stellwagen. Dichroic statistical model for prediction and analysis of peptide helicity. *Proteins: Structure, Function, and Genetics*, 28: 467–480, 1997.
- Lorna J. Smith, Xavier Daura, and Wilfred F. van Gunsteren. Assessing equilibration and convergence in biomolecular simulations. *Proteins: Structure, Function, and Genetics*, 48(3):487–496, 2002.
- C. D. Snow, N. Nguyen, Vijay S. Pande, and M. Gruebele. Absolute comparison of simulated and experimental protein-folding dynamics. *Nature*, 42:102–106, 2002.
- Eric J. Sorin and Vijay S. Pande. Exploring the helix-coil transition via all-atom equilibrium ensemble simulations. *Biophysical Journal*, 88:2472–2493, 2005a.
- Eric J. Sorin and Vijay S. Pande. Empirical force-field assessment: The interplay between backbone torsions and noncovalent term scaling. *J. Comp. Chem.*, 26: 682–690, 2005b.
- Shari Spector, Michael Rosconi, and Daniel P. Raleigh. Conformational analysis of peptide fragments derived from the peripheral subunit-binding domain from the pyruvate dehydrogenase multienzyme complex of *Bacillus stearothermophilus*: Evidence for nonrandom structure in the unfolded state. *Biopolymers*, 49:29–40, 1999.

- W. Clark Still, Anna Tempczyk, Ronald Hawley, and Thomas Hendrickson. Semi-analytic treatment of solvation for molecular mechanics and dynamics. *J. Am. Chem. Soc.*, 112:6127–6129, 1990.
- K. G. Strehlow and R. L. Baldwin. Effect of the substitution Ala-Gly at each of five residue positions in the C-peptide helix. *Biochemistry*, 28:2130–3, 1989.
- Yuji Sugita and Yuko Okamoto. Replica-exchange molecular dynamics method for protein folding. *Chemical Physics Letters*, 314:141–151, 1999.
- William C. Swope, Hans C. Andersen, Peter H. Berens, and Kent R. Wilson. A computer simulation method for the calculation of equilibrium constants for the formation of physical clusters of molecules: Application to small water clusters. *Journal of Chemical Physics*, 76(1):637–649, 1982.
- Luke Tierney. Markov chains for exploring posterior distributions. *Annals of Statistics*, 22(4):1701–1728, 1994.
- S Toxvaerd. Molecular dynamics at constant temperature and pressure. *Physical Review E*, 47(1):343–350, 1993.
- V. Tsui and D. A. Case. Theory and applications of the generalized Born solvation model in macromolecular simulations. *Biopolymers*, 56:275–291, 2001.
- Wilfred F. van Gunsteren and Alan E. Mark. Validation of molecular dynamics simulation. *Journal of Chemical Physics*, 108(15):6109–6116, 1998.
- Loup Verlet. Computer "experiments" on classical fluids. i. thermodynamical properties of lennard-jones molecules. *Physical Review*, 159(1):98, Jul 1967.
- Roland G Winkler, Volker Kraus, and Peter Reineker. Time reversible and phase-space conserving molecular dynamics at constant temperature. *Journal of Chemical Physics*, 102(22):9018–9025, 1995.
- Dawn Woodard, Scott Schmidler, and Mark Huber. Sufficient conditions for torpid mixing of parallel and simulated tempering on multimodal distributions. (submitted to *Electron. J. Probab.*), 2007.
- Dawn Woodard, Scott Schmidler, and Mark Huber. Conditions for rapid mixing of parallel and simulated tempering on multimodal distributions. *Annals of Applied Probability* (to be published), 2008.
- W Zhang, C Wu, and Y Duan. Convergence of replica exchange molecular dynamics. *Journal of Chemical Physics*, 123(15):154105, 2005.

# Biography



Benjamin Perry Cooke Isard was born in Washington, DC on August 12, 1978 to parents Margaret Anne Cooke and Peter Isard. As a child he attended All Saints All Day nursery school, Lafayette Elementary and the Sidwell Friends School from 7th through 12th grades. He spent his undergraduate years at the Massachusetts Institute of Technology, where he was an All-American in doubles as a member of the MIT varsity tennis team and his paper, “Reed-Muller Error Correcting Codes,” was published in the MIT undergraduate journal of mathematics. Ben was also an active member of the Chi Phi fraternity while at MIT, serving as president during his senior year in the house. After graduating from MIT with a Bachelors of Science in Mathematics Applied to Computer Science with a minor in Economics, Ben matriculated to the Duke University Mathematics Department, where he has enjoyed the sunny North Carolina weather. On a beautiful day in October 2006, Ben married his college sweetheart Linda Yu in Knoxville, Tennessee. In 2008, Ben has had two papers accepted to be published with his advisor, Scott Schmidler: “Statistical Prediction and Molecular Dynamics Simulation” in the Biophysics Journal and “Preserving the Boltzmann ensemble in replica-exchange molecular dynamics” in the Journal of Chemical Physics.